CHALMERS
UNIVERSITY OF TECHNOLOGY

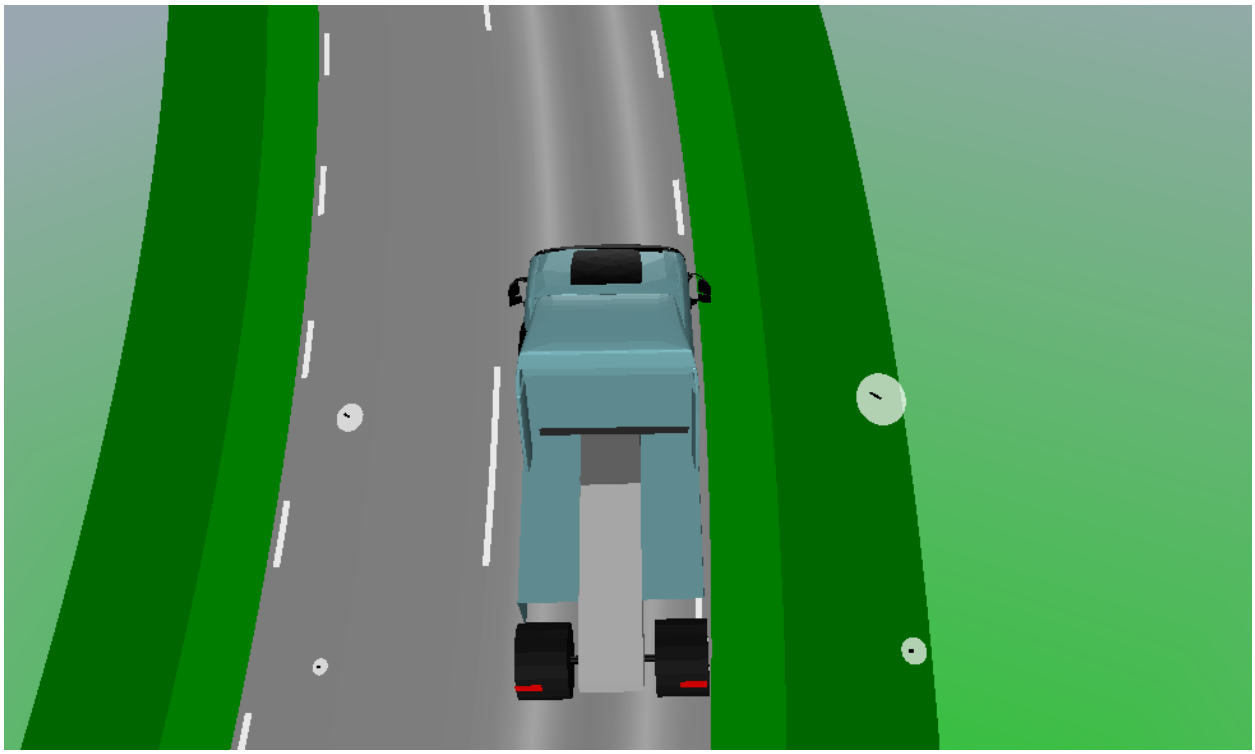

On torque vectoring to improve steering predictability while minimising power loss in heavy electric vehicles using model predictive control

Master's thesis in Systems, Control and Mechatronics

Jonas Persson
Jonathan Åkesson

DEPARTMENT OF MECHANICS AND MARITIME SCIENCES

CHALMERS UNIVERSITY OF TECHNOLOGY
Gothenburg, Sweden 2023
www.chalmers.se

Master's thesis 2023

On torque vectoring to improve steering predictability while minimising power loss in heavy electric vehicles using model predictive control

Jonas Persson
Jonathan Åkesson

CHALMERS
UNIVERSITY OF TECHNOLOGY

Department of Mechanics and Maritime Sciences
Division of Vehicle Engineering and Autonomous Systems
Vehicle Dynamics Group
Chalmers University of Technology
Gothenburg, Sweden 2023

On torque vectoring to improve steering predictability while minimising power loss in heavy electric vehicles using model predictive control
Master's Thesis
JONAS PERSSON
JONATHAN ÅKESSON

Supervisor: Sachin Janardhanan, Volvo Group Trucks Technology, Gothenburg, Sweden
Examiner: Bengt Jacobson, Mechanics and Maritime Sciences, Chalmers University of Technology, Gothenburg, Sweden

Master's Thesis 2023
Department of Mechanics and Maritime Sciences
Division of Vehicle Engineering and Autonomous Systems
Vehicle Dynamics Group
Chalmers University of Technology
SE-412 96 Gothenburg
Telephone +46 31 772 1000

Typeset in LaTeX
Printed by Chalmers Reproservice
Gothenburg, Sweden 2023

On torque vectoring to improve steering predictability while minimising power loss in heavy electric vehicles using model predictive control
Master's Thesis
JONAS PERSSON
JONATHAN ÅKESSON
Department of Mechanics and Maritime Sciences
Chalmers University of Technology

Abstract

The vehicle industry is moving towards electrical propulsion, and thereby improving the capabilities of the powertrain designs. Examples are the ability to produce both positive and negative torque, and the ability to have individually controlled wheels. These abilities also add redundancy to the powertrain system while allowing its primary objective of achieving the desired vehicle motion to be met. It may then fulfil secondary objectives, such as minimising power losses or tyre wear. With multiple motors, it is possible to micromanage the dynamics of the vehicle by varying the torque distribution on different wheels. This is called torque vectoring and includes the act of varying torque both in the longitudinal and lateral direction. This thesis analyses the impact of torque vectoring on a 4x4 heavy electric vehicle.

The torque vectoring controller acts as a global force request generator, taking in a yaw rate reference together with either an acceleration request in form of pedal positions from the driver or a velocity request in an autonomous driving algorithm. The outputs of the controller are the requested global forces, which are then distributed to the actuators using control allocation, while optimising for power loss minimisation. A Model Predictive Controller (MPC), with a prediction horizon of 1 second, was chosen as the motion coordinator, as it is able to account for actuator and friction limitations and ensure that the requested forces to the control allocation are feasible. The target for the lateral control, in the MPC, was chosen as the vehicle's steady state yaw rate response, as it reduces the amount of compensation from the driver during acceleration or braking.

Results show that the lateral control from the MPC is able to reduce the braking distance in a curve, as well as reduce the steering wheel angle compensation from the driver when hard braking with 20-30 degrees. In addition, it is able to minimise the change in vehicle behaviour caused by changing distribution of propulsion between front and rear motors. In a simulation on road data from Hällered to Alingsås (distance of 2.8 km), the controller uses approximately 1.3% more power than a vehicle with no lateral control. An alternate controller style was developed to only interfere when the vehicle diverged from the expected behaviour. This controller managed to decrease the excess power consumption to 0.1% more than no lateral control.

Keywords: Torque Vectoring, MPC, Power Loss, Steering Feel, Predictable, Heavy Vehicles

Acknowledgements

This master thesis was carried out at Volvo Group Trucks Technology in Gothenburg during the spring of 2023.

A big thank you to our supervisors and examiner at Volvo GTT and Chalmers for expressing a genuine interest in our work and encouragement along the way. Sachin Janardhanan for diving deep into our concepts and control design, ensuring our thesis turned out the best it could. Our examiner Bengt Jacobson for providing support far beyond what is expected from an examiner, joining almost every weekly meeting to give advice. Thank you to Leo Laine for very interesting discussions and exciting ideas, giving a direction when we were unsure how to progress. Thanks to Simon Schoutissen for supporting us in the team and ensuring we had a clear goal when working. A big thank you to the people at Volvo that took the time out of their workday to discuss our thesis and provide feedback to our ideas.

A final thank you to our families for your continuous support throughout these many years of studies, for your comfort and encouragement when times were tough.

Jonas Persson & Jonathan Åkesson, Gothenburg, June, 2023

List of Acronyms

Below is the list of acronyms that have been used throughout this thesis listed in alphabetical order:

CA	Control Allocator
CoG	Centre of Gravity
ICE	Internal Combustion Engine
IM	Induction Machine
LPV	Linear Parameter Varying
LQR	Linear Quadratic Regulator
PID	Proportional Integral Derivative
MIMO	Multiple Input Multiple Output
MPC	Model Predictive Controller
PMSM	Permanent Magnet Synchronous Machine
SISO	Single Input Single Output
VTM	Volvo Transport Model

Nomenclature

Below is the nomenclature of indices, parameters, and variables that have been used throughout this thesis.

Indices

crs	Indication for cruisability axle
fl	Subscript indication for front left
fr	Subscript indication for front right
i	Index for wheel
j	Index for wheel axle
rl	Subscript indication for rear left
rr	Subscript indication for rear right
stb	Indication for startability axle
t	Index for time step
x	Vehicle longitudinal direction
y	Vehicle lateral direction
z	Vehicle vertical direction

Parameters

ρ	Air density (kg/m^3)
c_d	Air resistance coefficient
$C_{f\alpha}$	Cornering stiffness, front (N/rad)
$C_{r\alpha}$	Cornering stiffness, rear (N/rad)
A_f	Frontal area (m^2)
gr_{crs}	Gear ratio, Cruisability axle (Nm/Nm)
gr_{stb}	Gear ratio, Startability axle (Nm/Nm)

g	Gravity (m/s^2)
T_s	Simulation loop time (s)
$T_{s,MPC}$	MPC horizon step time (s)
m	Mass (kg)
c_r	Rolling resistance coefficient (N/N)
r_s	Scrub radius (m)
t_f	Track width, front (m)
t_r	Track width, rear (m)
L	Wheel base (m)
L_f	Wheel base, front (m)
L_r	Wheel base, rear (m)
r_w	Wheel radius (m)
K_u	Understeer coefficient ($rad/(m/s^2)$)
I_{zz}	Yaw Inertia (kg/m^2)

Variables

ω	Angular velocity of vehicle (rad/s)
β	Body slip angle (rad)
F	Force (N)
δ_f	Steering angle (rad)
$\omega_{fl,fr,rl,rr}$	Tyre rotational speed (rad/s)
v	Translational velocity of vehicle (m/s)
a	Vehicle acceleration (m/s^2)
θ_z	Yaw angle (rad)

Contents

List of Acronyms **ix**

Nomenclature **xi**

1 Introduction **1**
1.1 Torque Vectoring . . . 1
1.2 Modular Powertrain Configuration for Heavy Vehicles . . . 2
1.3 Motivation . . . 3
1.4 Purpose . . . 4
1.5 Scope and limitations . . . 4

2 Vehicle Modelling **5**
2.1 Tyre Dynamics . . . 5
2.1.1 Longitudinal Tyre Slip . . . 6
2.1.2 Lateral Tyre Slip . . . 6
2.1.3 Combined Slip . . . 7
2.1.4 Safe Operating Limits . . . 8
2.1.5 Linear Tyre Model . . . 9
2.2 Longitudinal Dynamics . . . 9
2.3 Lateral Dynamics . . . 11
2.3.1 Body Slip Angle . . . 11
2.3.2 Yaw Rate . . . 13
2.3.3 Rollover . . . 13
2.4 Torque Vectoring . . . 14
2.5 Force Estimation . . . 16
2.5.1 Lateral Force Estimation . . . 16
2.5.2 Vertical Force Estimation . . . 16
2.6 Electrical Motors . . . 18
2.6.1 Motor Efficiency and Output limits . . . 19
2.6.2 Power Loss . . . 21

3 Steering Feel **23**
3.1 Previous works . . . 23
3.1.1 Torque Gradient . . . 24
3.1.2 Steering Gradient . . . 24
3.1.3 Jerk . . . 25
3.2 Interviews . . . 26

3.3 Predictability in Emergency Manoeuvres . . . 26
3.4 Sudden Switch between Cruise and Power mode . . . 29
3.4.1 Steady-state cornering . . . 29
3.4.2 Acceleration during cornering . . . 30

4 Control System **33**
4.1 Driver Model and Vehicle Model . . . 33
4.2 Driver Interpreter and Predictor . . . 34
4.3 Control Allocator and Limit Calculator . . . 34
4.3.1 Accounting for Static Losses in the Electrical Motors . . . 36
4.4 Motion Coordinator . . . 37
4.4.1 PID . . . 37
4.4.2 LQR/LQI . . . 37
4.4.3 LQR - LPV . . . 38
4.4.4 MPC . . . 39
4.4.4.1 MPC Model . . . 39
4.4.4.2 QP Formulation . . . 41
4.4.5 Static Reference Tracking . . . 44
4.4.6 Agile Reference Tracking . . . 45
4.4.7 Relaxing the Controller Output . . . 47
4.4.8 Barrier Method . . . 48

5 Test Setups for Verification and Validation **51**
5.1 Controller Comparison . . . 51
5.2 Feasibility at Tyre Limit . . . 53
5.3 Noise Impact on Controller . . . 53
5.4 MPC Sample Time Comparison . . . 54
5.5 Validation and Performance of Relaxed Request . . . 54
5.6 Soft Barrier Test . . . 55
5.7 Emergency Braking while cornering . . . 56
5.8 Mode Switching . . . 57
5.9 Rollover Prevention . . . 57
5.10 Comparison of Power Loss Optimisation and Power Usage in Forced and Relaxed Request . . . 57
5.11 Short Haul Power Use Simulation . . . 58

6 Results **61**
6.1 Controller comparison . . . 61
6.2 Feasibility at Tyre Limit . . . 63
6.3 Noise Impact on Controller . . . 66
6.4 MPC Sample Time Comparison . . . 66
6.5 Validation and Performance of Relaxed Requests . . . 68
6.6 Soft Barrier Test . . . 70
6.7 Emergency Braking while cornering . . . 73
6.8 Reducing mode switch impact . . . 75
6.9 Rollover Prevention Constraint . . . 76
6.10 Acceleration in Curve . . . 78

6.11 Short Haul Power Use Simulation 79

7 Conclusion **83**

Bibliography **85**

A Inequality matrices **I**

B 6x4 Tractor **VII**

1
Introduction

The automotive industry plays an important role in reaching the global goal of reducing carbon dioxide emissions. Within the European Union, a proposal has been made that all cars and vans being sold after year 2035 needs to be free from carbon emissions [1]. Similar goals are set on heavy vehicles [2], with more aggressive goals being suggested by the European Union to reduce truck emissions by 90% by 2040 [3]. As a result, the automotive industry is switching from combustion engines to electrical powertrains as a standard mode of propulsion. When comparing power train layouts between internal combustion engines (ICE) and electrical motors, it is found that the electrical propulsion allows for a much more flexible powertrain layout. This is a key component also contributing to improved vehicle designs and performance.

1.1 Torque Vectoring

Torque vectoring involves distributing torque on different axles or wheels of a vehicle to influence characteristics of the vehicle or optimise secondary objectives. The concept of torque vectoring is not new, and not necessarily related to electric propulsion. A rear wheel active yaw control system was introduced with the Mitsubishi Lancer Evolution IV in 1996 [4]. With an electric powertrain configuration, however, it is possible to more accurately control the power output. Electrical vehicles that incorporate a torque vectoring system are commonly available in the market, with examples such as the Rivian R1T in 2021 [5] and even more recently the Polestar 3, which is planned to be released in 2023 [6].

Torque vectoring shows promising improvements in electrical vehicles as it can enhance the vehicle's lateral performance, reduce power consumption by more efficient torque distribution and improve grip by reducing torque on the inner wheels in a curve. These are great advances within the field, but the research on torque vectoring is predominantly related to passenger cars and not heavy vehicles. As a result, the focus on development is on driving performance or tyre wear.

The load and centre of gravity on heavy vehicles tend to vary significantly more than passenger cars due to load conditions. This change in dynamics together with the general behaviour difference between cars and heavy vehicles produces an interest in analysing how torque vectoring affects heavy vehicles. As heavy vehicles such as trucks spend a lot of time on the roads, a more consistent driving experience

could result in fewer driver mistakes and a safer journey. This poses an interesting challenge on the controller design requirements for heavy vehicles.

1.2 Modular Powertrain Configuration for Heavy Vehicles

At Volvo, a modular powertrain structure for heavy vehicles has been proposed, using two separate e-axles with individual motors controlling each wheel [7]. An e-axle is defined as the electric machines being positioned with a common rotational axis similar to a vehicle axle, although not necessarily physically connected to eachother. This configuration, which is illustrated in Figure 1.1, uses a cruise axle in the front and a startability axle in the rear. The cruise axle is designed to be used in highway operations, without the startability axle being active. The electrical machines on the startability axle can be demagnetised during this type of driving to save in on idle losses. This continues until either a high acceleration is requested by the driver, or if there is a steep road incline (>2%), in which case the startability axle will contribute with additional power.

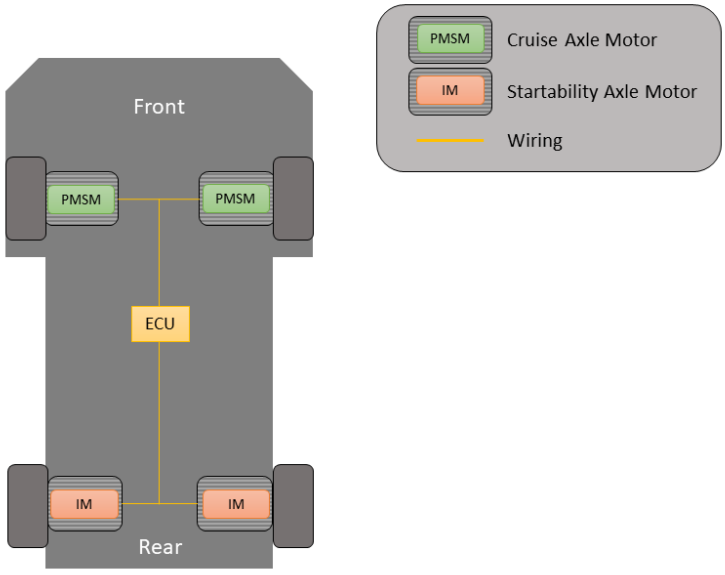

Figure 1.1: An illustration of the modular e-axle 4x4 truck proposed by S. Janardhanan in [7].

Upon engaging the rear axle for added power, the steering characteristics of the vehicle changes due to the difference in torque distribution between the front and rear axle. The handling properties shifts from that of a front-wheel-driven vehicle to that of an all-wheel-driven vehicle. This influences handling variables such as the

understeering gradient, risking an unpredictable steering behaviour. A suggested solution to this problem is to use torque vectoring to make up for the difference in handling. That is, adding an additional yaw torque to counter the handling properties changed by the difference in propulsion.

1.3 Motivation

When driving vehicles of different powertrain layouts, the lateral performance differ due to understeering properties. It is known that front-wheel-driven vehicles exhibit understeered characteristics, compared to a rear-wheel-driven vehicle that might be oversteered. This behaviour is illustrated in Figure 1.2a, where the steering response from a driver model is shown for three different powertrain layouts. The effect of reducing the roads friction coefficient is also shown for a all-wheel-driven vehicle. It can be seen that FWD requires a larger steering angle from the driver to clear the same corner, compared to AWD, which indicates the expected understeer behaviour. A similar change can be seen for lower friction as the steering angle increases for an all-wheel-driven vehicle on wet road. In this case, however, it takes longer for the driver to stabilise the vehicle. It can also be seen that the rear wheel driven vehicle has oversteered handling, since the steering wheel angle decreases with higher acceleration. The effect of this steering difference is visualised in Figure 1.2b. This shows that a vehicle that varies its power distribution between all four tyres will exhibit different steering behaviour depending on the current distribution. This can be seen as a disturbance from the drivers perspective as the vehicle will not always behave the same in the same situation.

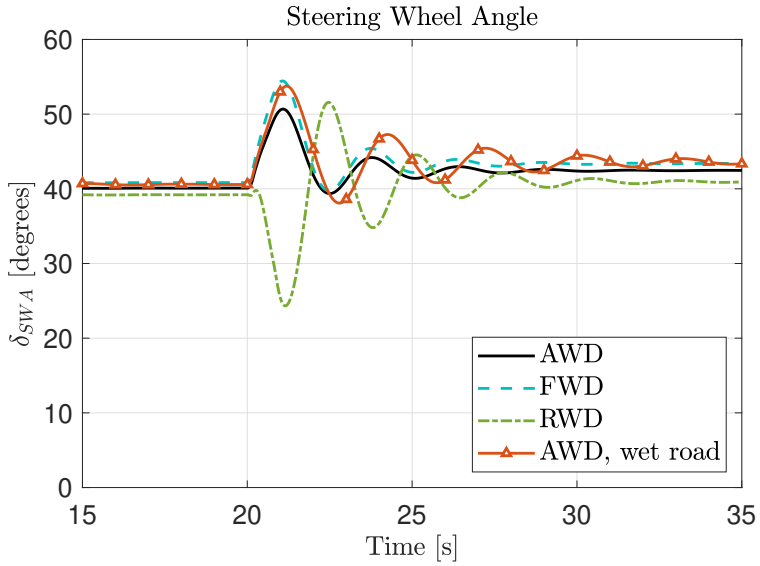

(a) Steering wheel angle for different powertrain layouts while cornering at 60 km/h, increasing to 65 km/h at 20 seconds.

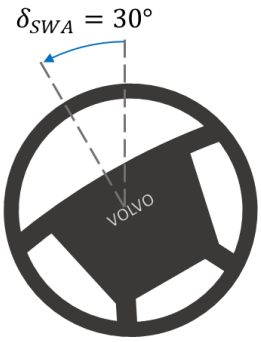

(b) Illustration of a steering wheel, turning with 30°.

1.4 Purpose

The purpose of this thesis is to assess the extent to which torque vectoring is capable of enhancing the lateral performance of a heavy electric vehicle. The thesis seeks to fulfil this purpose through answering the following research questions:

- How does torque vectoring using individually controlled wheels reasonably improve lateral performance of heavy electric vehicles, and to what degree?
- What control strategies are favourable when using this type of torque vectoring for heavy vehicles?
- How can lateral torque vectoring control improve the perceived consistency of the vehicle response?
- How does power loss optimisation between axles affect the vehicle behaviour and is torque vectoring able to mitigate any negative effects?
- What is the impact of torque vectoring on power consumption?

1.5 Scope and limitations

The following list highlights limitations and aspects that are not being considered in this thesis work:

- As there is no existing vehicle ready for testing of algorithms developed in this thesis, all controllers and models were implemented using vehicle models in simulation. More specifically Matlab Simulink.
- All states and variables used in the controller are assumed to be known or measurable and easily provided in the simulation environment. Consideration to only use realistic sensor measurements has been done.
- This thesis does not aim at making an optimised controller from a computing perspective. Execution time is not in focus, and computation optimisation strategies are not considered.
- The impact of calculation and communication delay from sensor reading to torque output has been neglected.
- The simulation was tested on a vehicle model (VTM) provided by Volvo.
- The thesis only treats solo tractors. The effect of articulated vehicles is not taken into account.

2
Vehicle Modelling

This chapter introduces the physics and vehicle dynamics principles on which the controllers are built upon. The longitudinal and lateral dynamics have been separated and are treated independently of each other. Vertical dynamics are also briefly touched upon as the thesis uses normal force estimation. The tyre models used are also presented, as well as properties of the electrical machines used. The vehicle parameters are specified in table 2.1. The thesis uses the ISO8855:2011 standard where applicable.

Table 2.1: Table of parameters describing the vehicle used for this thesis. Each parameter is described by name, denotation, unit and value.

Parameter	**Denotation**	**Unit**	**Value**
Air density	ρ	kg/m^3	1.2
Air resistance coefficient	c_d	1	0.59
Cornering stiffness, front	$C_{f\alpha}$	N/rad	2.5e5
Cornering stiffness, rear	$C_{r\alpha}$	N/rad	1.23e5
Frontal area	A_f	m^2	10
Gear ratio, Cruisability axle	gr_{crs}	Nm/Nm	4.5
Gear ratio, Startability axle	gr_{stb}	Nm/Nm	26
Gravitation	g	m/s^2	9.81
Mass	m	kg	6 918
Rolling resistance coefficient	c_r	N/N	0.008
Scrub radius	r_s	m	0.12
Track width, front	t_f	m	2.09
Track width, rear	t_r	m	1.85
Wheel base	L	m	3.7
Distance, CoG to front axle	L_f	m	0.9644
Distance, CoG to rear axle	L_r	m	2.7356
Wheel radius	r_w	m	0.47
Yaw inertia	I_{zz}	$kg \cdot m^2$	24 133

2.1 Tyre Dynamics

Tyres provide the interface between the vehicle and the road, which make their mechanics important in the dynamics of the vehicle. As tyres have elastic properties,

forces are highly nonlinear and difficult to model. Here, an introduction to tyre models will be presented as well as the concept of friction circle.

2.1.1 Longitudinal Tyre Slip

In the longitudinal direction, the tyre slip is commonly denoted as s_{ix} for an axle i. The definition for the slip is a ratio between the wheel hub speed and the tyre's rotational speed. Only considering pure longitudinal slip ($v_{wy} = 0$), the slip can be defined as

$$s_{ix} = \frac{r_w \cdot \omega_i - v_x}{|r_w \cdot \omega_i|} \tag{2.1}$$

where r_w is the tyre radius, ω_i is the rotational speed of the tyre and v_x is the vehicle's longitudinal speed. Not that this holds true for a driving tyre, but for a breaking tyre the denominator should be $|v_{ix}|$ instead.

2.1.2 Lateral Tyre Slip

The tyre slip angle is defined as the angular difference between the wheel hub direction and the direction of the wheel's velocity. Denoted as α_i, the slip angle for a steerable axle i is defined according to Figure 2.1.

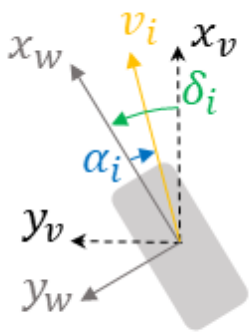

Figure 2.1: Illustration of tyre slip on the front axle. Subscript v indicates vehicle coordinate system, while subscript w indicates wheel coordinate system. Vectors are not to scale.

Using trigonometry, the slip angle can be defined as:

$$\alpha_i = \delta_i + \arctan(\frac{v_{iwy}}{v_{iwx}}) \tag{2.2}$$

where δ_i is the steering angle and v_{iwx}, v_{iwy} are the wheel hub velocity vector in x and y direction of the wheel coordinate system respectively. Note that for an unsteered

axle the same equation is valid, but δ_i becomes zero. The definition of slip in the lateral direction, lateral slip, is expressed as a ratio:

$$s_{iy} = \frac{v_{iwy}}{|v_{iwx}|} = tan(\alpha_i) \tag{2.3}$$

2.1.3 Combined Slip

Combined slip is present when the vehicle is accelerating or braking while cornering. As the name suggests, this results in a combination of longitudinal and lateral slip on the tyres. A combined slip model is used to estimate the maximal forces F_x and F_y as a result of the corresponding slip s_x and s_y. Assuming isotropic friction and tyre deformation, an estimation of maximal total tyre force can be expressed as:

$$\mu F_{iz} = \sqrt{F_{ix}^2 + F_{iy}^2} \tag{2.4}$$

where μ is the friction coefficient between road and tyres and F_z is the vertical load on the tyre. This is often referred to as the friction circle as can be seen in Figure 2.2. Note that tyres generally are unsymmetrical in the x and y direction, and that the estimation hence would take the form of an ellipse rather than a circle. For this thesis however, the dynamics are assumed to be isotropic.

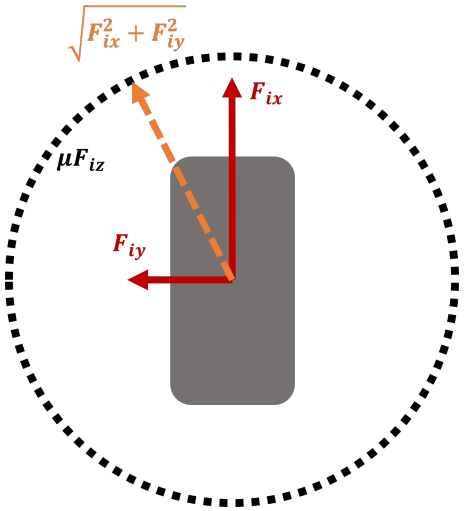

Figure 2.2: Illustration of friction circle.

By rearranging the friction circle expression, an estimation of maximal longitudinal tyre force can be calculated, given that the lateral and vertical tyre forces are known:

$$F_{ix,\mu Max} = \sqrt{(\mu F_{iz})^2 - F_{iy}^2} \tag{2.5}$$

where $F_{ix,\mu Max}$ is the maximal longitudinal force before the tyre starts sliding according to the friction circle. For this thesis, the lateral and vertical tyre forces and friction coefficient are assumed to be available through measurements or estimations. See equations 2.38 and 2.45 for implementations of lateral and vertical force

estimation used in this thesis.

An interesting discovery found through simulations is that an estimation of F_y gave better results than that of measured data. The reason for this is that the lateral force is reduced as the tyre starts sliding, falsely suggesting that the friction limits are no longer being violated. Estimations on the other hand will either have F_y stay constant or increase even when the tyre is sliding. This way, the controller using the estimations will understand that the friction limits are being violated.

Separating the longitudinal and lateral forces and using the estimated F_y (from equation 2.38) the following two equilibrium equations are found:

$$\frac{F_{iz}}{g}\left(\dot{v_{ix}} - \omega_z v_{iy}\right) = F_{ix,\mu Max} \tag{2.6}$$

$$F_{iy} = \frac{F_{iz}}{g}\left(a_y + L_j\dot{\omega_z}\right) \tag{2.7}$$

where ω_z is measured yaw rate, v_{iy} is measured lateral velocity, F_{iz} is the estimated normal force on each tyre and a_y is measured lateral acceleration. L_j represents the distance from CoG to the front or rear axle, depending on which tyre force is being calculated. The maximum additional force that can be exerted on the tyre can be seen as the maximum longitudinal force with respect to friction minus the force caused by the yaw rate. Combining equation 2.6 and 2.5:

$$\frac{F_{iz}}{g}\dot{v_{ix}} = F_{ix,Max} = F_{ix,\mu Max} + \omega_z v_{iy}\frac{F_{iz}}{g} \tag{2.8}$$

The former equation can be slightly modified by replacing the measured yaw rate with a yaw rate reference, estimated from the steering angle δ_f. Since the yaw rate is constantly being corrected to match the yaw rate reference this modification will not make a significant difference, but should make the estimations react slightly faster to change of yaw rate. The final expression for maximal longitudinal tyre forces can now be expressed as

$$F_{ix,Max} = \sqrt{(\mu F_{iz})^2 - (\frac{F_{iz}}{g}\cdot a_y)^2} + \frac{F_{iz}}{g}\cdot\omega_{z,ref}\cdot v_{iy} \tag{2.9}$$

where $\omega_{z,ref}$ is the reference yaw rate and $i = fl, fr, rl, rr$ indicates each tyre.

2.1.4 Safe Operating Limits

As slip ratio increases, lateral forces will naturally increase as well, which changes the characteristics of the longitudinal tyre dynamics. Longitudinal forces are considered independent of the lateral slip up to approximately 50% of the friction limit, as seen in the friction circle [8]. This will be reached when the magnitude of the resulting force equals half of the friction circle radius. The total planar force is then split up depending on lateral versus longitudinal slip,

$$\begin{bmatrix} F_x \\ F_y \end{bmatrix} = \begin{bmatrix} s_x \\ -s_y \end{bmatrix}\frac{F_{xy}}{s_{xy}} \tag{2.10}$$

Where s_{xy} is the combined slip vector and F_{xy} is the estimated total force based on the vertical load, the friction and current slip. This results in lateral forces decreasing when longitudinal forces increase, which is a problem when approaching the friction limit.

As mentioned previously, in reality the maximum lateral forces that can occur before sliding are lower than the maximum longitudinal force due to the anisotropic nature of tyres. This stems both from the thread patterns, camber angles and the general shape of a tyre [8]. In addition to this, once sliding occurs, the static friction estimation is no longer accurate and the kinetic friction (or slip friction) is lower.

As the controller constructed in this thesis is not mainly meant as a traction controller, a limit is put on the maximum percentage use of the friction circle to account for changes in friction, which will be referred to as the friction confidence.

$$\mu_{model} = \mu_{est} \cdot \mu_{confidence} \tag{2.11}$$

An initial value for the confidence coefficient is 80-85% to avoid exiting the linear region.

2.1.5 Linear Tyre Model

Linear tyre models describe a linear relationship between the tyre slip and the force it generates and are valid for lower slip magnitudes. As the vehicle mostly operate under low slip conditions, it is an accurate model for the majority of control situations. In the lateral direction, the forces generated are described through the cornering stiffness C_α. The relationship between lateral forces and the cornering stiffness is expressed as:

$$F_y = -C_\alpha \cdot \alpha \tag{2.12}$$

The value of the cornering stiffness changes with tyre types, tyre treads, tyre pressure and vertical load, among others [9]. During steady state driving, the cornering stiffness is largely unchanged. However, it will change based on how the vehicle is loaded, and if the vehicle accelerates or decelerates. As this thesis focus on countering dynamic behaviour, a static cornering stiffness will not be sufficient to accurately calculate the tyre forces. To improve on this, a varied cornering stiffness based on vertical axle load and a cornering stiffness coefficient is used [9]. For an axle j, the cornering stiffness $C_{j\alpha}$ is calculated through the tyre loads as:

$$C_{j\alpha} = CC_{j\alpha} \left(F_{jlz} + F_{jrz}\right) \tag{2.13}$$

Where subscript jlz and jrz indicates the vertical load on the left and right tyre of axle j respectively.

2.2 Longitudinal Dynamics

When considering purely longitudinal dynamics, the forces acting on the vehicle are resistances in the form of rolling resistance, air resistance and gravitational resis-

tance due to road gradient. There are also forces created by propulsion to counter the resistances and accelerate the vehicle. The tyre will either provide a positive longitudinal force if accelerating, or a negative if braking. An image of how all the forces act on the vehicle as well as the road gradient are illustrated in Figure 2.3.

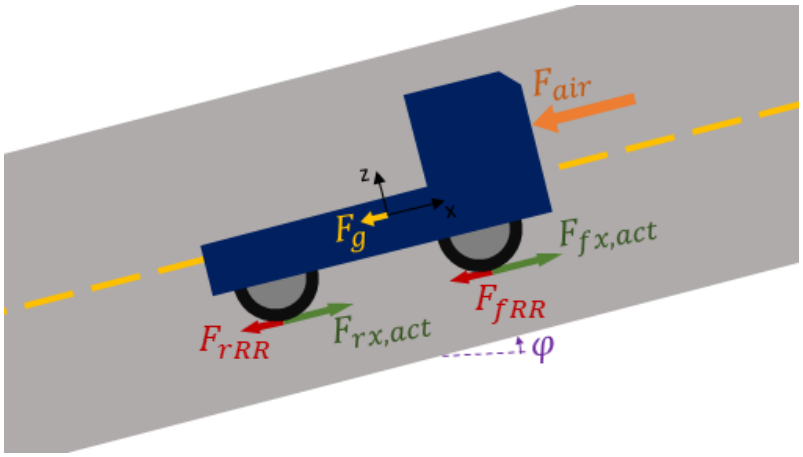

Figure 2.3: Solo tractor driving uphill. Forces affecting the tractor in longitudinal direction is drawn, as well as the road gradient. Note that the forces are not to scale.

The rolling resistance affecting the vehicle happens due to deformity and hysteresis of the rubber in the tyres. The rolling resistance is usually regarded constant over different speeds and is calculated as

$$F_{iRR} = c_r \cdot F_{iz} \tag{2.14}$$

where c_r is the rolling resistance coefficient, and F_{iz} is the vertical load on the tyre.

Air resistance is a force that acts on the vehicle as a response to the vehicle's speed and aerodynamic features. The resistance is calculated as

$$F_{air} = \frac{1}{2} \cdot \rho \cdot c_d \cdot A_f \cdot v_x^2 \tag{2.15}$$

The last force to consider is the gravitational resistance. This is a function of vehicle mass and road gradient. As the road gradient increases (driving uphill), the gravitational resistance increases. If, on the other hand, the road gradient becomes negative (driving downhill) the gravitational force accelerates the vehicle. The gravitational resistance is calculated as

$$F_g = m \cdot g \cdot sin(\varphi) \tag{2.16}$$

where m is the vehicle mass, g is the gravitational constant, and φ is the road gradient.

The force equilibrium for all the longitudinal forces can now be presented as

$$m\dot{v_x} = \sum_i (F_{ix,act} - F_{iRR}) - F_{air} - F_g \tag{2.17}$$

where $F_{x,act}$ is the resulting actuator force from electric machines and brakes on the front and rear axle, calculated as:

$$F_{fx,act} = \left((T_{fl,EM} + T_{fr,EM})\, gr_{crs} + T_{fl,brake} + T_{fr,brake} \right) r_w \tag{2.18}$$

$$F_{rx,act} = \left((T_{rl,EM} + T_{rr,EM})\, gr_{stb} + T_{rl,brake} + T_{rr,brake} \right) r_w \tag{2.19}$$

$$F_{x,act} = F_{fx,act} + F_{rx,act} \tag{2.20}$$

Here, T_{EM} is torque from the motors and T_{brake} torque form the brakes, r_w is the wheel radius, and gr_{crs} and gr_{stb} is the gear ratio for the cruise and startability axle respectively.

2.3 Lateral Dynamics

The state space model used for the controller in this thesis is based on a single track model (also known as bicycle model), which can be seen in Figure 2.4. Here, important variables and parameters are drawn out. The state space model uses two states (β and ω_z) and the derivation of those states will be shown in this section.

2.3.1 Body Slip Angle

The yaw rate and body slip angle (also known as vehicle side slip angle) are calculated from the bicycle model in Figure 2.4. Since the bicycle model only has two tyres, the tyres of each axle on the four-wheel vehicle are grouped together and summed up, while the steering angle on the front axle is averaged. If the steering angle is assumed to be low, the lateral forces acting on the vehicle can be described with the yaw rate and lateral acceleration according to

$$m(\dot{v_y} + v_x \cdot \omega_z) = \sum_i F_{iy} \tag{2.21}$$

where $i = fl, fr, rl, rr$ corresponds to the four tyres of the vehicle. This is helpful for model-based controllers, especially when hard braking, as the load on the front axle increases significantly and the load on the rear axle decreases accordingly. If the body slip angle is small it can be defined as:

$$\beta = \frac{v_y}{v_x} \tag{2.22}$$

If the longitudinal acceleration is assumed to be low (constant v_x), the equation

$$m \cdot v_x \left(\frac{\dot{v_y}}{v_x} + \omega_z \right) = m \cdot v_x \left(\dot{\beta} + \omega_z \right) = \sum_i F_{iy} \tag{2.23}$$

is obtained by substituting the longitudinal velocity and extracting v_x in equation 2.21. This shows an expression for the derivative of the body slip angle, which

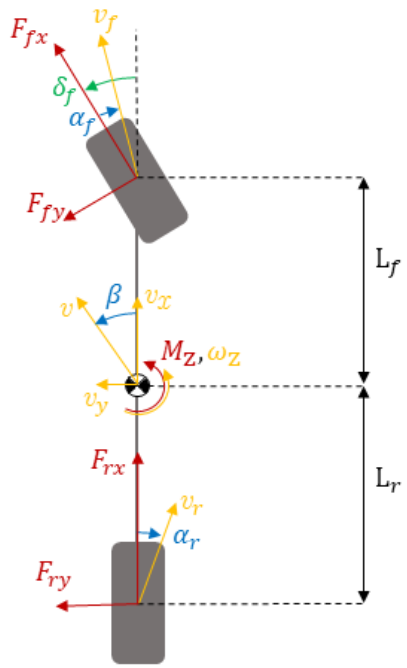

Figure 2.4: Single track model of the vehicle with important parameters drawn out. Velocities and angular velocities are drawn with yellow arrows; forces and moments are drawn with red arrows; and angles are drawn with blue arrows, with the exception of the steering angle which is drawn in green for clarity. Note that the vectors are not to scale.

is useful for the state space model. By extracting the body slip angle derivative, the following expression is found:

$$\dot{\beta} = \frac{\sum_i F_{iy}}{m \cdot v_x} - \omega_z \tag{2.24}$$

The lateral forces $\sum_i F_{iy}$ acting on each tyre depend on the tyre slip angle and tyre cornering stiffness of the respective axles. The lateral slip angles α_f and α_r can be seen in Figure 2.4, drawn in blue. They are calculated through the following equations (Note that the front slip angle depends on the steering angle):

$$\alpha_f \approx \left(\beta + \frac{L_f \cdot \omega_z}{v_x}\right) - \delta_f \tag{2.25}$$

$$\alpha_r \approx \left(\beta - \frac{L_r \cdot \omega_z}{v_x}\right) \tag{2.26}$$

Assuming that the tyres behave linearly, as previously described in equation 2.12, the total lateral force acting on the vehicle can be summarised as

$$\sum_i F_{iy} = -\left(C_{f\alpha} + C_{r\alpha}\right)\beta - \frac{C_{f\alpha} \cdot L_f - C_{r\alpha} \cdot L_r}{v_x}\omega_z + C_{f\alpha} \cdot \delta_f \tag{2.27}$$

by combining the expressions for total lateral force (equation 2.23), front tyre slip angle (equation 2.25) and rear tyre slip angle (equation 2.26). Using this definition for the lateral force on the vehicle and combining with the previous expression in

equation 2.24, the derivative of the body slip angle can now be expressed as

$$\dot{\beta} = -\frac{C_{f\alpha} + C_{r\alpha}}{m \cdot v_x}\beta + \left(\frac{-L_f \cdot C_{f\alpha} + L_r \cdot C_{r\alpha}}{m \cdot v_x^2} - 1\right)\omega_z + \frac{C_{f\alpha}}{m \cdot v_x}\delta_f. \tag{2.28}$$

This expression for the derivative of the body slip angle will later be used in the controller's state space model.

2.3.2 Yaw Rate

The derivative of yaw rate is found by using Newton's second law on rotational bodies, according to

$$I_{zz} \cdot \dot{\omega_z} = M_z = F_{fy} \cdot L_f - F_{ry} \cdot L_r \tag{2.29}$$

where I_{zz} is the vehicle's moment of inertia around the vertical axis. Rearranging this equation and, again, inserting the expression of total lateral force (equation 2.27), an expression for yaw rate derivative is found:

$$\dot{\omega_z} = -\frac{L_f \cdot C_{f\alpha} - L_r \cdot C_{r\alpha}}{I_{zz}}\beta - \frac{L_f^2 \cdot C_{f\alpha} + L_r^2 \cdot C_{r\alpha}}{I_{zz} \cdot v_x}\omega_z + \frac{L_f \cdot C_{f\alpha}}{I_{zz}}\delta_f. \tag{2.30}$$

2.3.3 Rollover

Rollover is what happens when the lateral forces on a vehicle are large enough that the roll moment generated causes the vehicle to tip over. This is significantly more dangerous on a truck, as the centre of gravity is much further above the ground, causing the lateral forces from the tyres to generate a larger moment on the vehicle.

There are three different types of rollover:

- Hitting an edge, such as pavement, known as tripped roll-over.
- Un-tripped rollover in steady state, caused by high tyre forces.
- Transient rollover, caused by resonating turns or a sudden change in latera acceleration.

The focus here will be on un-tripped rollover, and more specifically steady state rollover. Rollover will be defined as all wheels from one side lifting from the ground, as it is one of the easier limits to calculate and a limit that should never be surpassed when driving either way. In Figure 2.5, important forces and parameters are defined.

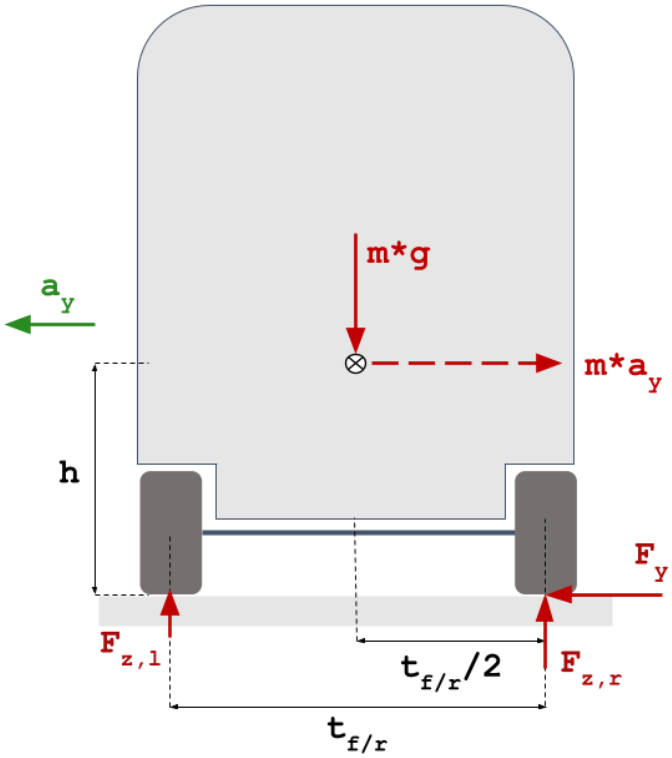

Figure 2.5: Lateral forces on a heavy vehicle in a left hand turn.

It can be seen that the lateral acceleration will cause a roll moment according to

$$M_{x,a_y} = m \cdot a_y \cdot h \tag{2.31}$$

where M_{x,a_y} is the roll moment due to lateral acceleration. There is also an additional moment generated by the change in load distribution. More accurately, the change in load distribution itself happens due to the moment generated by the lateral tyre forces. When there is no more weight to shift, the lateral moment causes the vehicle to rotate. Assuming a left hand turn:

$$M_{x,F_z} = (F_{flz} - F_{frz})\frac{t_f}{2} + (F_{rlz} - F_{rrz})\frac{t_r}{2} \tag{2.32}$$

where M_{x,F_z} is the roll moment due to vertical load and $\sum_i F_{iz} = m \cdot g$. A simple limit can then be seen as the moment generated with all the weight on one side.

$$M_{x,F_z} = M_{x,a_y} = m \cdot g\frac{t_f/2 + t_r/2}{2} = m \cdot a_{y,crit} \cdot h \implies a_{y,crit} = g\,\frac{t_f + t_r}{4 \cdot h} \tag{2.33}$$

As a rule of thumb, rollover limit for heavy vehicles vary between $0.3g$ and $0.5g$ lateral acceleration.

2.4 Torque Vectoring

Torque vectoring is the act of allocating different torque on the left and right wheels to modify the vehicle behaviour with the purpose of improving stability, performance

or resource usage (such as energy or tyre wear). With a distributed powertrain layout as previously explained, it is possible to control each wheel individually, ensuring the vehicle does not slide, and that power can be distributed based on need. Torque vectoring implementation can vary greatly in complexity from, for example, a proportional controller, to something more complex, such as having target states or mathematical models of the vehicle. Some common targets to optimise with torque vectoring are: Power use [10], [11]; tyre wear [12], [13]; cornering speed/performance [14], [15]; traction control [16], [17]; and stability control [11], [18].

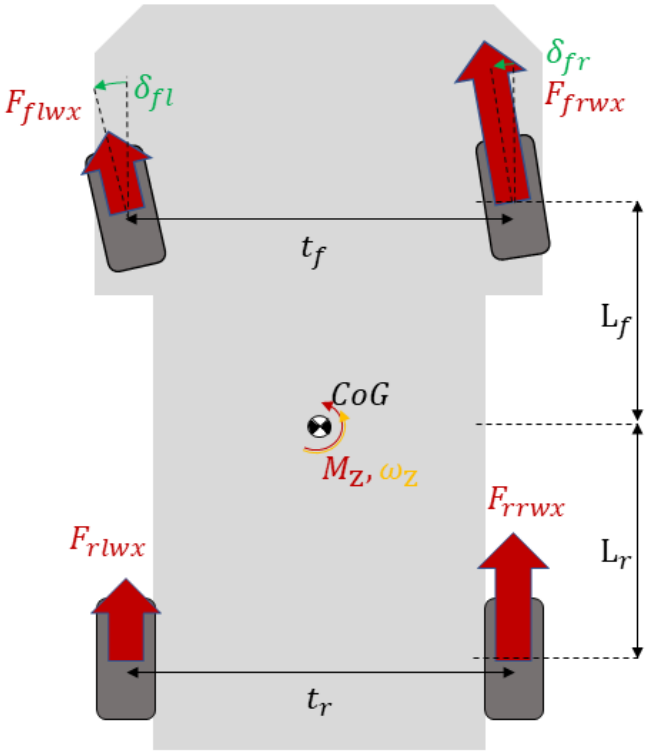

Figure 2.6: Example of forces generated through torque vectoring. The difference in forces generated from the left and right side causes a yaw moment on the vehicle, changing the dynamics of the unit.

As mentioned in Chapter 2.1.3, individually controlled motors can provide additional grip control. Since the load transfers to the outer side of the vehicle in a curve, it is possible to distribute the longitudinal forces to the outer wheels to reduce slip and tyre wear.

Moving the force distribution to different axles and sides generates an additional yaw moment. This can be a negative consequence of different grip levels on different wheels when braking or accelerating, such as split-μ surfaces. This can cause the vehicle to rotate and possibly spin out of control, if not accounted for.

The yaw moment generated can also be done intentionally to help the vehicle steer, which is the focus of this thesis. The yaw rate generated will depend on the track

width of the vehicle, the steering angle, the forces generated and the inertia of the controlled unit. In Figure 2.6, angles and distances used to calculate the yaw moment are presented. From these definitions, the following equations can be found:

$$M_{fz} = \left(F_{frwx} \cdot \cos(\delta_{fr}) - F_{flwx} \cdot \cos(\delta_{fl})\right) \frac{t_f}{2} + \left(F_{frwx} \cdot \sin(\delta_{fr}) - F_{frwx} \cdot \sin(\delta_{fl})\right) L_f \tag{2.34}$$

$$M_{rz} = (F_{rrwx} - F_{rlwx}) \frac{t_r}{2} \tag{2.35}$$

$$\dot{\omega_z} = \frac{M_{fz} + M_{rz}}{I_{zz}} \tag{2.36}$$

Equation 2.34 can be simplified at low steering angles ($\cos(\delta) \approx 1$), which is often true for heavy vehicles at higher speeds, where the torque vectoring would operate.

$$M_{fz} = F_{frwx} \frac{t_f}{2} - F_{flwx} \frac{t_f}{2} \tag{2.37}$$

This thesis mainly focuses on stability control to improve vehicle predictability, but uses the remaining degrees of freedom to reduce power consumption. Tyre wear and direct performance is not investigated, but preemptive traction control is considered for stability purposes. Another effect of torque vectoring that should be considered is rollover. This is due to the increased ability to suddenly increase the yaw moment and hence also increase the lateral acceleration.

2.5 Force Estimation

This paper explores the use of lateral and vertical force estimation instead of direct measurements. The equations used to calculate these estimations are found in this subsection, together with a comparison to the simulation outputs.

2.5.1 Lateral Force Estimation

Lateral force estimation for each wheel is based on vertical force estimations (see next subsection) and lateral acceleration measurements, according to

$$F_{iy} = \frac{F_{iz}}{g} \left(a_y + L_j \dot{\omega}_z\right). \tag{2.38}$$

The yaw acceleration has to be added, as each wheel will have an additional acceleration depending on the yaw acceleration of the vehicle. In Figure 2.7, the force estimations are plotted against simulation measurements. There it is possible to see that the general dynamics are well captured, although there is an offset as the steering angle increases.

2.5.2 Vertical Force Estimation

When calculating the friction circle per wheel, it is important to have a good estimation of the normal force on each tyre. It is possible to actively estimate the normal

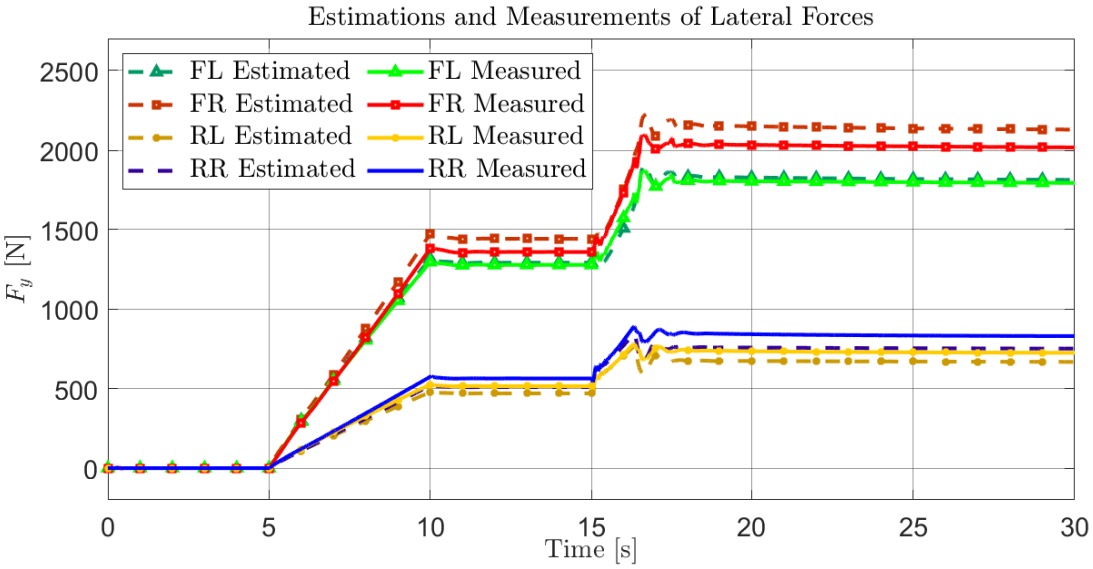

Figure 2.7: Lateral force estimation compared to simulation measurements. The test is conducted at 10 m/s with increasing steering angle from 0 deg to 0.02 deg between 5 s and 10 s. There is also a speed increase with 2 m/s at 10 s.

force distribution from the momentary lateral and longitudinal accelerations. There are three parts to this equation: static distribution, longitudinal- and lateral load transfer. The static weight distribution is calculated as

$$F_{fz}^{stat} = \frac{m \cdot g \cdot L_r}{2 \cdot L} \qquad (2.39) \qquad F_{rz}^{stat} = \frac{m \cdot g \cdot L_f}{2 \cdot L} \qquad (2.40)$$

where F_{fz}^{stat} and F_{rz}^{stat} correspond to the static normal force on the front and rear axle tyres respectively. The longitudinal load transfer is calculated as the static mass times a load coefficient. This coefficient is vehicle dependent and was tuned to the simulation of this thesis as $\frac{0.4}{1}$ and $\frac{0.9}{1}$ for the front and rear axles respectively. This corresponds to a 40 % load transfer at 1 g for the front axle and a 90 % load transfer at 1 g for the rear axle. With these coefficients, the load transfer equations become

$$F_{fz}^{long} = a_x \frac{m \cdot Lr}{2 \cdot L} \cdot \frac{0.4}{1} \qquad (2.41) \qquad F_{rz}^{long} = a_x \frac{m \cdot Lf}{2 \cdot L} \cdot \frac{0.9}{1}. \qquad (2.42)$$

Similar to the longitudinal case, the lateral load transfer is also tuned with vehicle specific coefficients. For this thesis, $\frac{1}{1}$ was used for the front axle and $\frac{0.75}{1}$ was used for the rear axle. This corresponds to a 100 % load transfer at 1 g and 75 % load transfer at 1 g respectively. The lateral load transfer equations look like

$$F_{fz}^{lat} = a_y \frac{m \cdot Lr}{2 \cdot L} \cdot \frac{1}{1} \qquad (2.43) \qquad F_{rz}^{lat} = a_y \frac{m \cdot Lf}{2 \cdot L} \cdot \frac{0.75}{1}. \qquad (2.44)$$

With both the static, longitudinal and lateral equations in place, the total normal force estimation looks like the following:

$$F_z = \begin{bmatrix} F_{flz} \\ F_{frz} \\ F_{rlz} \\ F_{rrz} \end{bmatrix} = \begin{bmatrix} F_{fz}^{stat} - F_{fz}^{long} - F_{fz}^{lat} \\ F_{fz}^{stat} - F_{fz}^{long} + F_{fz}^{lat} \\ F_{rz}^{stat} + F_{rz}^{long} - F_{rz}^{lat} \\ F_{rz}^{stat} + F_{rz}^{long} + F_{rz}^{lat} \end{bmatrix}. \tag{2.45}$$

The estimations for each tyre are compared and plotted in Fig. 2.8. It is clear to see that the estimations follow the measurements well during more static conditions. It is also noticeable that the estimations are less oscillating than the measurements, which is desirable from a control perspective.

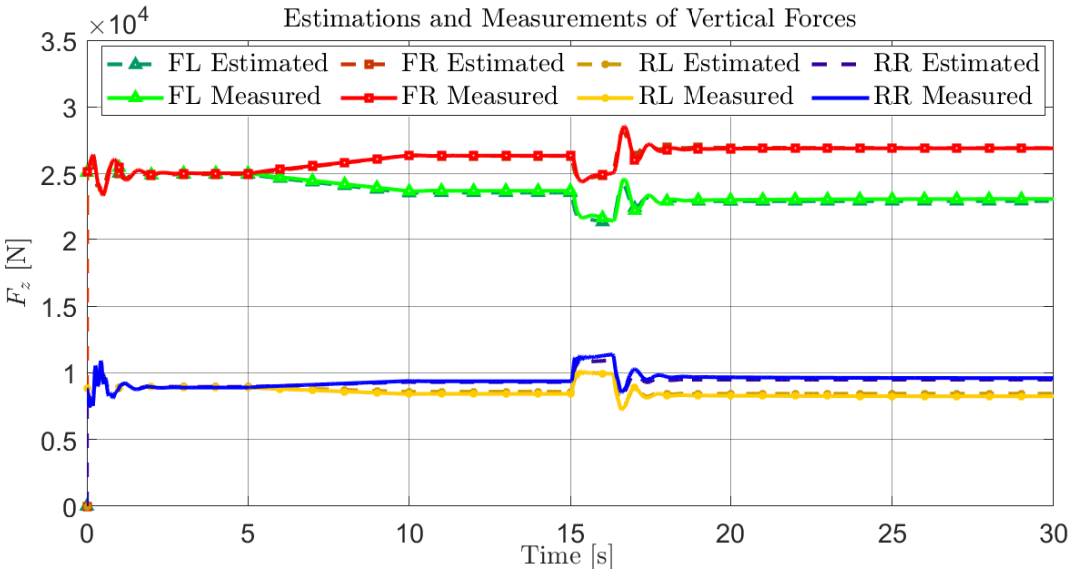

Figure 2.8: Vertical force estimation compared to simulation measurements. The test is conducted at 10 m/s with increasing steering angle from 0 deg to 0.02 deg between 5 sec and 10 sec. There is also a speed increase with 2 m/s at 10 s.

2.6 Electrical Motors

The vehicle plant model used in this thesis had four wheels with propulsion that were individually powered with one motor each. The vehicle layout and EM placement can be seen in Figure 1.1. The front axle used two PMSMs (Permanent-Magnet-Synchronous-Machine) for constant speed highway driving, while the rear utilised two IMs (Induction-Machine) for additional power when needed.

The motivation for the choice of machines was based on the fact that PMSMs generally are more efficient than IMs, making them suitable for continuous use. IMs on the other hand, have no permanent magnet losses when idle [19], which the PMSM suffers from. This makes IM motors more suitable for the sporadic use of the rear axle [20].

Using the terminology introduced in [7], the front axle is also called the cruise axle, and the rear axle may be referred to as the startability or start axle. To fulfill their respective tasks, the cruise and start axle work with different gear ratios. The goal was to select a single gear ratio for each axle, such that the vehicle can reach and maintain a top speed of 90 km/h. As the cruise axle works with higher speeds, a low gear ratio of 4.5 was selected. The rear axle, on the other hand, deals with higher loads and was utilising a much higher gear ratio of 26. As the main focus of the thesis was to analyse steering predictability, the gears are assumed to be ideal (no power loss). All parameters for the two motor types, and the their respective gear ratios, can be seen in table 2.2 below.

Table 2.2: Parameters for each of the two motor types.

	PMSM	IM
Power	200 kW	180 kW
Max Torque	790 Nm	329 Nm
Max speed	340 rad/s	1 361 rad/s
Gear Ratio	4.5	26

In order to work with the propulsion forces, it is convenient to translate the motors torque outputs to longitudinal forces. This is done similarly to equations 2.18 and 2.19, but split up on each tyre as:

$$\begin{aligned} F_{flx,EM} &= gr_{crs}\frac{T_{fl,EM}}{r_w} & F_{frx,EM} &= gr_{crs}\frac{T_{fr,EM}}{r_w} \\ F_{rlx,EM} &= gr_{stb}\frac{T_{rl,EM}}{r_w} & F_{rrx,EM} &= gr_{stb}\frac{T_{rr,EM}}{r_w} \end{aligned} \tag{2.46}$$

where T is the torque output from the electrical machines, r_w is the wheel radius and gr are gear ratios for cruise and start axle. All of these forces can now be summed up to get the general propulsion force that is acting on the vehicle:

$$F_{x,EM} = F_{flx,EM} + F_{frx,EM} + F_{rlx,EM} + F_{rrx,EM}. \tag{2.47}$$

2.6.1 Motor Efficiency and Output limits

Electric motors have a set max torque, max speed and max power output. Because of this, the maximum torque output for an electric motor is constant for a set speed, until the maximal power output is reached. The torque output is then reduced for increased speeds as the maximal power output is still the limiting parameter. In figure 2.9, the efficiency contours of the PMSM and IM machines used in this thesis are presented. It can be seen that the most efficient operating points for the two electrical machines are not located at zero torque. Instead, the PMSM has its most efficient operating point at maximal power output, while the IM should operate at around half of its peak torque for optimal efficiency. The reason for this is that both machines suffer from constant losses that are present even when idle.

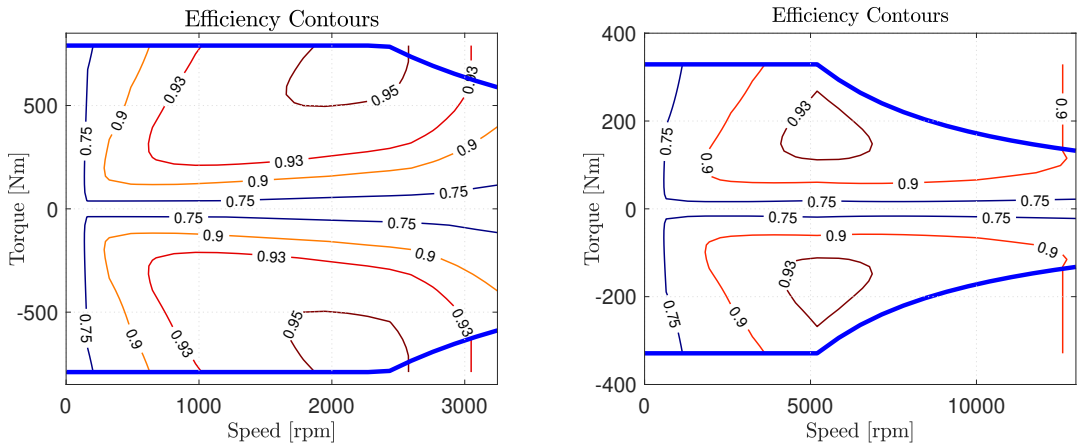

(a) PMSM **(b)** IM

Figure 2.9: Efficiency contours of a PMSM motor and a IM motor.

The efficiency of an electrical machine is calculated as the ratio between input and output power as:

$$\eta = \frac{P_{out}}{P_{in}} \tag{2.48}$$

If the machines don't produce any output power but still use energy, the efficiency is very low. On the other hand, if the output power becomes very high, the constant losses will not be as noticeable. Besides the constant losses, the machines also suffer from variable power losses. These depend on the output torque and speed, and vary between different type of machines, hence the different characteristics in the figure.

The motor models used in the thesis are similar to that used in [21]. Motor limits are calculated from a generated lookup table [22], depending on the current wheel speed:

$$\begin{aligned} F_{i,EM,Min} &= r_w \cdot T_{EM,MinLim}(\omega_i) \\ F_{i,EM,Max} &= r_w \cdot T_{EM,MaxLim}(\omega_i) \end{aligned} \tag{2.49}$$

$$\begin{aligned} F_{i,brake,Min} &= r_w \cdot T_{brake,MinLim}(\omega_i) \\ F_{i,brake,Max} &= 0 \end{aligned} \tag{2.50}$$

Where i = fl, fr, rl, rr. While electric motors are much more responsive than combustion engines, there is still a rate of change limit. Brakes however, are much slower and takes a longer amount of time to reach maximum retardation force. This has to be accounted for when calculating torques in the controller. The model used is a simple model proposed by [23].

$$\begin{aligned} \dot{T}_{EM} &= \frac{T_{EM,req} - T_{EM}}{\tau_{EM}} \\ \dot{T}_{brake} &= \frac{T_{brake,req} - T_{brake}}{\tau_{brake}} \end{aligned} \tag{2.51}$$

Configuring this to fit discrete time, it is possible to find the maximal positive and negative rate of change, so that the limits are not exceeded:

$$\begin{aligned} T_{EM,RateMin}[k+1] &= \frac{T_{EM,Min} - T_{EM}[k]}{\tau_{EM}} T_s \\ T_{EM,RateMax}[k+1] &= \frac{T_{EM,Max} - T_{EM}[k]}{\tau_{EM}} T_s \\ T_{brake,RateMin}[k+1] &= \frac{T_{brake,Min} - T_{brake}[k]}{\tau_{brake}} T_s \\ T_{brake,RateMax}[k+1] &= \frac{T_{brake,Max} - T_{brake}[k]}{\tau_{brake}} T_s \end{aligned} \tag{2.52}$$

For the purpose of setting saturation limits, the rate of change can be set as a limit, assuming minimum or maximum torque request is being sent.

2.6.2 Power Loss

In this thesis, power loss was defined as the losses that occur in an electrical motor due to heat dissipation, similar to [21]. In other words, power loss is the energy to the motors that do not contribute to motor output. Parts of the motor that was taken into account for power loss was losses in the copper, iron and windage losses.

To understand and use the individual motors' power loss characteristics, a mapping of each motor's power loss was used. The mapping maps a combination of motor speed and motor torque to instantaneous power loss. This creates a three dimensional surface made out of data points, representing the power loss for each combination of speed and torque. These data points can be seen in Figure 2.10 for both the PMSM and IM motors. Here, it is possible to see the difference in how much torque the IM motors can output compared to the much more narrow surface from the PMSM motors. Note that these are specific to these machines being mounted with respective gear ratios.

The figure shows a good overview of the motors' characteristics and how they compare for all cases. To further illustrate the difference at specific motor speeds, the graphs in Figure 2.11a and Figure 2.11b below illustrate two separate driving scenarios. The former shows the power loss for both motors at a speed of 30 km/h and different torques. Here it can be seen that the PMSM motors on the cruise axle are actually less efficient than the IM motors on the start axle when high torque is needed. This is due to the low speed, for which the start axle works best. The cruise axle works better during higher speeds, which can be seen in the latter figure. Here, the PMSM motors of the cruise axle show a lower power loss compared to the start axle's IM motors. In the actual driving case, two of each motor may be active and contribute with power losses at the same time. This means that the vehicle can use a combination of all four machines to minimise the power loss and not only one or the other.

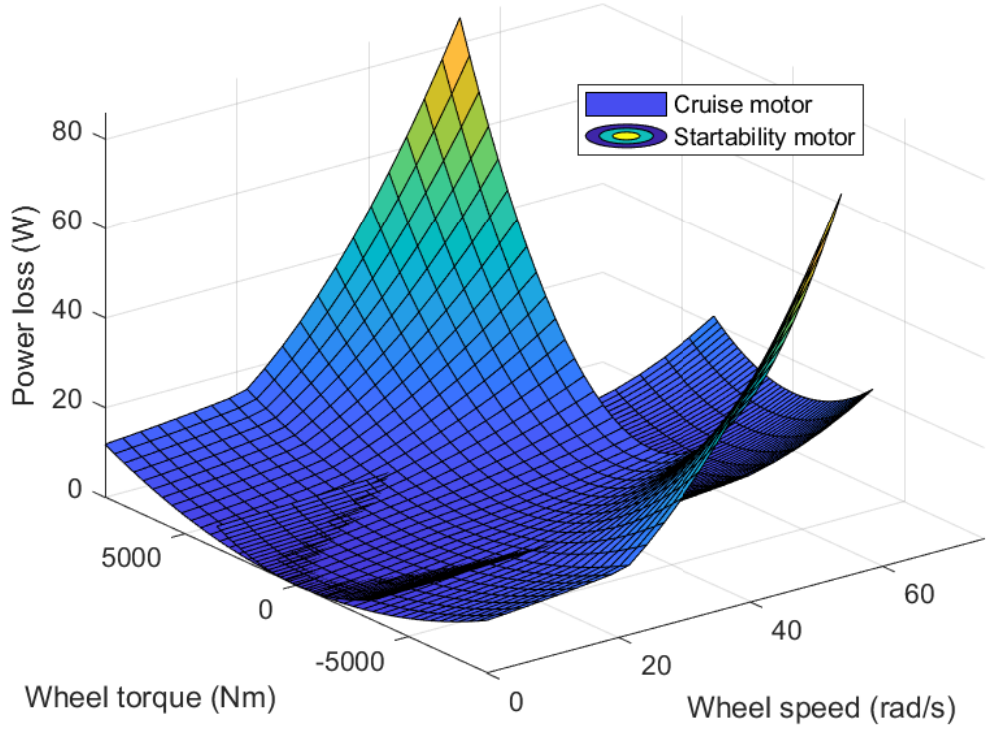

Figure 2.10: Power loss mapping of the startability and cruise motors. The startability motor has a gear ratio of 26 and the cruise motor has a gear ratio of 4.5.

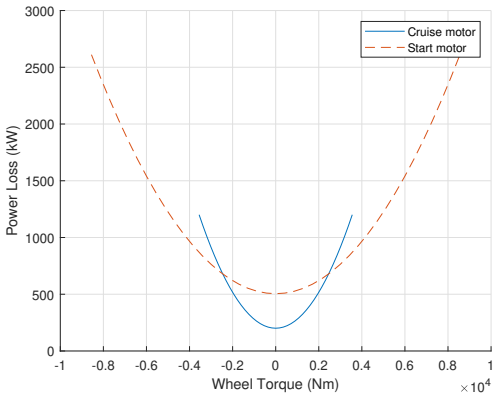

(a) Power loss at 30 km/h

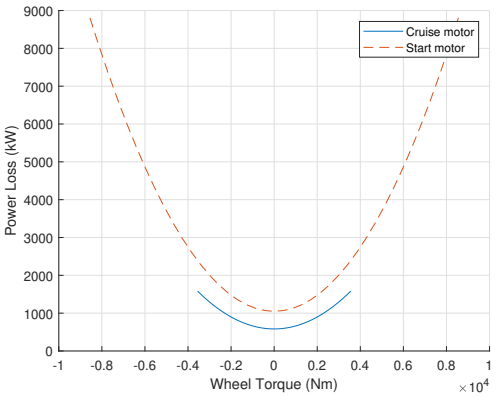

(b) Power loss at 70 km/h.

3
Steering Feel

A driver's preferred vehicle response is a subjective measure, which makes it hard to quantify. It also makes it difficult to model a general purpose or objective driver model. This thesis hence analyses the general driving experience through a literature study and expert interviews. Statistics for accidents have been analysed to model driver response for extreme scenarios. This chapter is a study of possible performance measures and affecting parameters, and not all parameters analysed are tested in simulation.

3.1 Previous works

In [24], a study was done to relate instrumental properties of a heavy truck to steering feel, which was characterised by nine dimensions, describing the steering system. The nine dimensions are:

- Stability ("wobbliness")
- Steering wheel resistivity
- Play (deadband)
- Road feel
- Response (time delays)
- Response (accuracy)
- Steering ratio
- Jerk
- Steering wheel return

Out of these nine indications, only four are deemed to be affected by torque vectoring. To create a predictable and comfortable steering feel, the dimensions of steering ratio, jerk, steering wheel return and steering response in terms of accuracy should be considered.

The study conducted a survey with truck drivers to relate these dimensions with instrumental values. It was found that some of the most important measures for these dimensions are: bandwidth, time delay, torque gradient and steering gradient. Out of these, the torque gradient and steering gradient are indicated as the most possible to affect from a control perspective. Jerk is its own measure and is also possible to affect through torque vectoring.

3.1.1 Torque Gradient

The torque gradient is described as the change in steering wheel torque as the vehicle accelerates in lateral direction. This is a phenomenon called self aligning torque, which works to straighten out the wheels during turning. The reason behind this effect is that the wheel hub of the steering axle is often mounted at a caster angle, which can be seen in Figure 3.1. When the tyre is not travelling straight, the offset between the centre of the tyre and the steering axis will create a steering moment. With a positive caster angle as in the figure, the wheel aligns it self to keep straight.

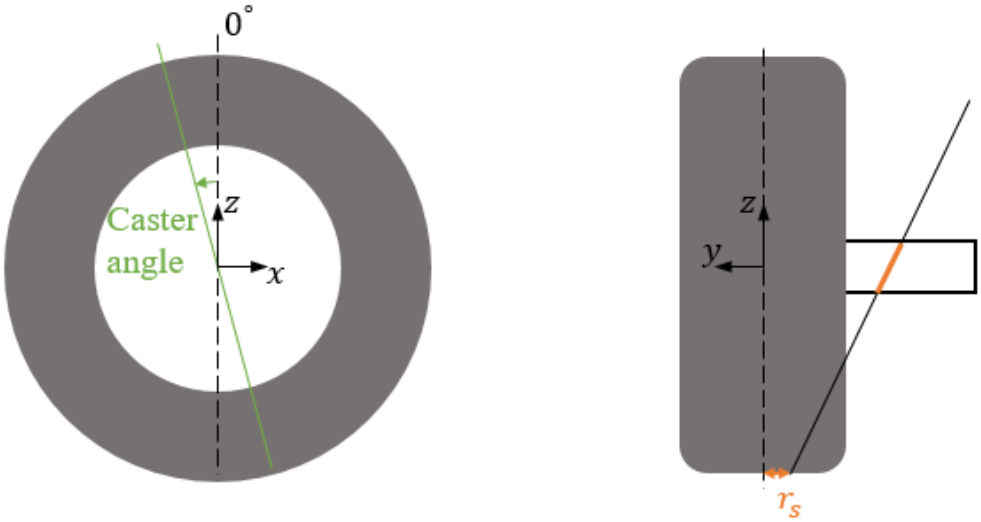

Figure 3.1: Caster angle and scrub radius of a steered wheel.

Another parameter of how the wheel is mounted is the scrub radius, which is also visualised in the image as r_s. Since the scrub radius creates a lateral offset between the centre of the contact patch and the point of rotation, longitudinal forces also create a steering moment. This is where torque vectoring could effect the torque gradient.

3.1.2 Steering Gradient

The steering gradient determines whether the car can be described as oversteered or understeered and is often denoted as K_u (also known as the understeer coefficient). The natural steering gradient can be calculated from vehicle parameters as:

$$K_u = \frac{C_{r\alpha} \cdot L_r - C_{f\alpha} \cdot L_f}{C_{f\alpha} \cdot C_{r\alpha} \cdot L} \tag{3.1}$$

The understeer coefficient affects the steering angle required to achieve a certain turning radius according to the following expression:

$$\delta_f = \frac{L}{R} + \frac{v_x^2}{R} K_u \tag{3.2}$$

This shows that a positive understeer coefficient results in a higher steering angle as the speed increase for a set turning radius. With other words, if K_u is positive, the vehicle is understeered. If the understeer coefficient would instead be negative, then the vehicle would be considered oversteered. This means that an increasing speed would correspond to a decreasing steering angle. This makes the vehicle unstable to control, so it is common to aim for a slightly positive understeer coefficient. If $K_u = 0$, the vehicle becomes neutral steered, which means that the steering angle does not change with speed.

Since torque vectoring produces a yaw moment on the car, it makes it possible to modify the vehicle's yaw rate depending on the driver's steering. This way, it is possible to create an artificial steering gradient.

3.1.3 Jerk

According to ISO 15622:2018 [25], the maximum acceptable jerk for adaptive cruise control for a vehicle is $2.5\,\mathrm{m/s^3}$ above speeds of $20\,\mathrm{m/s}$ and $5\,\mathrm{m/s^3}$ below speeds of $5\,\mathrm{m/s}$. As there is no driver seat function to stabilise the driver laterally, it can be assumed that the limit is similar or lower when controlling lateral jerk. This is supported by [26], noting that lateral jerk is perceived to be worse than both positive and negative longitudinal jerk due to a lack of seat support. In the studies analysed, maximum acceptable lateral jerk is around 60-70% of maximum longitudinal jerk. A conservative limit is therefore $1.5\ \mathrm{m/s^3}$ for lateral jerk.

In [27], unintended jerk is described to be caused by several factors, listed as:

1. Abrupt torque changes, often from initial conditions
2. Gearshifts
3. Mode transitions in hybrid vehicles
4. Road bumps
5. ABS or brake blending manoeuvres

While the proposed powertrain distribution is not a hybrid vehicle in the way that is described, the mode change can be considered similar to point 1 and 3. Point 2 and 4 are largely irrelevant or difficult to stop with a torque vectoring system, and point 5 is more of a byproduct of the torque vectoring itself rather than a problem to solve. The paper further discusses electric powertrains, highlighting that the torque variations in an electric motor are easier to control, but the potentially fast torque variations can cause jerky behaviour. This needs to be kept in mind when designing the controller. The paper notes that a jerk controller must work to reduce the acceleration as little as possible and to not change the average acceleration requested. The difficulty of implementing a jerk controller is to reduce the jerk without increasing the rise time for the requested acceleration, as that would make the vehicle feel less responsive. The problem is that this is a direct antithesis to the control objective itself. A trade-off is required. In a discussion chapter, the article further mentions that the increase of Model Predictive Controllers (MPCs) in the

automotive industry may increase the possibility to handle jerk, as it is able to set constraints on the control optimisation and handle multiple objectives.

A feedforward controller is proposed in [28], using a low pass filter approach on the requested torque to reduce the jerk. In [29], an MPC controller is developed for an acceleration controller, attempting to minimise energy consumption when accelerating but instead using a constraint on the jerk, keeping it below $1\,\mathrm{m/s^3}$. Similarly, [30] uses an approximation of the acceleration derivative to calculate jerk:

$$J = \frac{a_y[i+1] - a_y[i]}{T_s} \tag{3.3}$$

where $a_y[i]$ is the lateral acceleration of time step i and T_s is the sampling time. The article then attempts to use the jerk as a constraint or as a minimisation variable. As this approximation is possible in a state space model, it is a good candidate for control application. In an article analysing lane change control [31], a yaw rate controller is used to calculate the optimal jerk change to provide a comfortable lane change. The lateral acceleration is calculated as a function of yaw rate, body slip angle, steering angle and a steady state speed according to

$$a_y = -\frac{C_{f\alpha} + C_{r\alpha}}{m}\beta + \left(\frac{-L_f \cdot C_{f\alpha} + L_r \cdot C_{r\alpha}}{m \cdot v_x} - v_x\right)\omega_z + \frac{C_{f\alpha}}{m}\delta_f. \tag{3.4}$$

Combining this equation with the previous equation 3.3, it is possible to find jerk as a controlled state.

3.2 Interviews

To determine measurable goals for a predictable steering feel, interviews were done with experienced engineers at Volvo, specialised on handling and steering. The interviews were focused on problems the driver can experience with a power system switching between FWD and AWD at intervals not determined by the driver. A summary of the interviews are presented below.

- The difference in steering compensation when accelerating or braking is not dangerous, but may be annoying to the driver over long periods of time.
- The main concern is the how fast the vehicle switches between cruise mode and startability mode; a sudden change in dynamics may surprise the driver.
- Ideally, the same input should generate the same output whether or not it is currently in FWD, AWD or if the road surface friction is low or high.
- If possible, a reduction of steering compensation when accelerating or braking is beneficial.

3.3 Predictability in Emergency Manoeuvres

In Sweden, there are around 60 000 crashes with wild animals every year [32]. Around 5000 of those are with elks, which can cause bodily injuries or even death.

While the risk of bodily injuries is lower when driving a heavy vehicle, the accident rate will be similar and the vehicle may be damaged.

A common scenario that can contribute to such incidents is cornering with forest blocking the sight around the corner. In this situation, an animal might be hidden in the forest, out of sight from the driver, causing an emergency brake situation as it runs up on the road. In such a situation, it is very difficult to remain in control of the vehicle. The fully applied brakes and curving of the road will cause the tyres to reach their limits, risking the vehicle to start drifting or jackknifing. To analyse such a scenario, a simulated test was done, which is visualised in the graphs in Figure 3.2. Here, the result from doing the test with two different braking strategies are shown. The first strategy is with a forced equal left/right torque split where both wheels are limited if one loses traction (in turquoise), and the second with individually controlled brakes and no yaw moment control (in green). For the latter case, this means that only a longitudinal force is regarded. How this is distributed between the four electric machines, however, is not constrained. The test was done through a left hand curve, starting at 80 km/h, and emergency braking starting at 20 s.

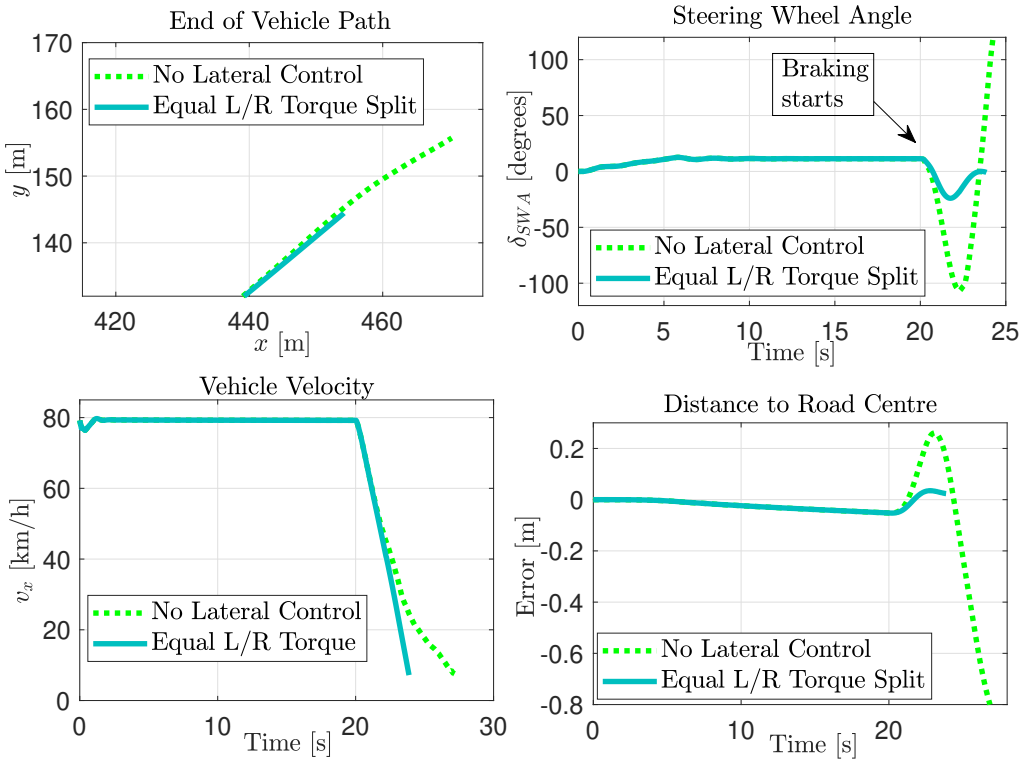

Figure 3.2: Emergency braking through corner, with an initial speed of 80 km/h. The braking starts at 20 s.

From the figure, it can be seen that a vehicle with individually optimised motors for each tyre creates too much freedom in the lateral direction. As the driver brakes and the friction limit is reached on the inner tyres, the yaw rate of the vehicle is affected. The driver then loses control of the vehicle due to an added yaw rotation,

which significantly affects the stopping distance. With a fixed split, the vehicle is able to come to a safe stop, but not without noticeable steering compensation from the driver. The distance from the road's centre is also shown, indicating that not controlling the lateral dynamics cause the driver to loose control of the vehicle and end up almost a metre away from the centre.

Since fine motor skills decrease significantly in high stress situations [33], it is to be expected that a driver will perform worse when presented with an emergency situation, compared to normal driving [34]. Ideally, there should be no expectation on the driver to know how to handle the emergency braking situation. Taking the vehicle to a safe stop should be as simple as pressing the brake and calmly reducing the steering angle.

One common way to improve stability in emergency manoeuvres is to use a yaw rate controller [35], [36]. As the proposed vehicle has four motors, torque vectoring would allow for very precise control of the yaw rate, which makes it a good candidate as a control policy.

In an ideal case the vehicle should follow the steady state yaw rate at all times. This would result in a minimal steering wheel angle compensation from the driver. As the vehicle brakes, the requested steering angle would decrease almost linearly, as seen in Figure 3.3.

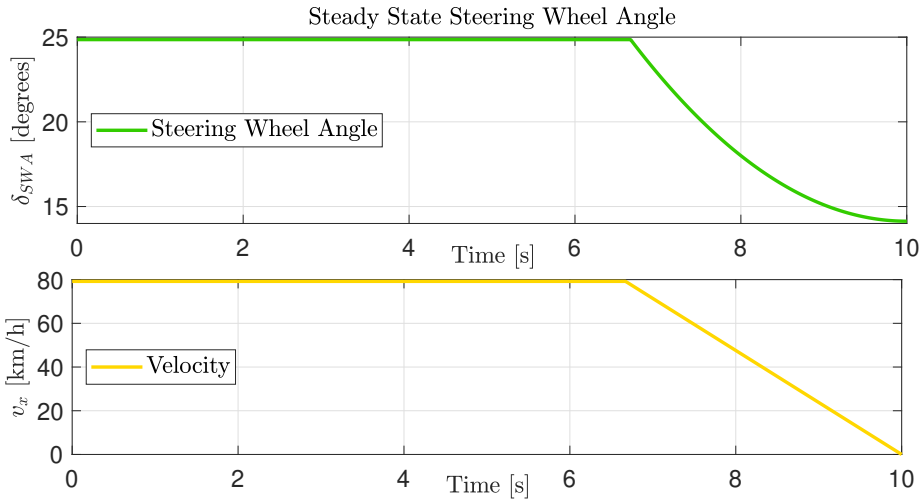

Figure 3.3: Steering angle over time for a vehicle that always follow the steady state curvature while emergency braking during cornering.

This behaviour is desirable as it makes the handling more predictable. The steady state yaw rate is found through the equation

$$\omega_{z,ref} = \frac{v_x \cdot \delta_f}{L_f + L_r + m \cdot K_u \cdot v_x^2} \tag{3.5}$$

3.4 Sudden Switch between Cruise and Power mode

The vehicle used in this thesis it designed to have two different modes of driving. The first one is called cruise mode and the second one is called power or startability mode. The difference is that cruise mode only utilise the front axle for propulsion, while the power mode utilise all wheels for propulsion. This will result in a difference in handling depending on which mode the vehicle is in. In normal circumstances, the cruise mode will be used most of the time and power mode only used when higher longitudinal acceleration is needed. This begs the question, 'How will the vehicle behave if a switch between modes would suddenly occur during cornering?'. This section analyses the effect of a sudden mode change by simulating this situation.

3.4.1 Steady-state cornering

To analyse the impact of switching modes in the middle of a curve, a mode switch was forced during a steady state corner. This test was done at 10 m/s, a constant steering wheel angle of 100° and friction coefficient $\mu = 0.3$ corresponding to driving on packed snow. This resulted in a lateral acceleration around 1.95 m/s^2. The resulting yaw rate can be seen in figure 3.4. It can be seen that the two individual modes, cruise and power, have only slightly different properties in steady state. When using power mode, the vehicle behaves as more oversteered compared to the cruise mode. An interesting observation is that after the switch has taken place, the vehicle simply transitions from one curve to the other. In both directions, the switch results in a smooth handling transition which was completed in around 0.5 s. In this scenario the difference in yaw rate was minimal between the two modes and is deemed to not affect the driver noticeably.

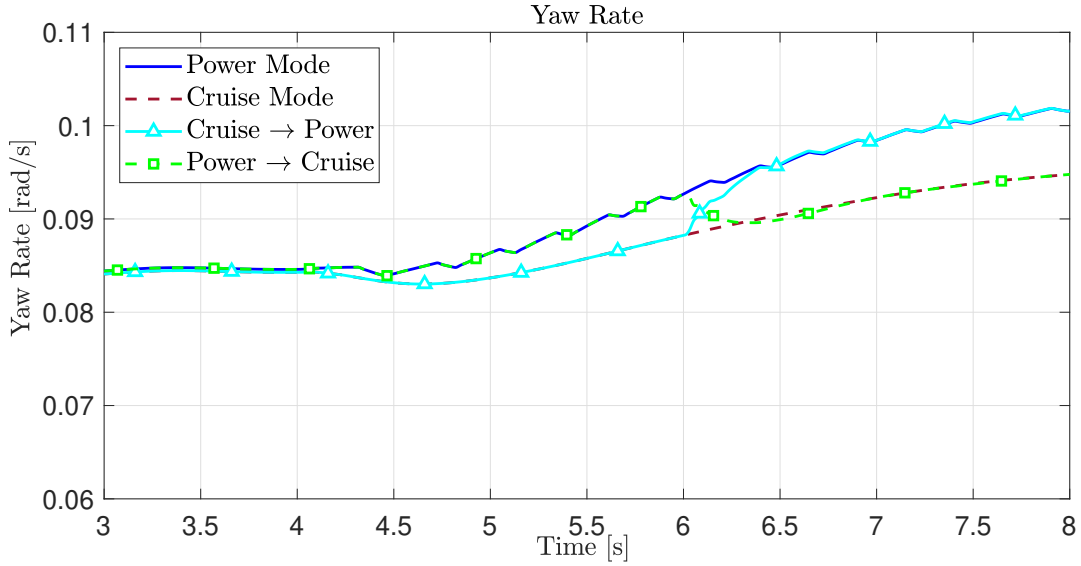

Figure 3.4: Yaw rate over time for mode switching (at t = 6 s) during a steady state corner. Note that the time starts at t = 3s, as this was when steady state was first achieved.

3.4.2 Acceleration during cornering

As the previous test did not hint towards in a considerable difference in handling during switching, a more extreme test was done. In this test, the mode switching took place during acceleration as this would increase the difference in handling properties between the two modes. The test was done with a base speed of 80 km/h, a steering wheel angle of 40° and friction coefficient $\mu = 0.8$ corresponding to driving on dry asphalt. After 3 s, an acceleration of 1.5 m/s^2 is introduced and the mode switching takes place at $t = 4$ s. The resulting yaw rate can be seen in figure 3.5 which shows a similar behaviour to the steady state case. It can be seen that the two modes have distinct curves and the switching simply creates a transition between them. This time, however, the difference in the two curves is considerably larger and the transition is more sudden. This abrupt change in dynamics may affect the driver as the vehicle suddenly becomes less understeered when the power mode is activated. This will result in the vehicle turning inwards in the curve which the driver has to compensate for.

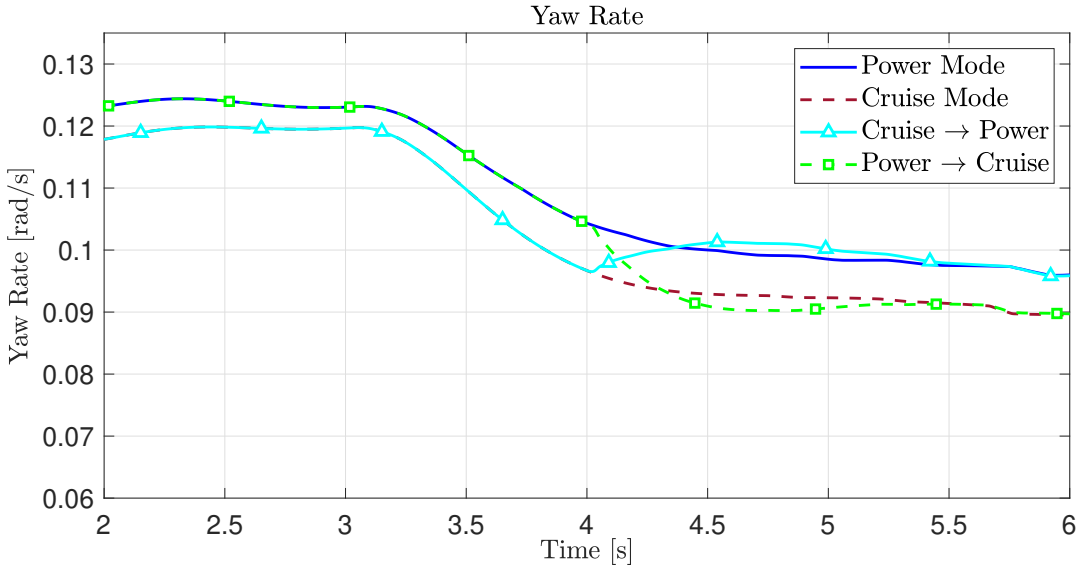

Figure 3.5: Yaw rate over time for mode switching (at t = 4 s) during acceleration while cornering.

To analyse a simulated driver's response to the switch during acceleration, a driver model was used instead of constant steering angle. Except for the steering angle, all test parameters are the same as the previous test for accelerating through a curve. The steering angle controlled by the driver model is plotted in figure 3.6. Although the graph shows a more oscillatory behaviour than previous cases, the general trend of two distinct curves and a transition between them during mode switching still holds true. Due to the mode switch occurring at 10 s, the driver has to compensate by increasing/decreasing the steer angle. In figure 3.7, corresponding yaw rate for the test including driver model is presented. This shows that the driver manages to keep a consistent yaw rate for both cruise and power mode. When introducing the

mode switch, however, the truck behaves in an unexpected manner and the driver ends up deviating from the road centre.

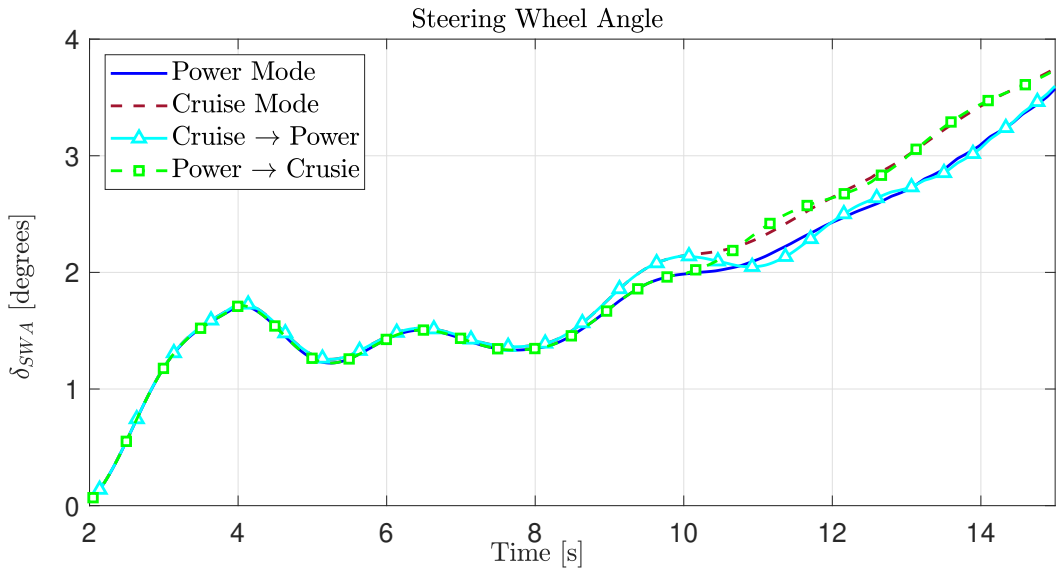

Figure 3.6: Steering angle over time for mode switching (at t = 10 s) during acceleration while cornering with a simulated driver.

Figure 3.7: Yaw rate over time for mode switching (at t = 10 s) during acceleration while cornering with a simulated driver.

4

Control System

This chapter presents the implementation and construction of the control system. All the development and testing have been done in Matlab and Simulink, and the Simulink model used in the thesis is a combination of estimation, control and VTM models provided by Volvo. For motion control, there are two controllers working in coordination, named motion coordinator and control allocator. The motion coordinator converts the reference from the driver interpreter, such as acceleration and reference yaw rate, to vehicle level force requests, such as yaw moment, lateral force, or longitudinal force. The low level control allocator (CA) then converts the vehicle forces to specific actuator torques. The entire system architecture is presented in Figure 4.1. Here, the Volvo provided models are shown as black boxes, controllers as yellow boxes, estimation as blue boxes and the driver interpreter as a green box.

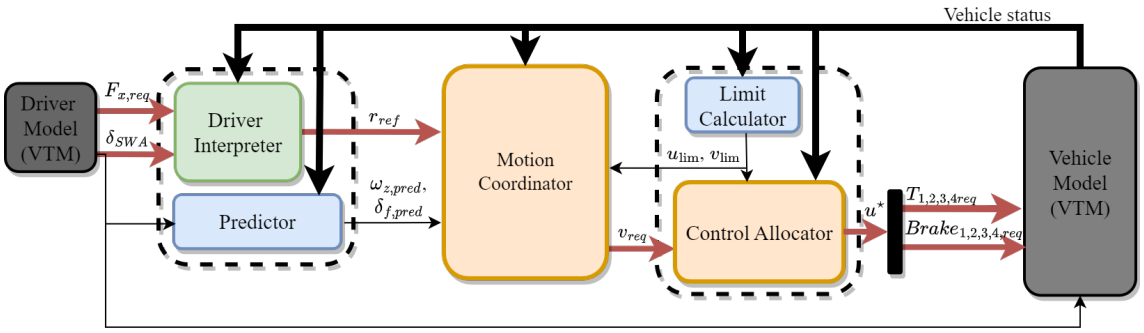

Figure 4.1: The basic system architecture as it would work in the vehicle. The limit calculator is considered to be part of the control allocator, but separated for clarity. Similarly, the predictor is considered to be part of the driver interpreter, but explicitly shown in the figure to clarify the flow of information.

r_{ref} is the reference points for the vehicle states, see eq 4.34. v_{req} is the output from the controller, see eq 4.33.

4.1 Driver Model and Vehicle Model

The plant model is regarded as the vehicle together with its driver and they were both provided by Volvo. The vehicle model includes the mechanical dynamics of a truck, its axles and tyres. Inputs to the vehicle model are steering angle and actuator torques. However, the VTM does not model powertrain dynamics, which instead has been separately implemented as seen in [37]. This way, the model also takes

actuator limits and delays into account. The VTM model outputs vehicle status (such as velocities and forces), which are recorded for analysis of the result.

The driver model is used to follow a created path, outputting a steering wheel angle and a longitudinal force request. This differs from a real world driver, since the pedal position has already been converted to a longitudinal force.

4.2 Driver Interpreter and Predictor

A driver interpreter has been created to convert the steering wheel angle to a lateral performance request. This is done by first converting the steering wheel angle to steering angle δ_f by dividing with the steering ratio. The steering angle is then used to create a yaw rate reference, based on the steady state yaw rate for the current speed, as presented in equation 3.5. In the longitudinal direction, the longitudinal force from the driver model is used directly. These references are the goals for the motion coordinator to achieve. The predictor block expands the driver interpretation by estimating future inputs that can be used, as later explained in subsection 4.4.6.

4.3 Control Allocator and Limit Calculator

Controlling the movement of a vehicle with motors for each individual wheel is an over actuated task. To optimise the distribution of torque between all actuators, a control allocator was used. The control allocator takes in the global request v_{req} from the motion controller and then calculates the optimal actuator combination to minimise power loss, as seen in [21]. The goal was to follow the motion request, while minimising power loss, which can be reached by solving the following minimisation problem:

$$\begin{aligned} \mathbf{u}^* &= \min_{\mathbf{u}} P_{loss}(\mathbf{u}, \omega_i) \\ \text{s.t.} \quad & B \cdot \mathbf{u} = \mathbf{v}_{req} \end{aligned} \tag{4.1}$$

where u^* is the optimal input to the actuators. The input vector $\mathbf{u} \in \mathcal{R}^8$ is comprised of the four service brakes followed by the two cruise motors and the two startability motors.

The motor mapping $P_{loss}(\mathbf{u}, \omega)$ takes in a motor speed and torque and then returns the motor's power loss. The control allocator uses the data constructed in section 2.6.2, where it can be seen that the data have a quadratic form. With the acquired wheel speed, a second degree polynomial was fit to the torque and power loss values to create a quadratic function that worked with the minimisation problem:

$$P_{loss} = T_i^2 \cdot c_2 + T_i \cdot c_1 + c_0 \tag{4.2}$$

where T_i is wheel torque and the coefficients c_2 and c_1 change depending on wheel speed and motor type.

The problem is then formulated as a minimisation problem according to

$$\mathbf{u}^* = \min_u \frac{1}{2}\mathbf{u}^T H \mathbf{u} + g^T \mathbf{u} \tag{4.3}$$

The second degree coefficient (c_2) is used for the H function and the first degree coefficient (c_1) is used for the g function. Using the two different types of motors available and the brakes, the final weight matrices are

$$H = 2\begin{bmatrix} c_{2,brk} & 0 & 0 \\ 0 & c_{2,crs} & 0 \\ 0 & 0 & c_{2,stb} \end{bmatrix} \tag{4.4a}$$

$$g^\top = \begin{bmatrix} -|\omega_i| & c_{1,crs} & c_{1,stb} \end{bmatrix} \tag{4.4b}$$

where ω_i is the rotational speed for tyre i.

Additionally, constraints had to be put on the allocator to ensure that the motors operated within their operating limits and responded to the driver's requests. This is done by introducing an inequality constraint, with an upper limit u_{max} and a lower limit u_{min} on the torque outputs. These limits are calculated through the limit calculator and can be summarised as:

1. Max F_x per tyre, see equation 2.9
2. Actuator limits see equation 2.49
3. Actuator rate of change limits, see equation 2.52

Negative limits, such as the maximum negative torque, has to be multiplied with -1 to fit the inequality criteria. With these limits in place, the final set of equations become

$$\begin{aligned} \mathbf{u}^* = \min_u \quad & \frac{1}{2}\mathbf{u}^\top H \mathbf{u} + g^\top \mathbf{u} \\ \text{s.t.} \quad & B \cdot \mathbf{u} = \mathbf{v}_{req} \\ & \mathbf{u}_{min} \leq \mathbf{u} \leq \mathbf{u}_{max} \end{aligned} \tag{4.5}$$

where $\mathbf{u}_{min}$ and $\mathbf{u}_{max}$ are the limits set by the limit calculator, used by both the control allocator and the motion coordinator. $\mathbf{v}_{req}$ in this case is the requested global force output from the motion coordinator. Depending on the controller, this could simply be a longitudinal force request F_x or multiple requests up to $\{F_x,\, M_z,\, F_y\}$. It is important to understand that the solver will fail if the requests cannot be met by the actuators. The solver will then try to break the actuator limits to meet the requests, and cause other problems. Because of this, actuator limits had to be accounted for in the motion coordinator so that the value for $\mathbf{v}_{req}$ was feasible.

The B matrix models how the wheel torque affects the performance constraint $\mathbf{v}_{req}$. For F_x and M_z, it needs to be converted from motor torque to force and moment:

$$B_{power} = \begin{bmatrix} \frac{1}{r_w} & \frac{1}{r_w} & \frac{1}{r_w} & \frac{1}{r_w} & \frac{gr_{crs}}{r_w} & \frac{gr_{crs}}{r_w} & \frac{gr_{stb}}{r_w} & \frac{gr_{stb}}{r_w} \\ -\frac{t_f}{2\,r_w} & \frac{t_f}{2\,r_w} & -\frac{t_r}{2\,r_w} & \frac{t_r}{2\,r_w} & -\frac{gr_{crs}\cdot t_f}{2\,r_w} & \frac{gr_{crs}\cdot t_f}{2\,r_w} & -\frac{gr_{stb}\cdot t_r}{2\,r_w} & \frac{gr_{stb}\cdot t_r}{2\,r_w} \end{bmatrix} \tag{4.6}$$

where r_w is the wheel radius; gr_{crs} and gr_{stb} are the respective gear ratios; and t_f and t_r are track width front and rear.

4.3.1 Accounting for Static Losses in the Electrical Motors

When formulating the QP problem, the constant term c_0 is not accounted for, as the cost is not affected by the torque. In reality, the startability motor can be disconnected by a clutch to eliminate any idle losses. This means that startability motors will suffer no losses while not used, while the cruise motors always need to account for static losses. The QP solver used in this thesis, originally did not utilise that such a disconnection could be made. However, this was solved by using two independent QP solvers at the same time. One for power mode, with all 4 motors available as previously presented, and one for cruise mode, with the two startability motors disabled, which would result in the following B-matrix:

$$B_{cruise} = \begin{bmatrix} \frac{1}{r_w} & \frac{1}{r_w} & \frac{1}{r_w} & \frac{1}{r_w} & \frac{gr_{crs}}{r_w} & \frac{gr_{crs}}{r_w} & 0 & 0 \\ -\frac{t_f}{2\,r_w} & \frac{t_f}{2\,r_w} & -\frac{t_r}{2\,r_w} & \frac{t_r}{2\,r_w} & -\frac{gr_{crs}\,t_f}{2\,r_w} & \frac{gr_{crs}\,t_f}{2\,r_w} & 0 & 0 \end{bmatrix} \tag{4.7}$$

where subscript *cruise* indicates that the vehicle is in cruise mode (the startability axle is disengaged). The total power loss for the power mode can then be calculated as

$$P_{loss,power} = \frac{1}{2}\mathbf{u}_{power}^{\top} H \mathbf{u}_{power} + g^{\top}\mathbf{u}_{power} + c_{crs} + c_{stb} \tag{4.8a}$$

where subscript *power* indicates that the vehicle is in power mode (both axles engaged). For cruise mode, the equation looks like the following:

$$P_{loss,cruise} = \frac{1}{2}\mathbf{u}_{cruise}^{\top}\, H\, \mathbf{u}_{cruise} + g^{\top}\mathbf{u}_{cruise} + c_{crs} \tag{4.8b}$$

As long as both solvers are feasible, the mode with lower power losses is considered optimal. Pseudo code for this may look like algorithm 1 below, where $cruise_{flag}$ is an integer that is 1 if the QP problem is feasible, and 0 or -2 otherwise.

Algorithm 1 Find Optimal Power Loss

```
if cruise_flag == 1 and P_loss,cruise ≤ P_loss,power then
    u = u_Ploss,cruise
else
    u = u_Ploss,power
end if
```

As the QP problem for power mode will always be feasible if the original problem is designed properly, it is not checked for.

4.4 Motion Coordinator

The motion coordinator has two objectives. One is to construct an optimal force requests in the form of a vector $\mathbf{v}_{req}$ that is sent to the control allocator and the other is to ensure that the request itself is feasible. This can be done by either constructing the control action beforehand and then saturate it, or by using a controller that is able to handle constraints as part of the control calculation. In this section, controllers that was tested in this thesis are presented. The different controller styles are later compared and tested, as can be seen in chapter 5.

4.4.1 PID

PID is short for Proportional-Integral-Derivative, which describes the controller function. It is a very simple controller and useful for controlling a single input single output (SISO) system. As yaw rate control is a single state system, PID is a common solution. Weights are put on each part of the controller, and are then summarised to a penalty, which is the control action:

$$u_{PID}(t) = K_p e(t) + K_i \int_0^t e(t)dt + K_d \frac{de(t)}{dt} \tag{4.9}$$

where $e(t)$ is the error at time t, $u_{PID}(t)$ is the output control action, and K_p, K_i and K_d are weights that are often set from a table based on testing.
A big downside with using a PID controller is that it is almost blind to the world. It is only aware of the current and previous states, and optimises from there. One way to implement a model with a PID is to have the weights change with physical properties, such as side slip angle or velocity [38]. In this thesis, PID was used to compare with the more complex controllers to see if they provide any advantages over the more traditional controller.

4.4.2 LQR/LQI

LQR stands for Linear-Quadratic-Regulator and, unlike the PID controller, is model based. This means that it will take into account the dynamics of the vehicle when calculating the next control output. LQR is also a multiple input multiple output (MIMO) controller, which means that it is able to minimise multiple states at once and weigh the positives of minimising one state versus the cost of increasing another. An LQR controller's goal is to minimise the cost function

$$J = \sum_{k=0}^{\infty} x[k]^\top Q x[k] + u[k]^\top R u[k] \tag{4.10}$$

where $x[k+1] = Ax[k] + Bu_{LQR}[k]$. The solution to this is

$$u_{LQR}[k] = -K\, x[k] \tag{4.11}$$

where K is the control gain, calculated offline through the Matlab function `dlqr`, which solves the discrete-time Ricatti equation:

$$S = A^T SA - A^T SB(B^T SB + R)^{-1} B^T SA + Q \tag{4.12}$$

$$K = (B^T SB + R)^{-1} B^T SA \tag{4.13}$$

As the name suggests, LQR is a linear controller and hence needs a completely linear model. This can be difficult to obtain when the real system is highly nonlinear, which can often be seen in vehicle models. Because of this, many assumptions need to be made on the vehicles states. The model used in this thesis is a 3 state model using the equations for body slip angle and yaw rate shown in chapter 2.3, with an integral state added for yaw rate to avoid an offset error:

$$A = \begin{bmatrix} \frac{-L_r^2 C_{r\alpha} - L_f^2 C_{f\alpha}}{I_{zz} v_x} & \frac{L_r C_{r\alpha} - L_f C_{f\alpha}}{I_{zz}} & 0 \\ \frac{L_r C_{r\alpha} - L_f C_{f\alpha}}{v_x^2 m} - 1 & \frac{-C_{f\alpha} - C_{r\alpha}}{v_x m} & 0 \\ 1 & 0 & 0 \end{bmatrix} \quad (4.14a) \qquad x = \begin{bmatrix} \omega \\ \beta \\ \omega_I \end{bmatrix} \quad (4.14b)$$

$$B = \begin{bmatrix} \frac{1}{I_{zz}} \\ 0 \\ 0 \end{bmatrix} \quad (4.14c) \qquad u_{LQR} = M_z \quad (4.14d)$$

where ω_I is the integral state of yaw rate, and u is the current yaw moment created from the actuators. The LQR output is a requested yaw moment which is sent to the control allocator to achieve the reference yaw rate. The next control action at any time step k is found by replacing the states in equation 4.11 with the current state error $e[k] = x[k] - r_{ref}[k]$. Note that this controller does not calculate longitudinal forces. Hence, a separate cruise controller was needed, which the previously explained PID controller was a good candidate for.

The model works well for steady state cornering, but there are some things to consider. For a normal LQR, the optimal controller gain $\mathbf{K}$ is calculated offline. This means that the vehicle model is never updated, which does not properly reflect reality. The vehicle model does in fact change based on vehicle speed, which is clear from the existence of v_x in the A-matrix (seen in equation 4.14b). A solution to this is including v_x as a state that is updated together with all other states. This results in a nonlinear relation between the velocity and yaw rate and is difficult to calculate.

4.4.3 LQR - LPV

To solve the problem with an offline calculated LQR model, it is possible to use an LPV model, which stands for Linear-Parameter-Varying. This extended version of an LQR updates the state space model every loop. It should however be noted that the Matlab commands `lqr`, `dlqr` and `ss` are not supported by code generation. Attempting to solve the Riccatti equation through `idare` is also not supported. Another approach to solve this online approach is to directly observe the Ricatti equation.

The offline Riccatti equation can be solved through

$$A^\top XA - X - (A^\top XB)(B^\top XB + R)^{-1}(B^\top XA) + Q = 0 \quad (4.15)$$

where the matrices A, B and R are as presented in the previous section about LQR. An approximation of the change in X can then be found by looking at the error in

this equation in an online computation:

$$A^\top X[k]A - (A^\top X[k]B)(B^\top X[k]B + R)^{-1}(B^\top X[k]A) + Q = X[k+1] \tag{4.16}$$

This is not exact, and should be thought of more as a proportional controller of X. Over time it will converge to the correct X. The updated gain can be found through:

$$K[k+1] = (R + B^\top X[k+1]B)^{-1}(B^\top X[k+1]A) \tag{4.17}$$

With this, it is possible to update parameters in the model, such as the velocity, or to have dynamic weighting. In this case, dynamic weighting is important as steering action from the driver can become much more aggressive at lower speeds. The control penalty matrix $\mathbf{R}$ is set based on the current velocity:

$$\mathbf{R} = \frac{100}{v_x^2} \tag{4.18}$$

reducing the aggressiveness from the controller as the speed approaches zero.

4.4.4 MPC

MPC stands for Model-Predictive-Controller and is a controller that uses a predetermined time horizon and propagates simulated inputs forward in time to find an optimal controller output. This is done through a state space model, similar to the LQR controller presented previously. The model is expanded over the entire horizon and concatenated into one quadratic minimisation problem which is then minimised. The MPC controller can take both nonlinear models and constraints, for example states or outputs, into account while calculating the optimal control action. This ensures that deviations from the path, or maximum torque output from the actuators are also part of the optimisation. With this, the MPC is able to plan ahead to avoid saturation of actuator output, where the other controllers would lose control over the model. The input to the MPC is the refecence states that the vehicle should track, and the output is the global force requests that are being sent to the control allocator. Note that the MPC optimises a sequence of control actions $u = \{u[0], u[1], ..., u[T_{horizon}]\}$ for a given time horizon, but the output to the control allocator is only the first step $u[0]$. This makes the MPC very computationally complex, since only a part of the calculated solution is actually used. Given the complexity of calculating quadratic minimisation problems with matrices with hundreds of rows and columns every time iteration, MPC is a very computationally heavy controller.

4.4.4.1 MPC Model

The model used in this thesis was based on an article published in 2020 [39]. The model is a two state LPV model that uses the steering angle as disturbances. For this thesis, the model has been expanded to allow longitudinal force reference points through additional longitudinal acceleration and velocity states. The expanded

state-space model looks like the following:

$$\dot{x} = Ax + Bu_{mpc} + C\delta_f + D \tag{4.19a}$$

$$x = \begin{bmatrix} \dot{v_x} \\ v_x \\ \omega_z \\ \beta \end{bmatrix} \tag{4.19b}$$

$$u_{mpc} = \begin{bmatrix} T_{fl} \\ T_{fr} \\ T_{rl} \\ T_{rr} \end{bmatrix} \tag{4.19c}$$

where v_x is the longitudinal velocity, ω_z is yaw rate and β is the body slip angle. Note that this does not follow a standard state space structure. The C and D matrices are not affected by the states, nor the controller input at all. The yaw rate and the body slip angle are calculated using a single-track model. The derived equations are expressed in chapter 2.3, but repeated here for clarity:

$$\dot{\beta} = -\frac{C_{f\alpha} + C_{r\alpha}}{m \cdot v_x}\beta + \left(\frac{-L_f \cdot C_{f\alpha} + L_r \cdot C_{r\alpha}}{m \cdot v_x^2} - 1\right)\omega_z + \frac{C_{f\alpha}}{mv_x}\delta_f \tag{4.20a}$$

$$\dot{\omega_z} = -\frac{L_f \cdot C_{f\alpha} - L_r \cdot C_{r\alpha}}{I_{zz}}\beta - \frac{L_f^2 \cdot C_{f\alpha} - L_r^2 \cdot C_{r\alpha}}{I_{zz} \cdot v_x}\omega_z + \frac{L_f \cdot C_{f\alpha}}{I_{zz}}\delta_f \tag{4.20b}$$

The velocity state derivative is derived from

$$\dot{v_x} = \omega_z v_y + \frac{T_{fl}}{r_w \cdot m} + \frac{T_{fr}}{r_w \cdot m} + \frac{T_{rl}}{r_w \cdot m} + \frac{T_{rr}}{r_w \cdot m}. \tag{4.21}$$

This leads to the following continuous A-matrix:

$$A_c = \begin{bmatrix} 0 & 0 & v_y & 0 \\ 0 & 0 & \frac{-L_r^2 C_{r\alpha} - L_f^2 C_{f\alpha}}{I_{zz} v_x} & \frac{L_r C_{r\alpha} - L_f C_{\alpha f}}{I_{zz}} \\ 0 & 0 & \frac{L_r C_{r\alpha} - L_f C_{f\alpha}}{v_x^2 m} - 1 & \frac{-C_{f\alpha} - C_{r\alpha}}{v_x m} \end{bmatrix} \tag{4.22}$$

While the change in velocity and yaw rate is easy to measure, calculating how the acceleration changes over time, for the purpose of simulating a horizon, is difficult. Because of this, the derivatives themselves are approximated using Newton's method. Assuming the model has already been discretised, $x[k+1] = \mathcal{F}_d x[k]$, the current rate of change can be calculated. As an example for velocity:

$$a_x = \frac{f(x+h) - f(x)}{h} = \frac{v_x[k+1] - v_x[k]}{T_{s,MPC}} = \frac{(\mathcal{F}_d - 1)v_x}{T_{s,MPC}} \tag{4.23}$$

where $T_{s,MPC}$ is the sampling time of the MPC controller. This naturally follows the state space model structure. The step time $T_{s,MPC}$ has to be used, as the difference between x[k] and x[k+1] needs to be converted to the continuous time derivative.

This row is already discretised, and needs to be added post discretisation. The discretised matrix A_d is calculated as

$$A_d = \begin{bmatrix} 0 & 1 & 0 & 0 \\ 0 & 0 & 1 & 0 \\ 0 & 0 & 0 & 1 \end{bmatrix} + A_c \cdot T_{s,MPC} \tag{4.24}$$

From this, the final discrete A-matrix can be expressed with the added state derivative as:

$$A = \begin{bmatrix} 0 & \frac{-1}{T_{s,MPC}} & \frac{v_y}{T_{s,MPC}} & 0 \\ \multicolumn{4}{c}{\text{- - - - - - - - - - - - - - - -}} \\ \multicolumn{4}{c}{A_d} \end{bmatrix} \tag{4.25a}$$

The B,C and D matrices are also discretised and expressed as below:

$$B = \begin{bmatrix} \frac{1}{T_{s,MPC}\, r_w m} & \frac{1}{T_{s,MPC}\, r_w m} & \frac{1}{T_{s,MPC}\, r_w m} & \frac{1}{T_{s,MPC}\, r_w m} \\ \frac{1}{r_w m} & \frac{1}{r_w m} & \frac{1}{r_w m} & \frac{1}{r_w m} \\ -\frac{t_f}{2\, I_{zz}\, r_w} & \frac{t_f}{2\, I_{zz}\, r_w} & -\frac{t_r}{2\, I_{zz}\, r_w} & \frac{t_r}{2\, I_{zz}\, r_w} \\ 0 & 0 & 0 & 0 \end{bmatrix} \tag{4.25b}$$

$$C = \begin{bmatrix} 0 \\ 0 \\ \frac{C_{f\alpha}\, L_f}{I_{zz}} \\ \frac{C_{f\alpha}}{v_x m} \end{bmatrix} \tag{4.25c}$$

$$D = \begin{bmatrix} -\frac{1}{T_{s,MPC}\, m} \left(\frac{1}{2} \rho \cdot C_d \cdot A_f \cdot v_x^2 - C_r \cdot F_z \right) \\ -\frac{1}{m} \left(\frac{1}{2} \rho \cdot C_d \cdot A_f \cdot v_x^2 - C_r \cdot F_z \right) \\ 0 \\ 0 \end{bmatrix} \tag{4.25d}$$

4.4.4.2 QP Formulation

The matrices are fed into a receding horizon controller formulated as a quadratic minimisation problem:

$$\begin{aligned} \min_{z} \quad & \frac{1}{2} \mathbf{z}^\top H_{mpc} \mathbf{z} + g_{mpc}^\top \mathbf{z} \\ \text{s.t.} \quad & A_{eq} \cdot \mathbf{z} = b_{eq} \\ & A_{in} \cdot \mathbf{z} \leq b_{in} \end{aligned} \tag{4.26}$$

where H_{mpc} and g_{mpc} are the weighting matrices for the controller; A_{eq} and b_{eq} are equality constraints, representing the state space model and ensures that the

model follows the state space structure; and A_{in} and b_{in} represent the inequality constraints, such as the friction circle and the actuator limits. $\mathbf{z}$ represents the set of states from $t = 1$ to $t = N$ followed by the set of optimal control actions from $t = 0$ to $t = N - 1$ where N is the prediction horizon in samples. This is visualised as

$$\mathbf{z} = \begin{bmatrix} x[1] \\ x[2] \\ \vdots \\ x[N] \\ u_{mpc}[0] \\ u_{mpc}[1] \\ \vdots \\ u_{mpc}[N-1] \end{bmatrix} \tag{4.27}$$

where the solution $u^*_{mpc}[0]$ is extracted from the optimised vector $\mathbf{z}^*$ that is acquired from eq 4.26.

The inequality constrains used are a combination of limits on the control action and limits on the states. The control action limits are the same limits as used in the control allocator and are taken from the limit calculator. The state limits are constant values, used to avoid rollover and limit state error. The constraints are summarised as the following (note that item 1, 2 and 4 are the same as in the control allocator):

1. Max F_x per tyre, see equation 2.9
2. Actuator limits see equation 2.49
3. Rollover lateral acceleration limit, see equation 2.33
4. Actuator rate of change limits, see equation 2.52
5. State limits, such as maximum yaw rate error

The inequality matrices grow quite large, as the constraint has to be ensured at every time step. The full inequality matrices can be found in appendix A.

As MPC only uses quadratic minimisation, g_{mpc} is zero. H_{mpc} is a diagonal matrix with the state and control output weights for the different time instances from 0 to N. Using $\mathbf{Q}$ for state weight and $\mathbf{R}$ for control weight, $\mathbf{Q}$ punishes the error of the states relative to the reference point(see chapter 4.4.5) and $\mathbf{R}$ is set as an identity matrix. $\mathbf{R}$ can not be set as zero, as the MPC would attempt to solve all errors in a single timestep, which would make the vehicle feel very erratic and nervous:

$$Q = \begin{bmatrix} cost_{e_{a_x}} & 0 & \cdots & 0 \\ 0 & cost_{e_{v_x}} & & \vdots \\ \vdots & & cost_{e_{\omega_z}} & \vdots \\ 0 & \cdots & \cdots & cost_{e_\beta} \end{bmatrix} \tag{4.28}$$

$$R = \begin{bmatrix} cost_{T_{fl}} & 0 & \cdots & 0 \\ 0 & cost_{T_{fr}} & & \vdots \\ \vdots & & cost_{T_{rl}} & \vdots \\ 0 & \cdots & \cdots & cost_{T_{rr}} \end{bmatrix} \tag{4.29}$$

In this case, the weight is the same throughout the entire horizon, which means the weights are simply repeated for each horizon step.

$$H_{Q,mpc} = \begin{bmatrix} Q & 0 & \cdots & 0 \\ 0 & Q & & \vdots \\ \vdots & & \ddots & \vdots \\ 0 & \cdots & \cdots & Q \end{bmatrix} \quad (4.30a) \qquad H_{R,mpc} = \begin{bmatrix} R & 0 & \cdots & 0 \\ 0 & R & & \vdots \\ \vdots & & \ddots & \vdots \\ 0 & \cdots & \cdots & R \end{bmatrix} \quad (4.30b)$$

$$H_{mpc} = 2 \begin{bmatrix} H_{Q,mpc} & 0 \\ 0 & H_{R,mpc} \end{bmatrix} \quad (4.30c)$$

In the context of an MPC, A_{eq} and b_{eq} represents the state space model, ensuring that the input $\mathbf{z}$ follows the laws set by the model. The evolution of the states in A_{eq} and b_{eq} follow the standard state space structure:

$$-Ax[k] + x[k+1] - Bu_{mpc}[k] = 0 \quad (4.31)$$

Assuming no disturbance in the model and a setpoint at zero, A_{eq} and b_{eq} is a set of matrices describing this equation for each time step across the horizon.

$$A_{eq}\mathbf{z} = b_{eq} = \left[\begin{array}{ccccc|cccc} I & 0 & \cdots & & 0 & -B & 0 & \cdots & 0 \\ -A & I & 0 & \cdots & 0 & 0 & -B & \cdots & 0 \\ 0 & -A & I & \cdots & 0 & \vdots & & \ddots & \vdots \\ \vdots & & \ddots & \ddots & \vdots & & & & \\ 0 & & \cdots & -A & I & 0 & \cdots & & -B \end{array}\right] \begin{bmatrix} x[1] \\ x[2] \\ \vdots \\ x[N] \\ u_{mpc}[0] \\ u_{mpc}[1] \\ \vdots \\ u_{mpc}[N-1] \end{bmatrix} = \begin{bmatrix} Ax[0] \\ 0 \\ \vdots \\ \vdots \\ \vdots \\ \vdots \\ 0 \end{bmatrix} \quad (4.32)$$

Note that the output from this QP formulation is a set of torques for the four wheels. However, the MPC should output a longitudinal force request and a yaw moment request for the truck. Hence the torques need to be converted into global forces in the following way:

$$v_{req} = \begin{bmatrix} F_{x,req} \\ M_{z,req} \end{bmatrix} = \begin{bmatrix} \frac{1}{r_w} & \frac{1}{r_w} & \frac{1}{r_w} & \frac{1}{r_w} \\ -\frac{t_f}{2\,r_w} & \frac{t_f}{2\,r_w} & -\frac{t_r}{2\,r_w} & \frac{t_r}{2\,r_w} \end{bmatrix} \begin{bmatrix} T_{fl} \\ T_{fr} \\ T_{rl} \\ T_{rr} \end{bmatrix} \quad (4.33)$$

This way, as long as the QP problem is solvable, the global force request becomes feasible, since it is created from a feasible combination of actuator torques. This also allows for the control allocator to minimise for power loss if there are more than one solution.

4.4.5 Static Reference Tracking

To follow a driver's request, the matrices need to be modified to account for reference tracking and the disturbance matrices. The input x in the array **z** is changed to the error between the current states and the desired states.

$$e_x = \mathbf{x} - r_{ref} = \begin{bmatrix} \dot{v_x} \\ v_x \\ \omega \\ \beta \end{bmatrix} - \begin{bmatrix} \frac{F_{x,ref}}{m} \\ v_{x_{ref}} \\ \omega_{z_{ref}} \\ \beta_{ref} \end{bmatrix} \tag{4.34}$$

and the discrete state space equation is rewritten as

$$e_x[k+1] = A \underbrace{(e_x[k] + r_{ref})}_{x[k]} + Bu_{mpc}[k] - r_{ref} \tag{4.35}$$

Adding on disturbance matrices C and D:

$$\underbrace{e_x[k+1] = A \underbrace{(e_x[k] + r_{ref})}_{x[k]} + Bu_{mpc}[k] + C\delta_f + D - r_{ref}}_{\mathbf{x[k+1]} - r_{ref}} . \tag{4.36}$$

Now reformulating the equations to fit the syntax for A_{eq} and b_{eq} gives the following equations:

$$e_x[1] - Bu_{mpc}[0] = A(e_x[0] + r_{ref}) + C\delta_f + D - r_{ref} \tag{4.37a}$$
$$e_x[k+1] - Ae_x[k] - Bu_{mpc}[k] = Ar_{ref} + C\delta_f + D - r_{ref} \tag{4.37b}$$

This yields the following b_{eq}:

$$b_{eq} = \begin{bmatrix} A(e_x[0] + r_{ref}) + C\delta_f + D - r_{ref} \\ Ar_{ref} + C\delta_f + D - r_{ref} \\ \vdots \\ \vdots \\ \vdots \\ \vdots \\ Ar_{ref} + C\delta_f + D - r_{ref} \end{bmatrix} \tag{4.38}$$

which finalises the equality constraint. In this equation, $e_x[0]$ is fed into the QP as the current error. The input vector **z** no longer describes the states and control

action, but the error and control action.

$$\mathbf{z} = \begin{bmatrix} e(1) \\ e(2) \\ \vdots \\ e(N) \\ u_{mpc}(0) \\ u_{mpc}(1) \\ \vdots \\ u_{mpc}(N-1) \end{bmatrix} \tag{4.39}$$

4.4.6 Agile Reference Tracking

The reference tracking provided in the MPC is static, meaning that the reference signal does not change over the horizon. Although this might be fine for a single time instant or shorter period of time, it provides less desirable results the longer the horizon is. If for example, a static yaw reference is used and the vehicle then accelerates, the reference will no longer be accurate. The difference between a static and dynamic yaw reference for such a case can be calculated as

$$\Delta\omega_{z_{ref}} = \delta_f\left(\frac{v_x}{L_f + L_r + mK_u v_x^2} - \frac{v_{x0}}{L_f + L_r + mK_u v_{x0}^2}\right) \tag{4.40}$$

for an initial reference velocity v_{x0} and actual velocity v_x. Note that this also applies to the steering angle provided by the user. This means that the MPC assumes the steering angle to be constant over the horizon. The proposed solution to this problem is to update the steering angle across the horizon. This is done through Taylor expansion of the signal, using derivatives to predict future reference values. The predicted steering angle $\delta_{f,pred}$ at a future time instance t_{pred} is then expressed as following:

$$\delta_{f,pred}(t_{pred}) = \delta_f(t_0) + \delta_f'(t_0)t_{pred} + \delta_f''(t_0)\frac{t_{pred}^2}{2!} + \cdots \tag{4.41}$$

where t_0 is the current time step.

The derivatives of the steering angle are found using a Savitzky-Golay filter. The filter fits a polynomial to a specified amount of datapoints using least squares minimisation. It is also possible for the filter to output the signals' derivatives of different orders. Deciding on a sample size for the filter depends on the sensor noise and the delay that the controller can handle. For an accurately predicting filter, the first and second derivatives were used to complete the second order Taylor expansion seen in equation 4.41. The error term can now be expressed as

$$e_x[k+1] = A(e_x[k] + r_{ref}[k]) + Bu_{mpc}[k] + C\delta_f + D - r_{ref}[k+1] \tag{4.42}$$

where r_{ref} is a vector with length N (same as the prediction horizon). This method can be used to create dynamic reference points for yaw rate and velocity as well.

Figures 4.2a and 4.2b show the reference prediction error between different methods of prediction for a prediction horizon of one second. It can be seen that the prediction using the first derivative filter is quite oscillatory. This is due to the long prediction horizon. A more stable result can be observed in Figures 4.3a and 4.3b, where the prediction horizon is reduced to 0.25 seconds.

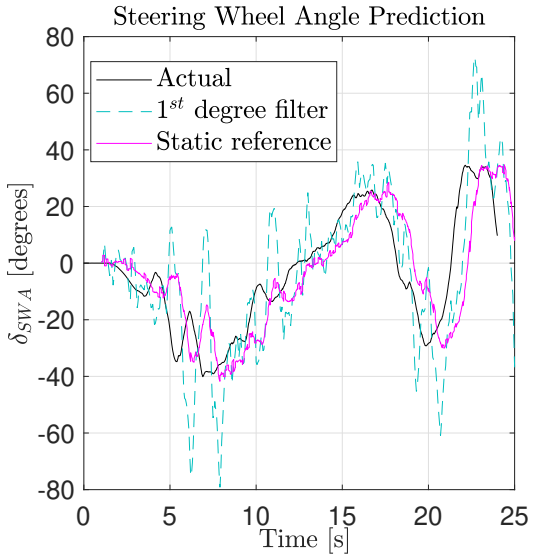

(a) 1 second horizon prediction vs actual steering angle after 1 second

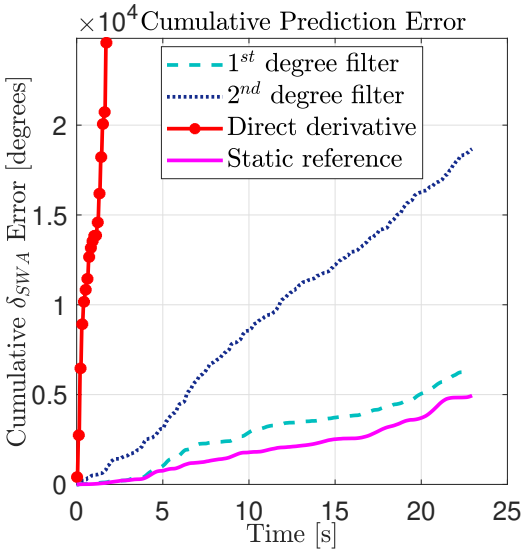

(b) Cumulative error over a 25 second period on normal road conditions

Figure 4.2: 1 second prediction horizon using different prediction methods.

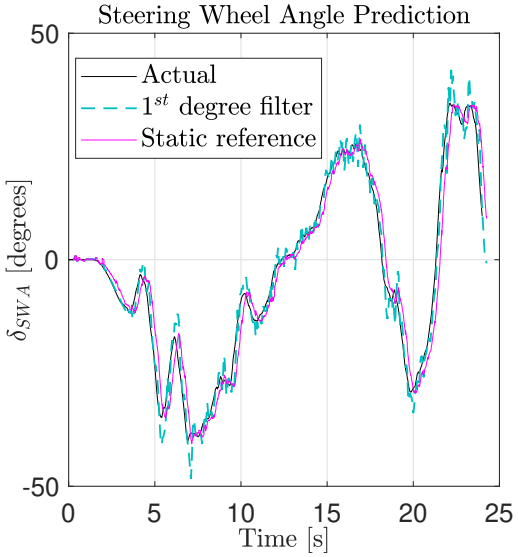

(a) 1 second horizon prediction vs actual steering angle after 0.25 seconds

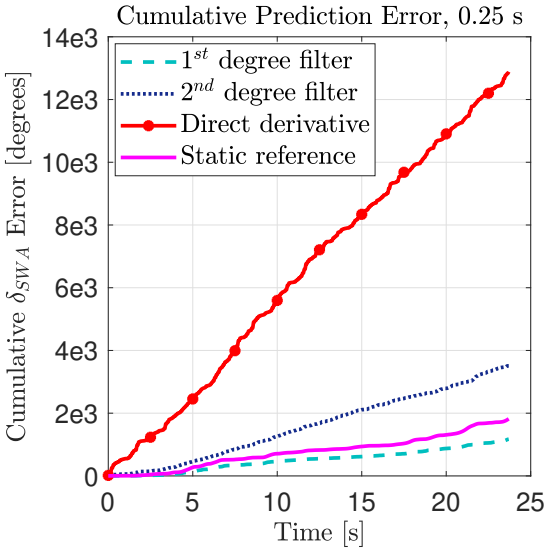

(b) Cumulative error over a 25 second period on normal road conditions

Figure 4.3: 0.25 second prediction horizon using different prediction methods.

The result was that with any amount of noise added, the direct derivative and second degree filter are too unreliable to use for prediction. For highway driving with a long prediction horizon, the static reference was generally found to perform better than the first degree filter. This is due to the fact that highway driving usually does not require a lot of steering. Most of the steering done was in order for the driver to stay on a straight or slightly curved road. For this case, the first order derivative will expect larger changes and hence does not accurately predict the future steering action from the driver. Using a shorter prediction horizon, however, the first degree filter was found to perform better than the static reference. This also holds for longer prediction horizon when driving through long turns. The 1st degree filter is preferred over the static reference, as the horizon steps closer to the current time will affect the MPC more. It should also be noted that the 1st degree filter always assumes a more aggressive steering than the static reference, which leads to the MPC being more conservative with longitudinal force. If the driver were to continue turning like the 1st degree filter predicts, the static reference MPC would likely turn infeasible at some point.

4.4.7 Relaxing the Controller Output

Using the output vector from the MPC as an equality constraint in the control allocator ensures that the acceleration and yaw moment requested are met. However, in normal driving conditions exact output from the vehicle yaw rate and velocity are not needed. In these cases, it could be more advantageous to relax the constraints and give the power loss minimisation algorithm more freedom. This thesis mainly focuses on adapting the controller for a range of yaw rates, and not acceleration requests.

Hence, a proposed change is to provide the low level controller with the output vector $\mathbf{v}_{req} = [v_{max}, v_{min}]$ as an inequality constraint instead, forcing the vehicle to behave within a certain range of velocities and yaw rates. The power loss minimisation then has the possibility to not fulfil the requested velocity and yaw moment, if the vehicle still behaves within the provided limits. If an extreme scenario appears, the minimum and maximum requests will approach each other (ideally take on the same value), forcing the output and neglecting power loss minimisation. Then after such a scenario, power loss would once again be in focus.

The newly proposed request vector is generated from the driver's steering input, using two different understeering characteristics. These understeering characteristics will decide on how big of a range the yaw rate is allowed to vary within. The specific values could be determined by for example the manufacturer (as a factory setting) or by the driver directly. The limits are found according to

$$\omega_{z,max} = \delta_f \frac{v_x}{L + mK_{u,min}v_x^2}, \quad \omega_{z,min} = \delta_f \frac{v_x}{L + mK_{u,max}v_x^2} \tag{4.43}$$

where K_u is the understeer coefficient, $\omega_{z,max}$ is the yaw rate for a more aggressive steering, and $\omega_{z,min}$ is the yaw rate for a more relaxed controller output. K_u is usually a constant based on vehicle parameters. With this controller, however, it is

possible to use a desired K_u, which is the parameter to be determined.

To find the two different controller actions, two different controllers have to be run. This will double the execution time of the MPC, but they can run in parallel. The inequality matrix b_{in} is changed to ensure that the aggressive controller will not go above $\omega_{z_{max}}$, and the relaxed controller will not go below $\omega_{z_{min}}$, see Appendix A. In these cases, the control will automatically adjust the torque output and the controller outputs would approach each other.

Finally, the control allocator is changed to have more relaxed constraints, giving more room for power loss optimisation during normal driving.

$$B \cdot \mathbf{u} = \mathbf{v}_{req} \quad \rightarrow \quad \mathbf{v}_{min} \leq B \cdot \mathbf{u} \leq \mathbf{v}_{max} \tag{4.44}$$

The vector that contains $\mathbf{v}_{min}$ and $\mathbf{v}_{max}$ will further be referred to as $\mathbf{v}_{des}$, and is sent to the control allocator, similarly to $\mathbf{v}_{req}$.

4.4.8 Barrier Method

When it comes to stability and driver expectations, lane keeping assist is found distracting by certain drivers, with a report from 2016 noting that more than 1 in 3 drivers prefer to drive without lane keeping assist [40]. Lane keeping is generally inactive, and then applies a force to the steering wheel when the driver is about to exit the lane. It is natural to make the comparison from exiting the lane to hitting the hard constraints on $\omega_{z_{max}}$ and $\omega_{z_{min}}$. The difference being that in the hard constraint case the controller will increase the requested moment significantly more than a lane keeping system, essentially jerking the vehicle back into the acceptable yaw rate range. It can be both irritating for the driver and unsafe if the driver is not prepared.

In addition, the controller will stop applying the extreme force once the vehicle is barely back in an acceptable range. The likely scenario is that the vehicle will once again drift out of range, repeating the process. It is very common for oscillations to occur, even if the driver is prepared. One solution to take inspiration from the previously mentioned lane assist system, and instead apply a softer force when the hard constraints are met, increasing drastically the further off the acceptable range the vehicle drifts. This is done by adding a slack variable and adding it to the inequality constraint:

$$A_{in} \cdot \mathbf{z} \leq b_{in} \rightarrow A_{in} \cdot \mathbf{z} - s \leq b_{in} \tag{4.45}$$

The slack variable is free for the solver to choose, as it does not affect anything physically. The caveat being that the cost for increasing the slack variable is set to be very high. The controller, when optimising, would attempt to keep the slack variable at zero at all times, only increasing it when the inequality constraint is violated or about to be violated.

Implementation of the slack cost can be implemented in the quadratic problem, as long as the $\mathbf{z}$ vector is extended accordingly.

$$\mathbf{z} = \begin{bmatrix} e(1) \\ e(2) \\ \vdots \\ e(N) \\ u(0) \\ u(1) \\ \vdots \\ u(N-1) \\ s(1) \\ \vdots \\ s(N) \end{bmatrix} \tag{4.46}$$

The matrix A_{eq} is not relevant to the slack variable, and is hence only extended with zeros to make matrix dimensions match up. The matrix A_{in} requires a slight extension to allow the slack variable to reduce the output to an acceptable level:

$$A_{in_{slack}} = \left[\begin{array}{c|cccc} & -1 & 0 & \cdots & 0 \\ & 0 & -1 & & \vdots \\ A_{in} & \vdots & & \ddots & \vdots \\ & \vdots & & -1 & 0 \\ & 0 & \cdots & 0 & -1 \end{array}\right] \tag{4.47}$$

One slack variable exists N times, as the constraint may be violated in each time step. One slack variable can only handle one constraint, but an indefinite amount of slack variables can be added at the end of $\mathbf{z}$. This will however, increase the computational complexity.

5

Test Setups for Verification and Validation

This section presents the tests performed in order to validate the intended functionality of the controllers and control strategies presented and discussed in Chapter 4. A comparison was also done between alternative controllers to provide a foundation for choosing which would fit best as a motion coordinator. With a working controller, tests have been done to compare the behaviour and driver response to a heavy vehicle without lateral control during emergency manoeuvres, with power loss minimisation impacting the dynamics of the vehicle. As discussed in Chapter 3, the main performance indicators are how much the driver has to compensate with steering wheel angle to stay on the road, how a sudden switch between propulsion axle affects the handling, and the ability to stop in emergency situations.

5.1 Controller Comparison

In order to determine the most appropriate motion coordinator style out of PID, LQR and MPC, two tests were done to appraise the performance difference between the three controller styles, an acceleration manoeuvre and a braking manoeuvre. The acceleration test was done with an initial speed of 50 km/h and a hand held steering wheel angle of 2° on dry asphalt ($\mu = 0.8$). The steering angle was kept static while the vehicle speed increased with 5 km/h after reaching steady state. The driver inputs can be seen in Figure 5.1a and 5.1b. The observed output was the vehicle yaw rate, to determine how the controller handles driver steering input. The goal of this test was to verify that all controllers work well during normal conditions, and to see whether an obvious difference in performance could be observed.

The brake test was done at a higher speed of 100 km/h, while cornering on dry asphalt. Hard braking was engaged after reaching steady state cornering. This aimed to analyse the controllers ability to assist in keeping the driver at the road, as well as keeping the reference yaw rate. The reference speed and road that the vehicle was travelling on can be seen in Figure 5.2a and 5.2b respectively. The path curve corresponds to a lateral acceleration of 2 m/s^2 for the initial velocity. The outputs observed was yaw rate, travelled path, steering wheel angle and vehicle velocity. The yaw rate and steering wheel angle were analysed to determine the controllers effect on the driver and the travelled path and vehicle velocity to analyse how effectively the controllers were able to come to a stop. In addition to the three controllers, a

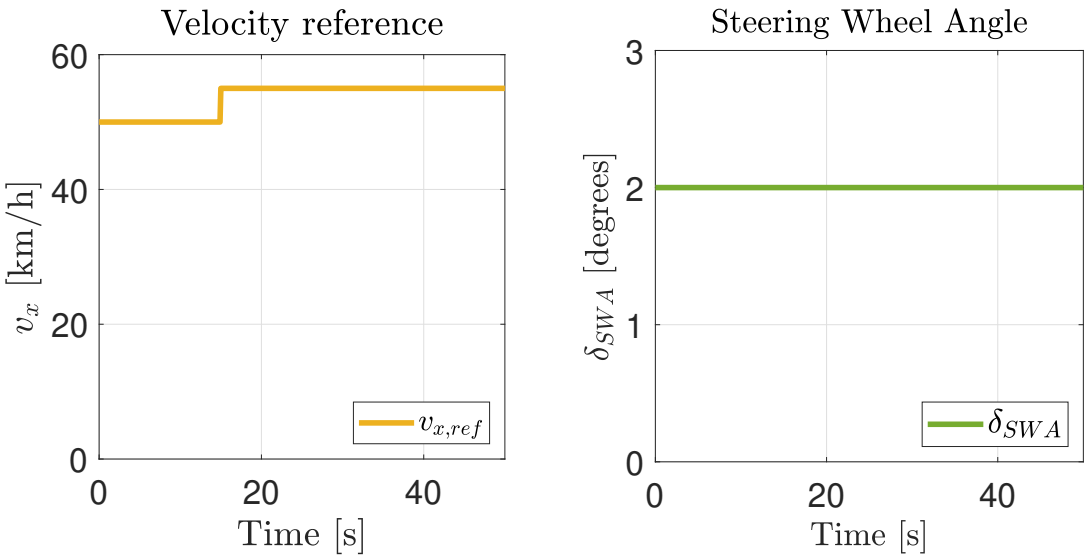

(a) Reference speed with step increase at $t = 15\,\text{s}$.

(b) Reference steering wheel angle.

Figure 5.1: Reference inputs for the forward acceleration manoeuvre.

final simulation was also ran without any motion coordination laterally. For this case, the axles were locked so that the left and right side produced the same output torque.

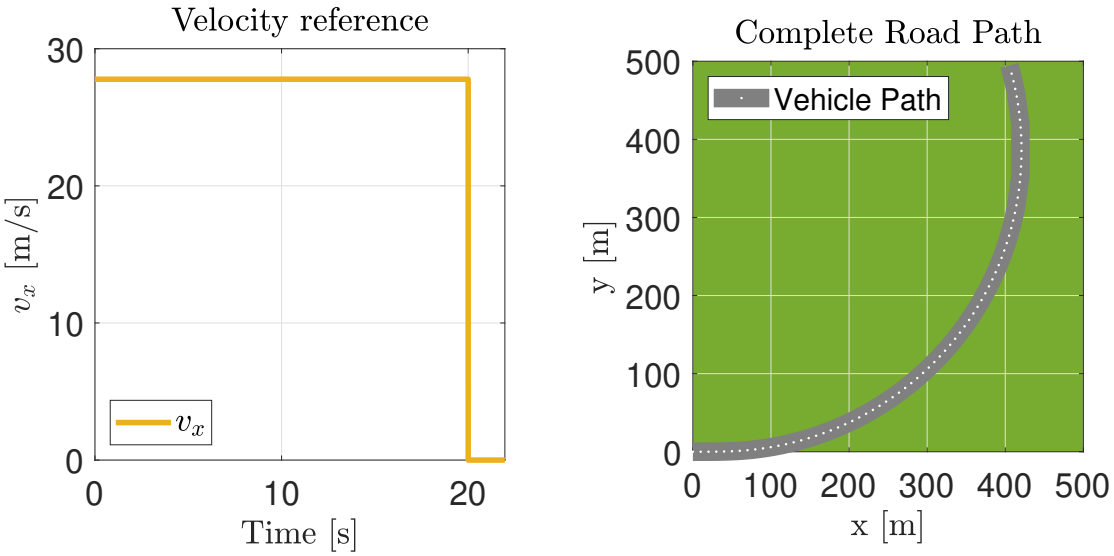

(a) Reference speed with hard braking at t=20 s.

(b) Reference path for vehicle with a 385 m radius (corresponding to $a_y = 2\ \text{m/s}^2$).

Figure 5.2: Reference inputs for the braking manoeuvre.

5.2 Feasibility at Tyre Limit

The purpose of using an MPC compared to the other controller structures, is that the MPC allows for limit inclusion. As explained in a previous chapter, an LQR cannot take actuator limits into consideration when calculating the optimal output. Instead, the output will be saturated post optimisation, which might make it non-optimal. To verify a correct implementation of constraints in the MPC, a test scenario with infeasible request combinations was constructed. The test aimed to put the driver and vehicle in a situation where it would be infeasible to maintain both the lateral and longitudinal forces requested. More specifically, the test challenged the constraints based on combined slip.

To expose the vehicle to a combination of high longitudinal and lateral forces, the vehicle was exposed to high speed through cornering. Since the challenge was to examine combined slip, the friction coefficient was set to 0.3, corresponding to driving on packed snow. This choice was made to avoid consideration for roll over. Note that the MPC does not estimate the friction, instead it was set as a parameter. The test started at an initial speed of 15 m/s and then accelerated up to the highest top speed the MPC would allow. After reaching steady state at the maximum velocity, the driver engaged full braking. This tested the MPC's ability to prevent the driver requesting dangerous longitudinal forces and keep the needed yaw rate, while balancing longitudinal and lateral forces to stay on the road. The variables that were mainly analysed during the test was:

- The forces acting on the tyres, which was compared with the theoretical maximal forces to estimate whether the MPC behaved as intended.
- The vehicle velocity, to examine the maximally allowed speed and stopping time.
- The steering wheel angle, to see how the driver was affected
- The offset to centre line of the road, to see how well the MPC aided the driver in staying on the road.

5.3 Noise Impact on Controller

Next, the MPC controller's robustness was tested. This was done by adding noise on the signals to simulate measured sensor signals on a vehicle. The added synthetic noise were zero mean Gaussian noise, with variance as seen in table 5.1. The noise levels were determined from observation of real test data provided by Volvo.

The test case used to analyse the effect of additive noise was similar to the hard braking test in secction 5.1, but at a speed of 70 km/h. The vehicle started off at 70 km/h, entered a left hand curve and engaged hard braking after reaching steady state. The test was done at dry asphalt, so a friction coefficient of 0.8. The signals were measured to observe the noise levels and the steering wheel angle and vehicle yaw rate were observed to see the noises' effect on the driver behaviour.

Table 5.1: Variance and sample time of added artificial noise on sensor output.

Sensor Output	Variance	Sample Time
δ_f	$1e-5$	0.05
ω_z	$1e-5$	0.05
v_x	1	0.05
v_y	1	0.05
a_x	0.1	0.05
a_y	0.1	0.05

5.4 MPC Sample Time Comparison

The biggest drawback of using a MPC compared to other controller styles is the computational complexity that it brings. This causes a trade-off between the MPC performance and execution time. One way to influence the execution time of the MPC is through changing the sample time. While the change in execution time from doing this change is quite predictable, its effect on performance is harder to estimate. To analyse this effect, a test scenario was constructed and simulated with five different sampling times: 10 ms, 5 ms, 2 ms, 1 ms and 0.1 ms. This corresponded to the MPC being run 10, 20, 50, 100, and 1000 times per second, respectively. Note that no consideration for real time computing was taken into account.

The test scenario was once again constructed so that the driver entered a left hand curve at 70 km/h, and then engaged in full braking. The test was done at packed snow and with added noise as seen in the last test. Observed outputs were steering wheel angle from the driver and vehicle yaw rate.

5.5 Validation and Performance of Relaxed Request

Before comparing the effectiveness of a relaxed request and a hard constraint request, the viability of implementing a relaxed request was analysed. The relaxed request outputted a minimum and maximum $\mathbf{v}_{min}$ and $\mathbf{v}_{max}$ to the control allocator, instead of an equality constraint. The theory is that the minimum and maximum request should converge during critical scenarios, and otherwise let power loss operate as intended. However, power loss may use any request within the span. This could result in unpredictable behaviour, generating an output neither request is looking to achieve.

The test aimed at creating an extreme scenario, where the control system was tested at its limits. The vehicle started at 50 km/h, driving on packed snow($\mu = 0.3$) into a left hand turn representing 1.12 m/s^2, and then accelerates as much as possible before the MPC reduced the torque output. At 20 seconds, the driver attempted

to fully engage the brakes. The MPC needed to both keep the yaw rate steady in the acceleration and braking, and also manage the acceleration while staying within the bounds of limited friction. The driven path, steering wheel input and vehicle velocity for the test can be seen in Figure 5.3.

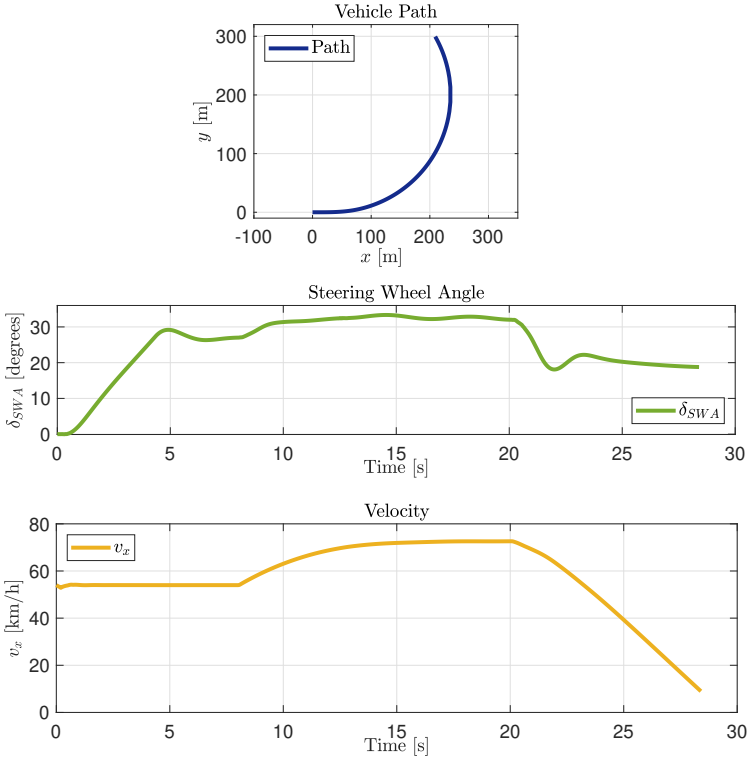

Figure 5.3: Test setup for validation of relaxed request. The driver model was requested to accelerate as much as possible, and then brake to zero m/s.

5.6 Soft Barrier Test

The MPC had tendencies to oscillate when meeting the hard constraint, even when the input from the driver was constant. A test was set up at high speed to showcase this. The steering wheel angle was slowly increased up to 14° to simulate entering a curve, and the vehicle then accelerated as much as possible, followed by hard braking to standstill. The vehicle path, velocity and reference steering wheel angle can be seen in Figure 5.4. The test was repeated for a motion coordinator both with and without a soft barrier. The observed outputs were the vehicle yaw rate and actuator output to each wheel.

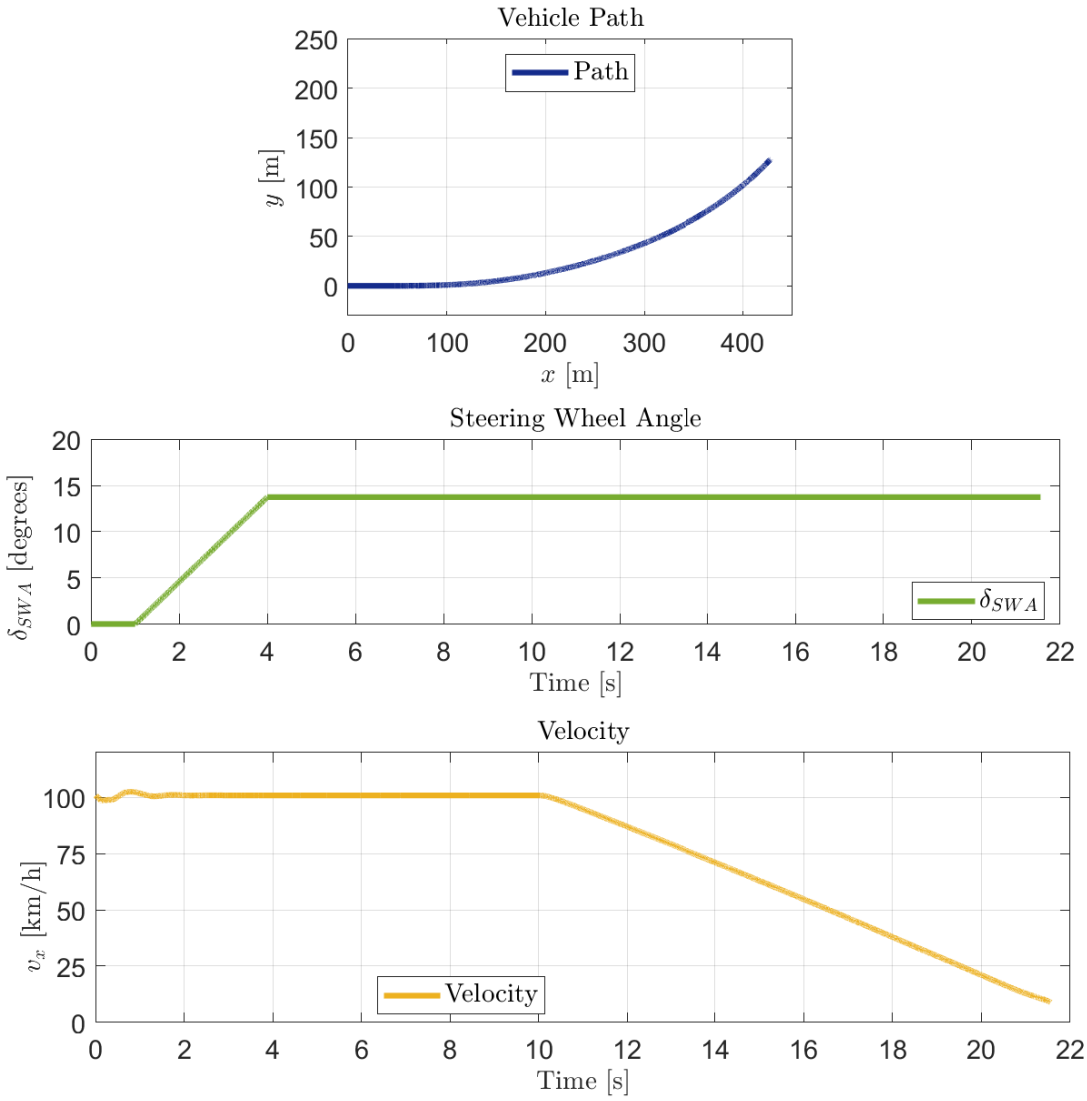

Figure 5.4: Movement of the vehicle for the barrier test. High speed was used as it causes more oscillations.

5.7 Emergency Braking while cornering

Predictability in emergency manoeuvres, which was discussed in Chapter 3, showed that control of all four wheels without any lateral control made the vehicle unstable to handle. To analyse the performance of the implemented control structure, the test presented in Figure 3.2 was repeated, but with the yaw rate controller enabled. This meant that the vehicle, with an initial speed of 80 km/h, entered a left hand curve, corresponding to a lateral acceleration of $1\,\mathrm{m/s^2}$. After reaching steady state cornering, the driver engaged hard braking until fully stopped. The MPC's purpose in this test was to assist the driver in handling the vehicle and prevent driving off the road.

5.8 Mode Switching

When introducing power loss optimisation, it was shown that a disturbance might occur as the propulsion axles engage and disengage. This was referred to as mode switching and was analysed for the developed control structure. To test this, the two previous observations were repeated and the test was also run with the yaw rate controller activated. The two test scenarios were switching during high longitudinal acceleration and during high lateral acceleration.

The first test started at 65 km/h, entering a left hand curve and reaching steady state cornering. Then, the vehicle started to accelerate for 5 seconds before the mode switch took place. The test was done at dry asphalt ($\mu = 0.8$).

The second test was done from an initial speed of 35 km/h. The vehicle entered a left hand curve and started to accelerate until reaching 55 km/h. At this point, the truck had a lateral acceleration of around 0.4g. The mode switch was then executed, observing how the steering wheel angle from the driver changed.

For both test cases, the switch was done on both directions (from power mode to cruise mode as well as cruise mode to power mode).

5.9 Rollover Prevention

Torque vectoring can be used to improve the lateral performance of the vehicle by creating an additional yaw moment. This will, however, increase the risk for rollover as the lateral forces increase. Hence, there was an interest in observing and preventing the risk of rollover using the MPC. The risk for rollover is mainly present for a truck with semitrailer or articulated vehicles, which is not treated in this thesis. Instead, this functionality is mainly aimed at proving that it is possible to control both the yaw rate and the lateral acceleration at the same time.

The test setup was done with the steering wheel locked at a 30 degree angle. The MPC was then asked to increase the speed to the point of failure, where the goal was to have the MPC stay within the limit of lateral acceleration and yaw rate, sacrificing speed for the sake of stability.

5.10 Comparison of Power Loss Optimisation and Power Usage in Forced and Relaxed Request

To understand the impact of the boundary relaxation implementation described in chapter 4.4.7, it is important to observe how the power usage is affected. The tests analysed the impact on power usage in a common driving scenario, comparing the direct request v_{req} with the relaxed boundary constraint v_{des}. Performance factors such as velocity and steering wheel angle were also observed, to have a

better understanding of trade-off between power use and performance.

This test aimed to analyse the power consumption characteristics of the two different request strategies during a single manoeuvre scenario. To achieve this, the vehicle was accelerated through a left hand curve in moderate speed on dry asphalt. The initial speed was 60 km/h and the radius of the curve corresponded to 2 m/s^2 of lateral acceleration. The vehicle then accelerated to 67 km/h after reaching steady state. The simulation was stopped based on distance, to ensure correct comparison of power usage. The complete road used for the simulation can be seen in Figure 5.5.

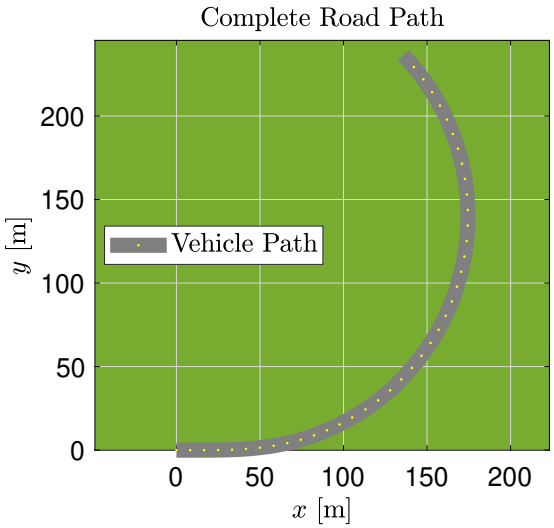

Figure 5.5: Road input for simulation.

5.11 Short Haul Power Use Simulation

In the previous test, the instantaneous power use and power loss was tested, but it was also important to observe the total power use over a longer drive cycle. During normal use cases, such as driving on a country road with good grip and few turns, the yaw rate controller does not need to be active the majority of the time. The purpose of a relaxed motion coordinator request is to determine when the yaw rate controller need to act, and to avoid using more power than needed. To analyse whether this held true, a test scenario was set up with a 2.5 km road from Hällered to Alingsås. The road path and height change can be found in Figure 5.6 and 5.7.

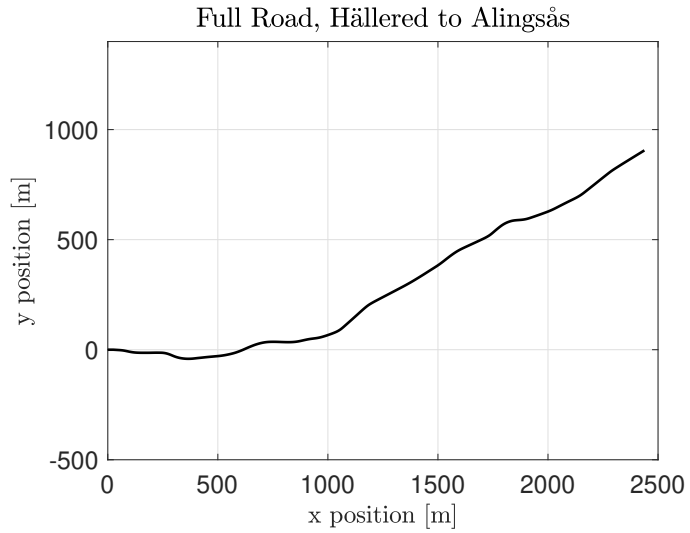

Figure 5.6: Road change over time for a 2800 m snippet between Hällered-Alingsås.

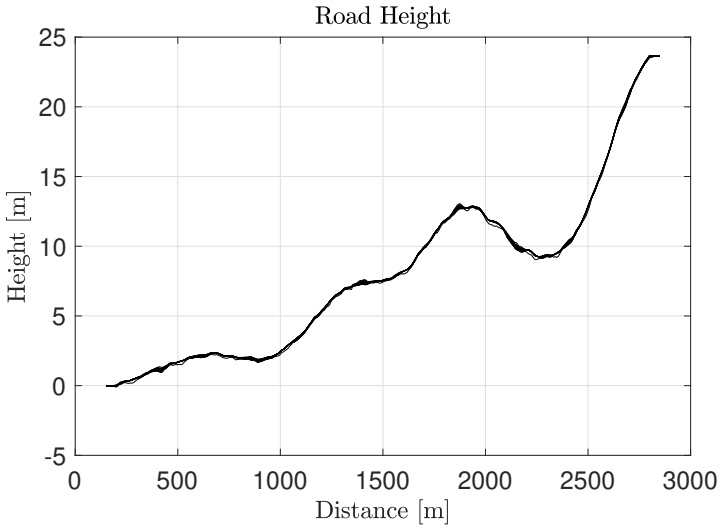

Figure 5.7: Road height change over time for a 2800 m snippet between Hällered-Alingsås.

6
Results

This chapter presents the results found from running the test simulations as described in the previous chapter. The tests performed follow the same order as chapter 5. All tests were done using an empty tractor, without trailer or external load.

6.1 Controller comparison

Two tests were done to compare all three discussed controllers: PID, LQR-LPV and MPC. The first test was done with a static steering angle and step increase in velocity. The results from this test can be found in Figure 6.1. Here, it can be observed that all three controllers behaved quite similarly and as intended. It can also be seen that the MPC had a slightly longer time response to the step, compared to the PID and LQR. This might depend on the fact that the MPC used its own weighting between longitudinal force and yaw moment, effectively using a slightly modified reference signal. The other two controllers, used an external PI cruise controller. It is also observed that the MPC had a bit more stable response as it oscillated less than the other controllers. Otherwise, no major difference is seen between the controllers.

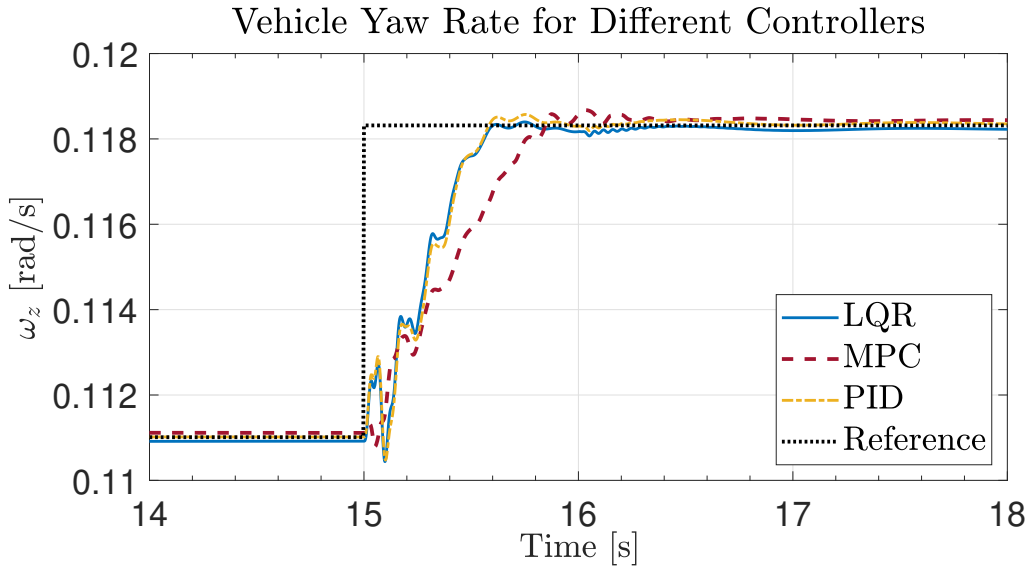

Figure 6.1: Yaw rate of the vehicle, using different controllers to generate the requested global forces. The control allocator was the same in all 3 test cases.

The next test was to compare hard braking in a curve at high speeds and the results from this test can be found in Figure 6.2. It can be seen that "no lateral control" case required significant steering compensation from the driver to stay on the road. The goal of the motion coordinator was to aid the driver in stopping quickly, safely, and without excess steering wheel compensation. Due to the positive rotational movement caused when braking in a curve, keeping a reference steady state yaw rate can be very difficult. It can be noted that all three motion coordinators vastly reduced the steering compensation needed by the driver when hard braking, and all three motion coordinators reduced the braking distance. There was, however, still a performance difference between PID, LQR and MPC. Looking at the steering wheel angle, the controllers behaved similarly at the start of the braking, where the driver model reduces the steering wheel angle to accommodate for the yaw moment induced. As the MPC used its own longitudinal control that was coupled with the lateral control, it was able to accommodate for the reduction in lateral forces due to the high longitudinal forces. This allowed the driver to compensate less with the steering wheel.

The combination of lateral and longitudinal performance can also be seen in the braking distance, as the MPC focused on stabilising the vehicle at the start of braking, which then allowed it to brake harder towards the end. This shows that even without considering constraint testing, the MPC outperformed the other controllers. For this reason, further tests were done exclusively with MPC.

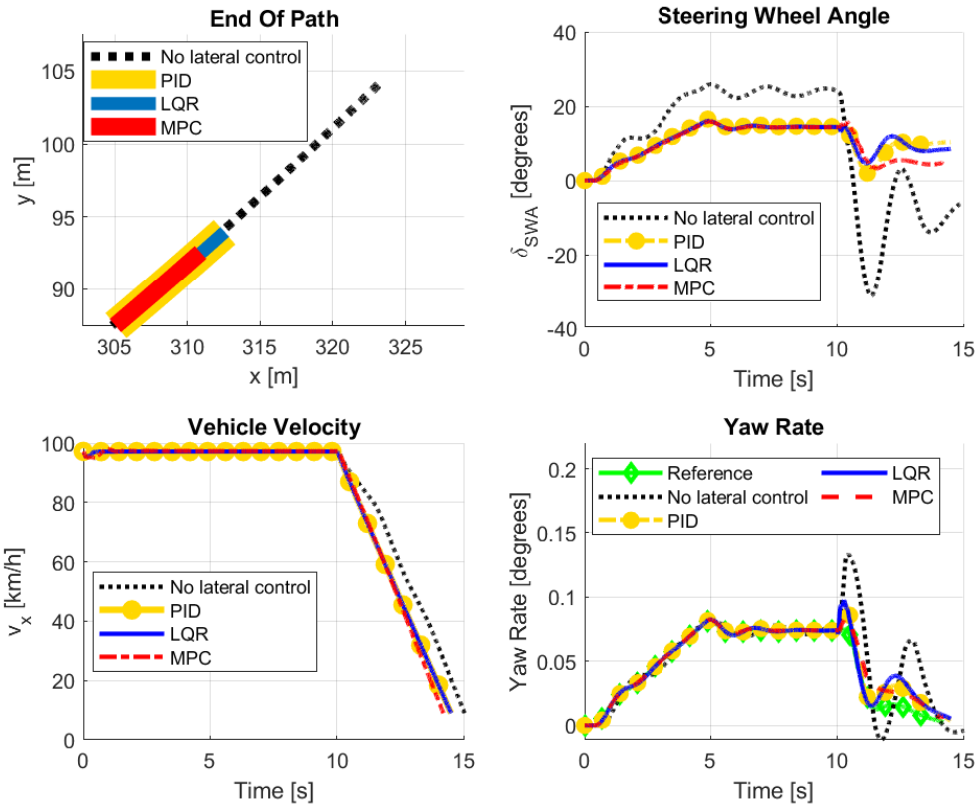

Figure 6.2: Steady state corner at 100 km/h. Test setup to compare PID, LQR, MPC and no latereral motion coordinator. Hard braking engaged at t = 10 s.

6.2 Feasibility at Tyre Limit

This test was done with the aim of seeing how the MPC handles saturation of the tyre forces. By engaging hard braking, from a high speed, in a curve, on low friction surface the lateral and longitudinal forces reached their limits. It was then no longer be possible to maintain both longitudinal and lateral velocity. This tested the internal friction circle constraints used in the MPC.

The resulting vehicle responses can be found in Figures 6.3b - 6.3d. Here, it is seen that the maximal velocity reached was around 75 km/h. It is clear that the MPC managed to limit the longitudinal forces to not lose lateral grip. The braking had a linear behaviour, suggesting that the manoeuvre was executed in a controlled manner. Looking at the steering wheel angle, it can be seen that the driver experienced an oversteered behaviour as the steering input decreased upon braking. This was caused by the rotational momentum of the vehicle which was hard to avoid due to the low friction. It can be seen from the centre line offset that the vehicle drifted off around 20 cm away from the middle.

The corresponding tyre forces together with estimated maximal forces are presented

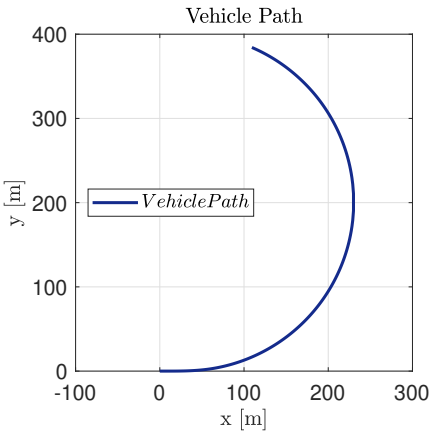

(a) Travelled path

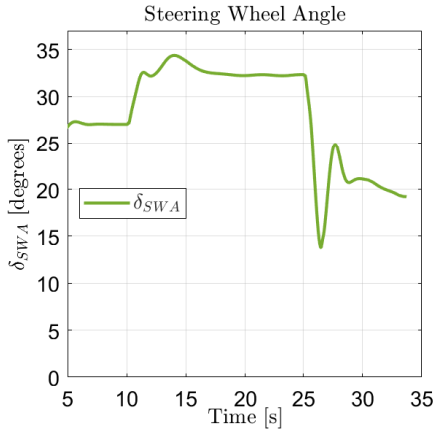

(b) Driver's steering input

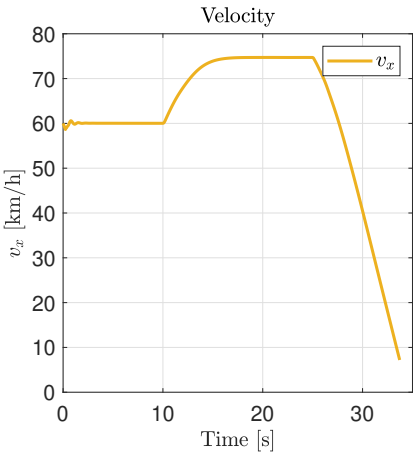

(c) Achieved velocity

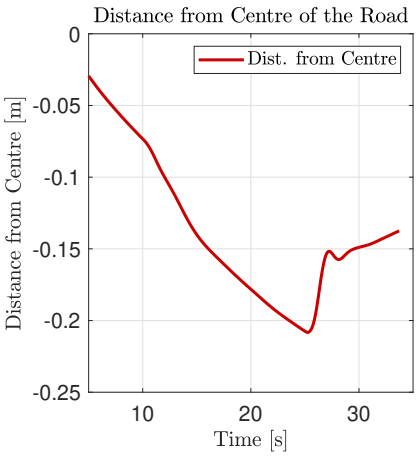

(d) Distance from centre

Figure 6.3: Resulting measurements from the tyre limit test.

in Figure 6.4. Here, $Friction_{Max/Min}$ refer to the estimated maximal and minimal tyre forces caused by combined slip, the radius of the friction circle; $Estimated_{Max/Min}$ shows the maximum and minimum output force in longitudinal direction due to a combination of friction estimation and actuator limits. If the friction is good, the actuators will limit the force, and if the friction is bad the tyre grip will limit the maximum and minimum force. Output F_x is the longitudinal force output from each tyre and "Used Tyre Force" refers to the magnitude of the force vector exerted by the tyre, expressed as $F_{tot} = \sqrt{F_x^2 + F_y^2}$. If the yellow line representing total output force crosses the friction limit, the tyre starts to slip. The reason the MPC does not allow the "Real force" to reach the the actual limit is the $\mu_{confidence}$ discussed in chapter 2.1.4. It directly scales the friction circle limit to $x\%$ of the real maximum. For this test, a safety factor of 0.8 was used. In addition, a secondary scaling factor of 0.95 was used when accelerating to avoid a situation where the driver was unable to brake, due to the entire friction circle being occupied by lateral forces.

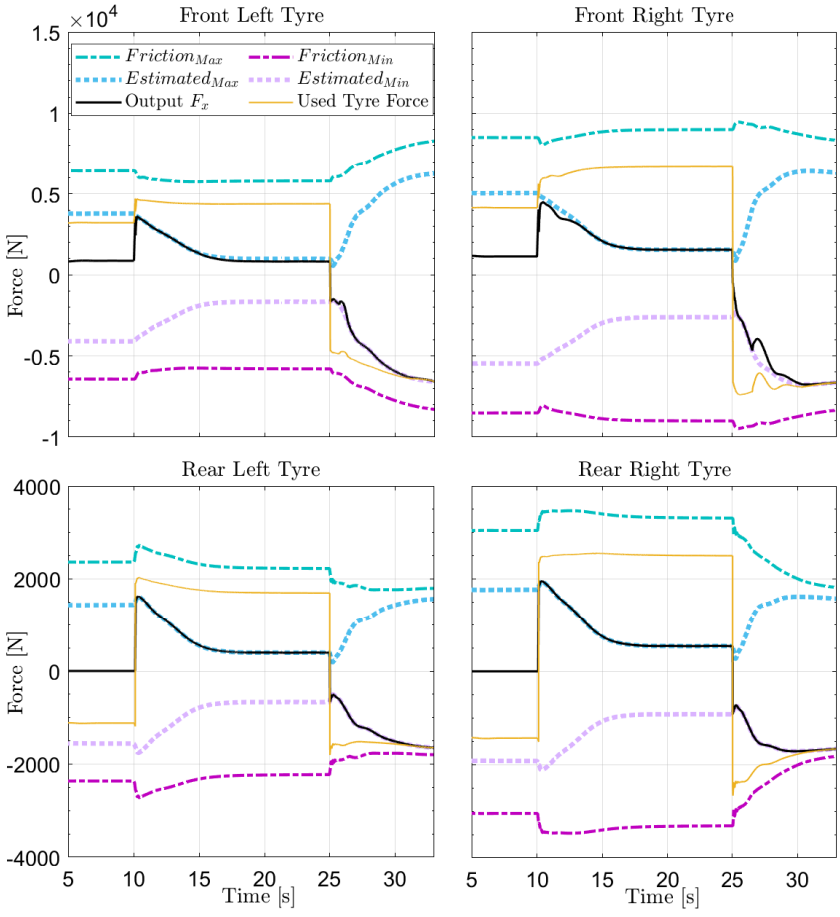

Figure 6.4: The forces compared to the upper and lower constraints and the real friction limit.

6.3 Noise Impact on Controller

A test was done to analyse the MPC's capability of handling noisy input. The noise parameters can be found in table 5.1. The resulting sensor data can be seen in Figure 6.5. Here, it is clear that the measurements from the steering wheel angle were noisy, compared to the other measurements. Particularly the yaw rate measurements had a low variance noise. The simulation results corresponding to these inputs can be found in Figure 6.6. Here, it can be seen that the MPC performed similarly to having no noise at all. A slight change in yaw rate and steering compensation can be seen, but the change was so small that it would likely be unnoticeable in reality due to vehicle inertia and steering wheel deadband.

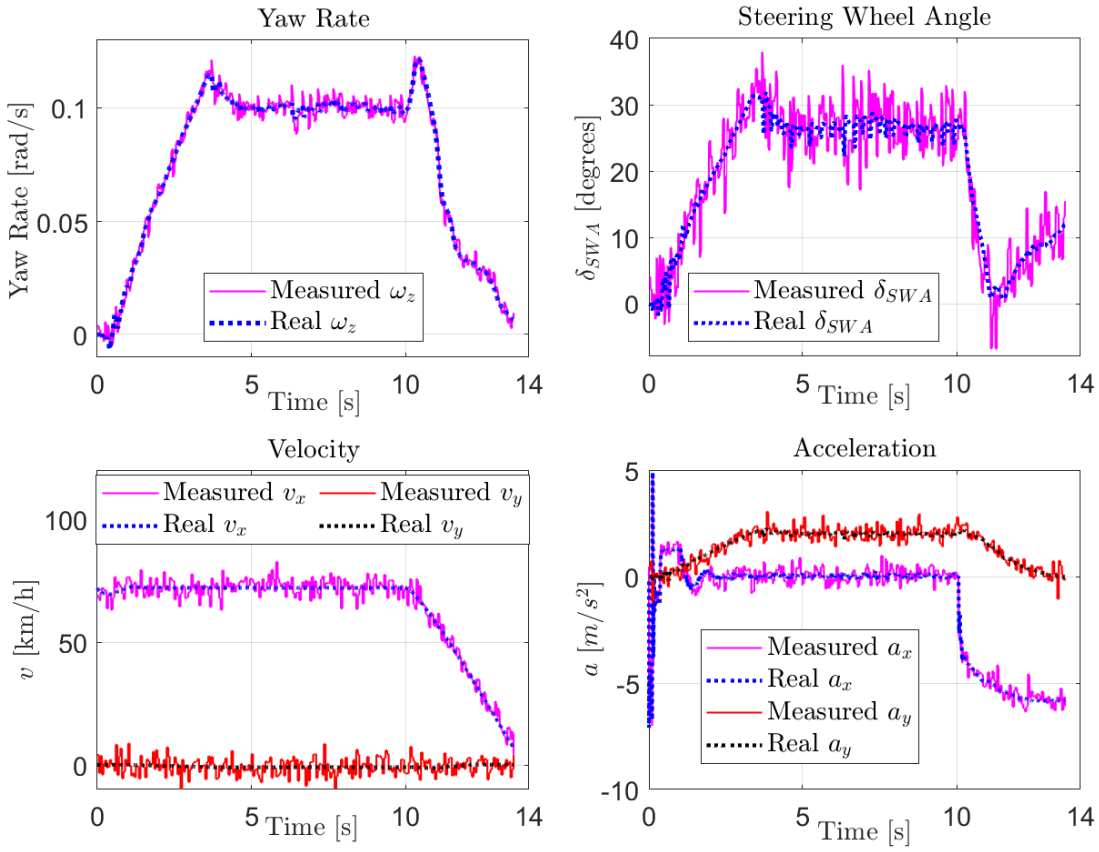

Figure 6.5: Noise on the sensors compared to real values. The steering angle value moved slightly due to the driver model, but was within the steering wheel deadband.

6.4 MPC Sample Time Comparison

When using an MPC, a compromise has to be made between performance and execution time. A test was done to examine the impact of execution time on the MPC performance. The resulting output can be seen in Figure 6.7. Here, the result for frequencies of 10, 20, 50 and 100 Hz were plotted, while the case of 1000 Hz was left out, since it completely coincided with the 100 Hz test and no additional

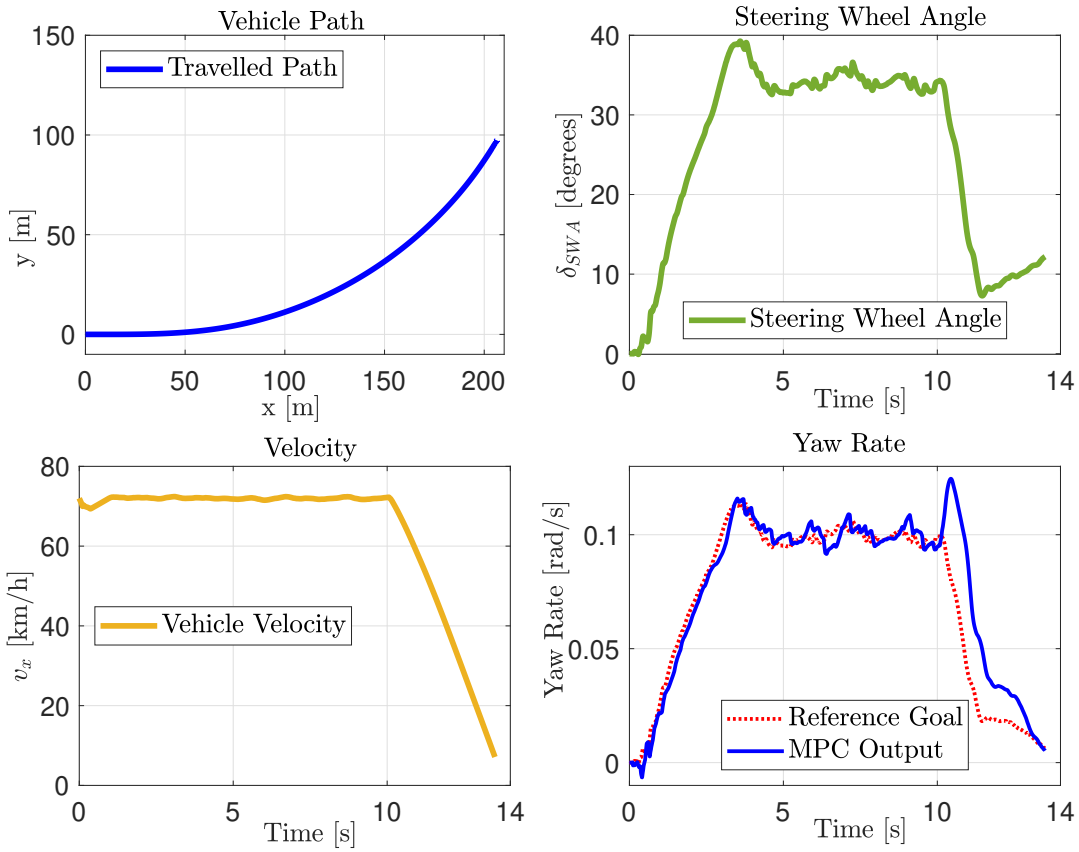

Figure 6.6: MPC performance with noise.

benefits were observed. The two noticeable performance indicators in the test were stability and braking distance. An MPC execution rate of 10 Hz caused significant oscillations in the yaw rate, and the driver seemed uncomfortable with the vehicle behaviour, as can be seen on the steering wheel angle.

The stability performance difference between a sample rate of 20 Hz and higher rates was generally negligible, but a slight difference could be seen in the braking distance. In the simulation, the 20 samples/second controller had a braking distance of approximately 3 meters longer than the more frequently sampled controllers. This was likely due to the higher sampled controllers being updated more often and hence captured the change of velocity and steering wheel angle quicker. From this result it can be seen that a sample rate lower than 20 Hz was unwanted due to inaccuracy, but higher sampling than 50 Hz did not seem to contribute with significant benefits in performance. Thus it can be summarised that the sampling time should be between 20 - 50 Hz.

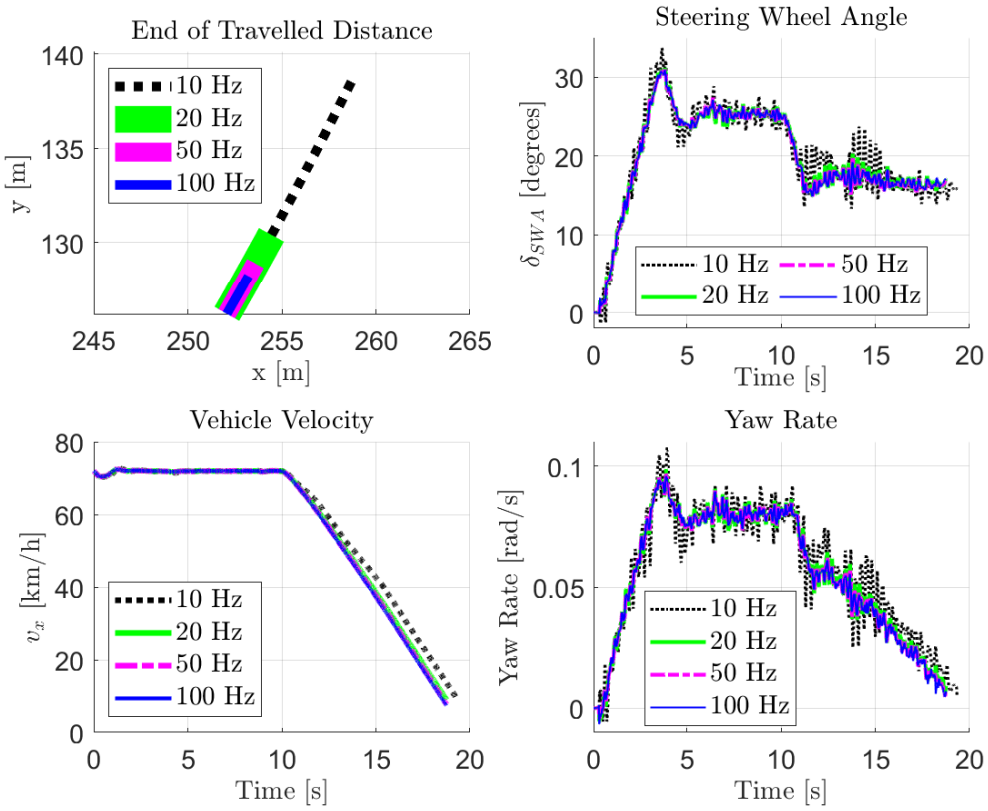

Figure 6.7: Comparison of MPC motion coordinators with different sampling time.

6.5 Validation and Performance of Relaxed Requests

The validation test for a relaxed request motion coordinator showed very promising results, which can be seen in Figure 6.8 and 6.9. In Figure 6.8, the yaw rate stayed within the set constraints (in red and blue). The control allocaton opted to aim for the more relaxed yaw rate, due to the power loss reducing actuator effort. On the other hand, when the vehicle started braking, the more aggressive target was used for guidance as this required less actuator output in the opposite direction. In the latter figure, it is clear that also the yaw moment was being kept between the aggressive request (orange) and the more relaxed request (blue). The vehicle naturally operated between the two ranges, until the vehicle accelerated at 8 seconds. The vehicle then coincided with the lower constraint for the minimum acceptable yaw rate, and the motion coordinator moment request spiked. For the control allocator, the difference between these two requests were the range of possible moment outputs.

In practice, the power loss optimisation will often use the least amount of yaw moment possible, as that reduces the power the most. The v_{des} request style can be seen as similar to a lane keeping system, except that it ensures that the vehicle behaves within a certain range of driving dynamics, instead of staying within a lane.

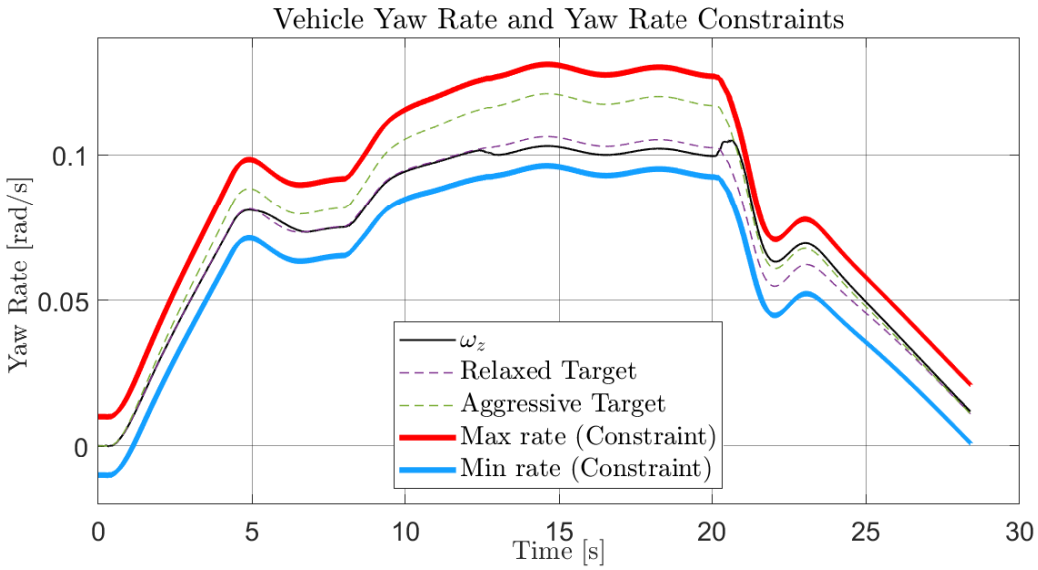

Figure 6.8: The vehicle yaw rate compared to the upper and lower constraints.

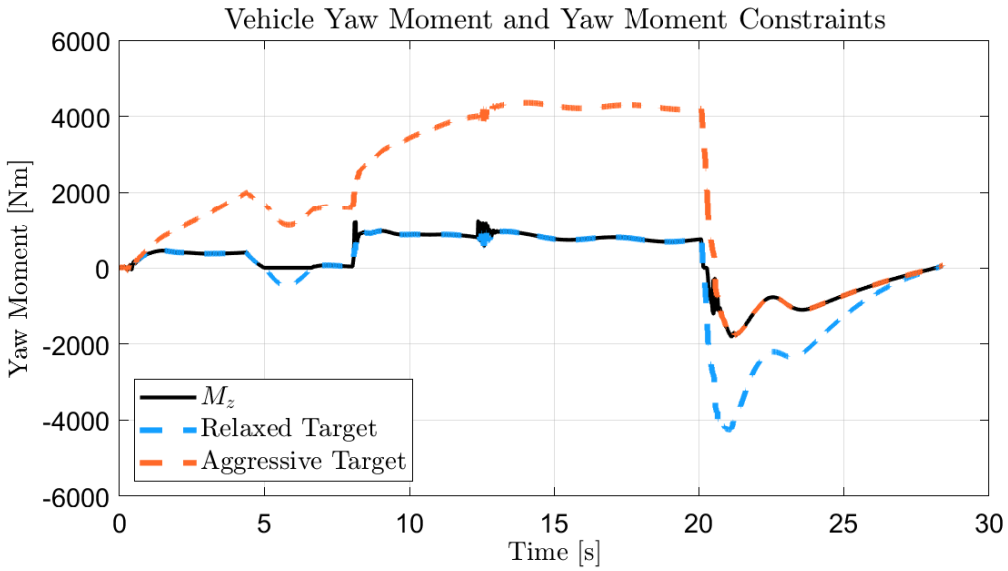

Figure 6.9: The controllers representing the range approach. The control allocator was free to operate between the two outputs.

6.6 Soft Barrier Test

To mitigate the occasional oscillations in the control output, a soft barrier was implemented. A test was done at high speed and while cornering to showcase the need for this implementation. The test was then repeated for a MPC with the soft barrier implemented to show the improvements. It can be seen in Figure 6.10 that the control system struggled while the yaw rate was on the border of the set constraint. Once the vehicle started accelerating, the MPC had difficulties prioritising between yaw rate and acceleration, and the hard constraint was met. Once the hard constraint was violated, the MPC request oscillated between the yaw rate constraint control action and the much more relaxed normal control action. There was a clear need for a hard constraint, but the difference between no violated constraint and a barely violated constraint needed to be softer. The corresponding actuator forces can be found in Figure 6.11. Here, it is obvious that the MPC caused a lot of unwanted oscillations.

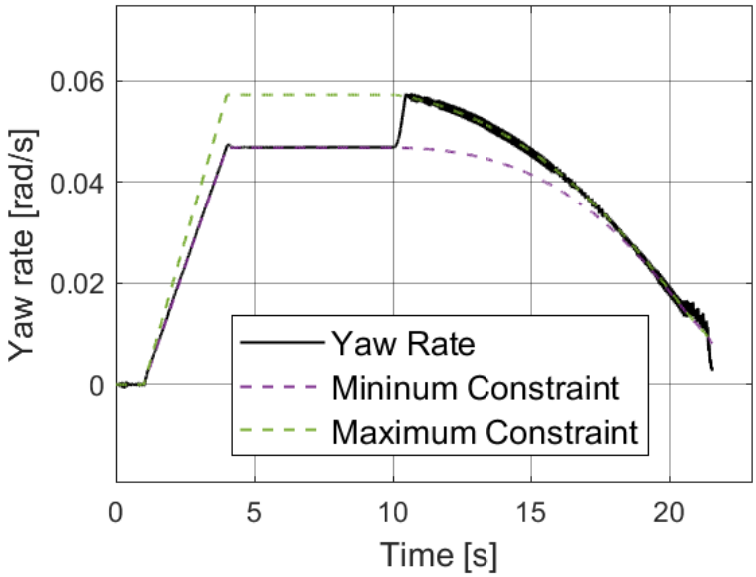

Figure 6.10: Yaw rate change with hard constraints. As the MPC maximised the actuator output in order to create a feasible output (within acceptable yaw rate), the control output oscillated when the driver started braking.

The result from implementing the soft barrier can be seen in Figures 6.12 and 6.13. The former graph shows the vehicle yaw rate and its constraints. By comparing it to Figure 6.10, it is clear to see that the oscillations were prevented and a better control was obtained. The former graph also indicates that the control output was much more robust as it did not contain any oscillations in comparison to Figure 6.11 as showed previously.

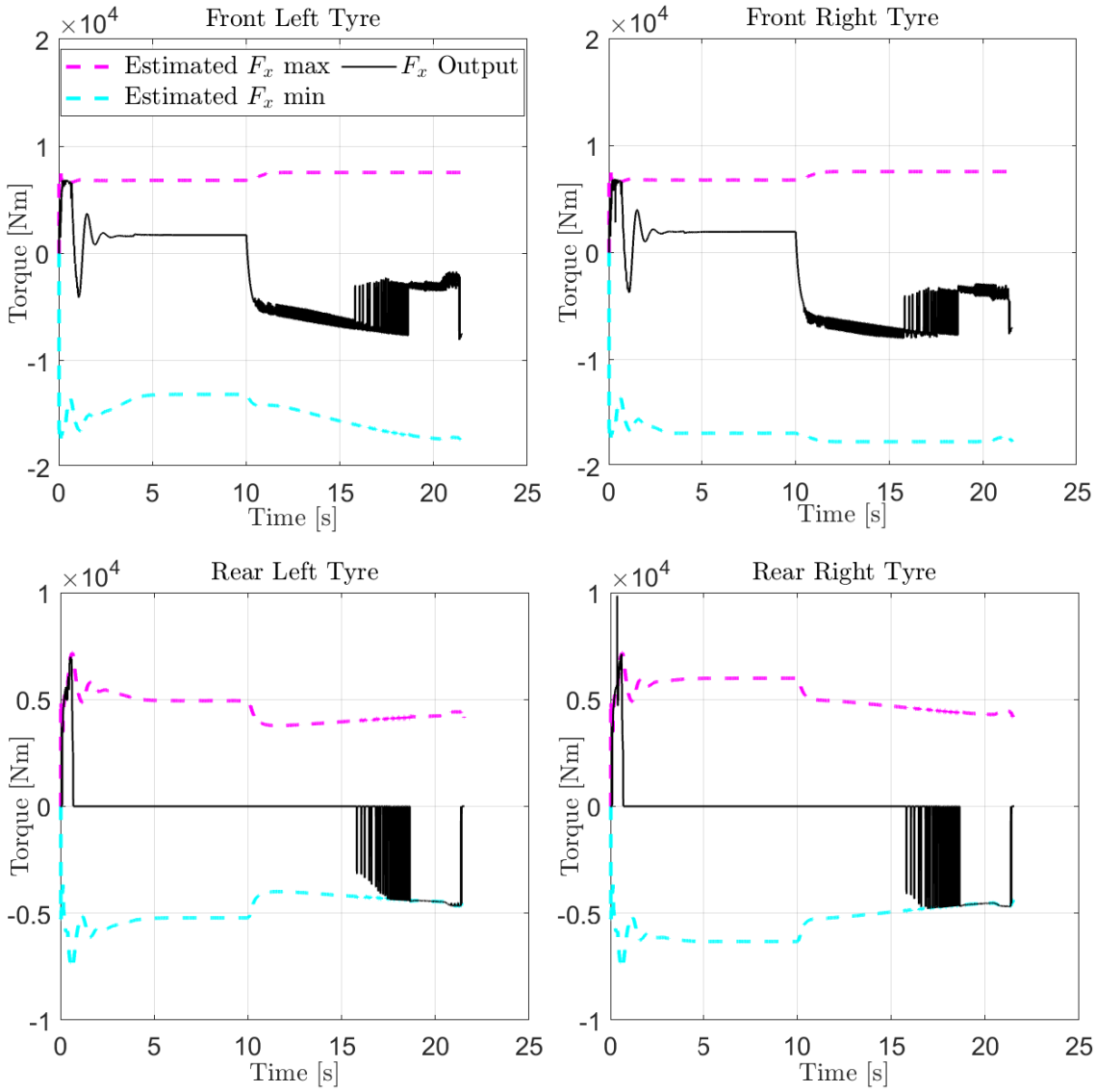

Figure 6.11: Torque use during the barrier test with hard constraints. Motor torque output oscillated wildly when the constraint was hit.

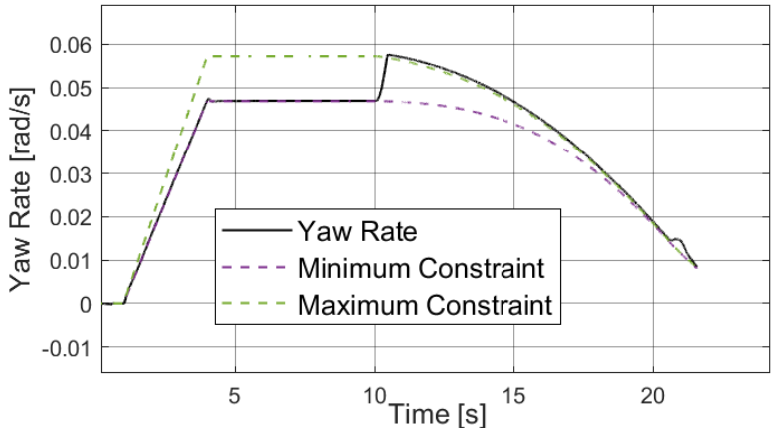

Figure 6.12: Yaw rate change with the implemented slack variable. There was a slight violation of the constraint, but the oscillations have been removed entirely.

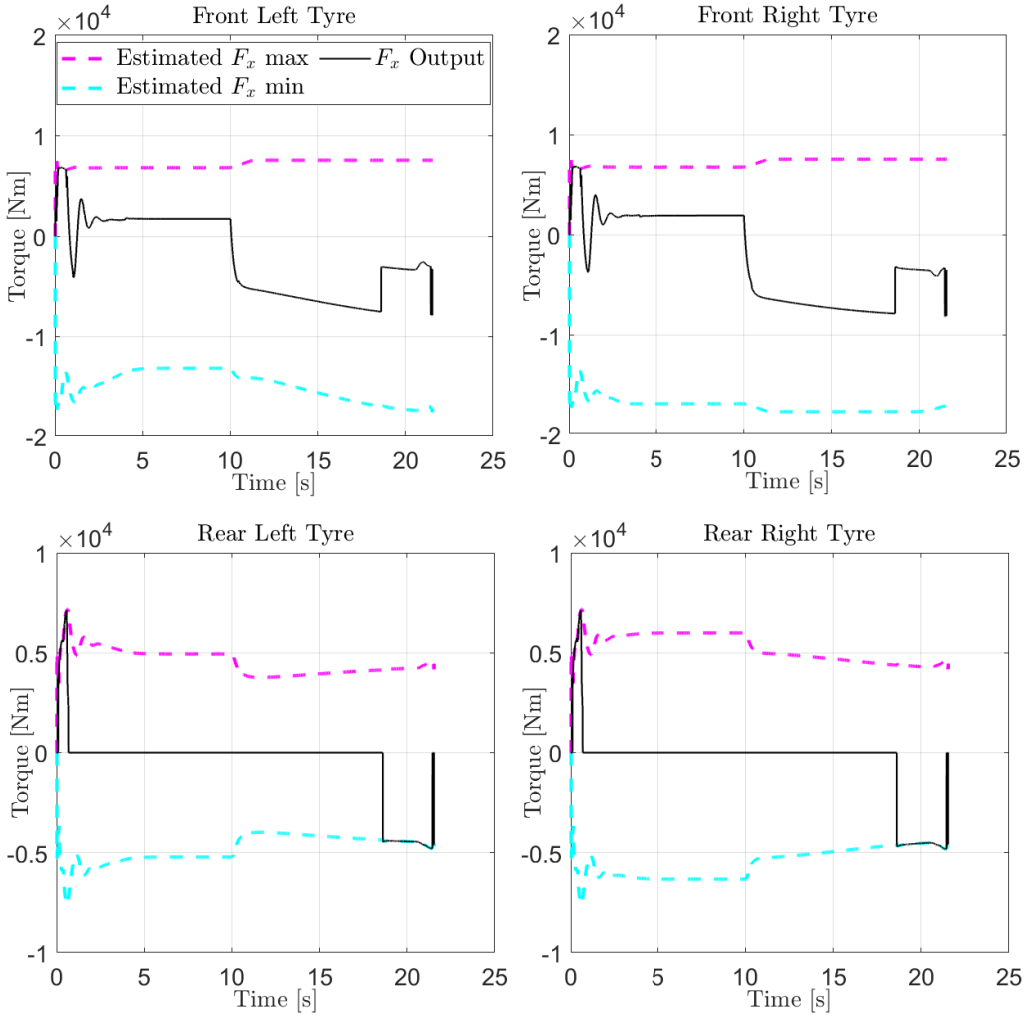

Figure 6.13: Wheel torque during the barrier test with the implemented slack. Motor torque output does no longer oscillate when the constraint is hit.

To summarise, the result shows that the soft barrier made the MPC significantly more robust, but performance took a mild hit. However, this was easily accommodated for by using more aggressive reference yaw rates. Execution speed was also lowered slightly. This was due to there being more variables to optimise for, as it was not immediately obvious what the correct output was, compared to hard constraints.

6.7 Emergency Braking while cornering

The performance of the MPC can be seen in Figure 6.14 and is here also compared to the previous observations. It can be seen that the yaw rate motion coordinator was better than the setups without torque vectoring in all aspects. The required steering compensation was almost completely eliminated. It did not exactly follow the optimal steady state steering angle which was presented in Figure 3.3, but such a controller would ignore all slower dynamics of the vehicle, producing a very jerky driving experience. As an additional note, the vehicle came to a complete stop faster than the equal torque distribution, reducing stopping distance to approximately 39 meters from 42.

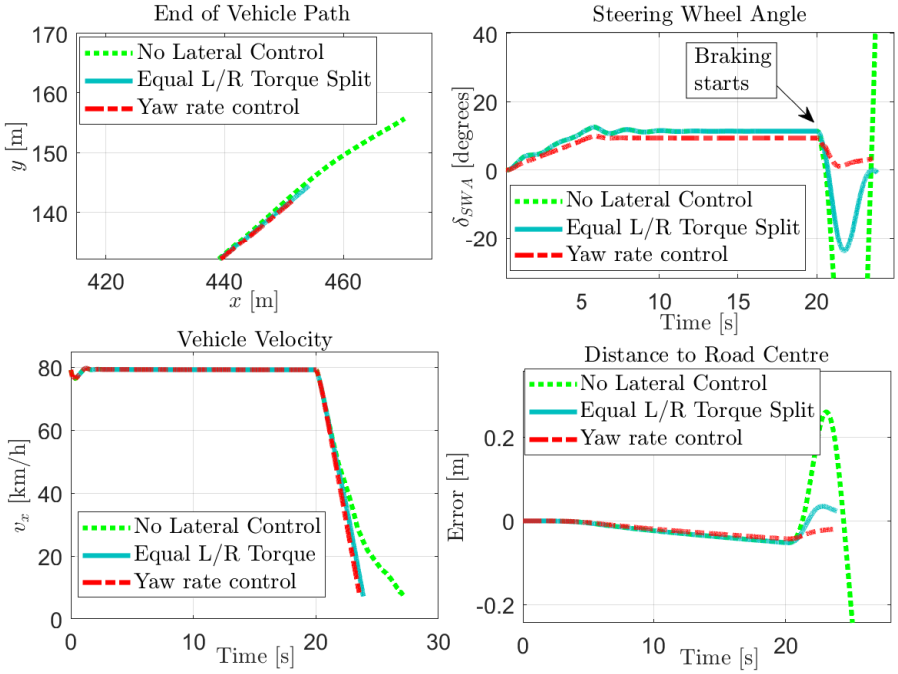

Figure 6.14: Performance measurements for hard braking test in curve. Green represents only using friction and actuator limits without yaw moment control, turquoise represents a forced equal torque distribution between the left and right side, and red represents the active MPC controller.

In terms of motion coordinator aggressiveness, the needed torque difference between left and right to enhance the performance was very low, which can be seen in Figure

6.15. Note that while there was a difference between the left and right actuators, it did not significantly affect the total power consumption.

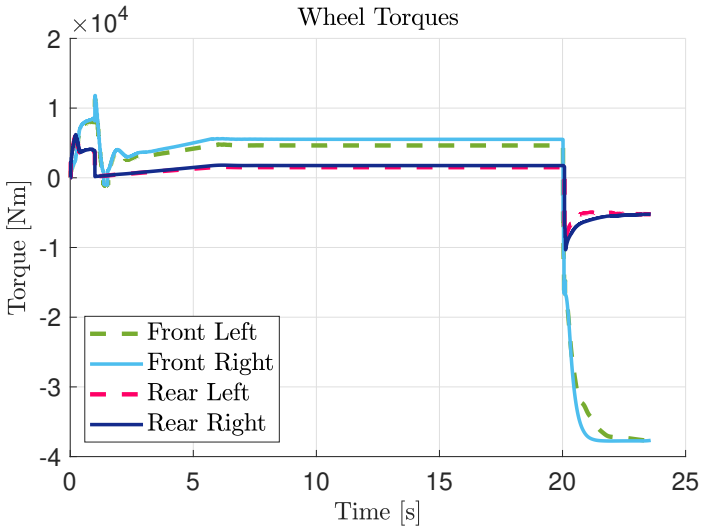

Figure 6.15: Torque usage when braking with MPC active. The motion coordinator moment request can be seen on the left/right torque difference.

6.8 Reducing mode switch impact

While switching from cruise mode to power mode is usually a result of a driver request, it may activate at times where the driver does not expect it. This could be due to a slight incline during, or after a slight acceleration on a highway, where the power requirement is too high for the cruise motors. A test was done with switching at high longitudinal acceleration and the result can be found in Figure 6.16. Here, it can be seen that while the MPC did help in mitigating the oscillations after the switch, it failed to completely eliminate the difference in vehicle behaviour. The reason for this is that the vehicle dynamics change depending on the propulsion mode and the updated parameters were not accounted for in the MPC. It could be worthwhile to investigate a different set of parameters for the MPC depending on the current mode the vehicle is in. The difference in steering wheel angle however, was very low, both with and without the motion coordinator. The play in the steering wheel is slightly below 10 degrees, and the difference between the two modes on the active control graphs were significantly lower than this. It is likely that the driver would not notice this mode switch.

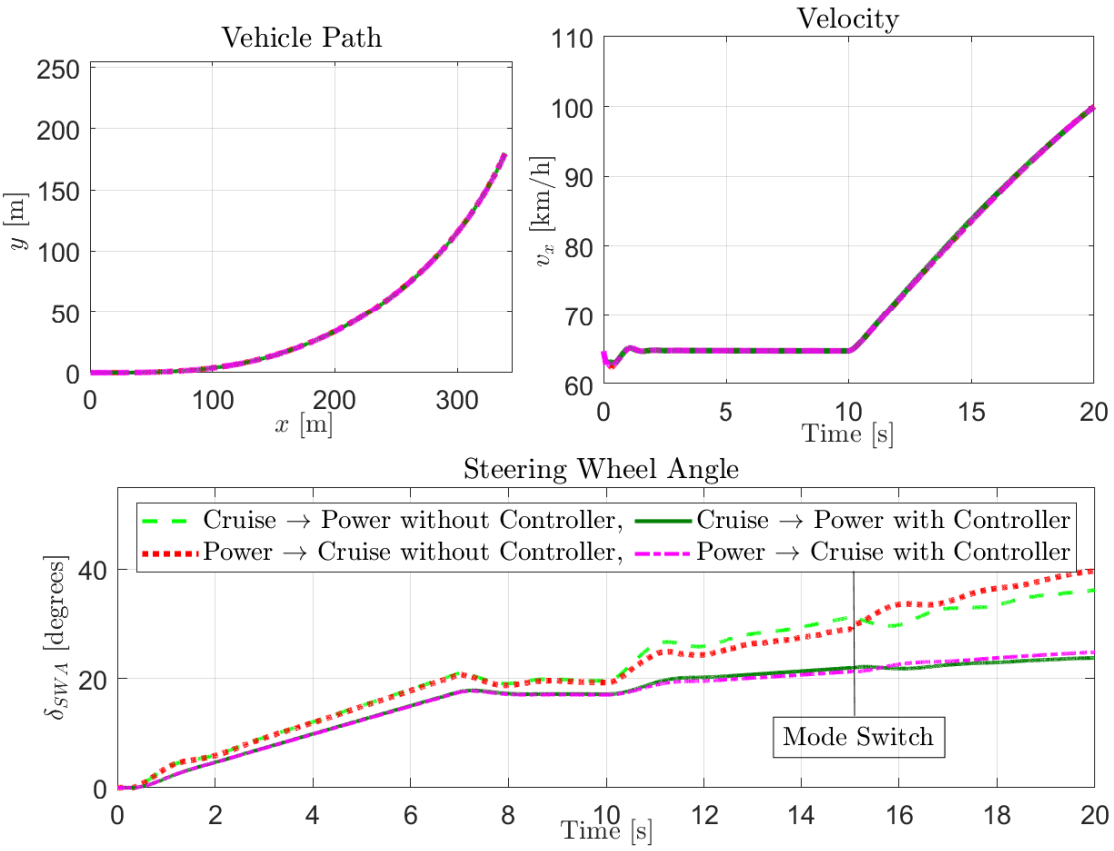

Figure 6.16: High speed switch, during longitudinal acceleration, between cruise mode and power mode, with and without lateral motion coordination. Mode switch takes place a at t = 15 seconds.

A second test was also done, this time with higher lateral acceleration, and the re-

sults of this test can be found in Figure 6.17. Here, it can be seen that the timing of the switch either dampened the oscillations of the vehicle (Power Mode -> Cruise Mode, red) or accentuated the oscillations (Cruise Mode -> Power Mode, green), making the driver further lose control. In this case, the difference between the two modes was up to 30 degrees on the steering wheel angle, which could be problematic for the driver. The MPC performed similarly to the first test. However, this time the improvement from not using the lateral motion coordinator was noticeably different. The MPC was able to stabilise the vehicle before the switch, reducing the impact. The difference in steering wheel angle before and after the switch was hence less than 10 degrees, which is deemed acceptable.

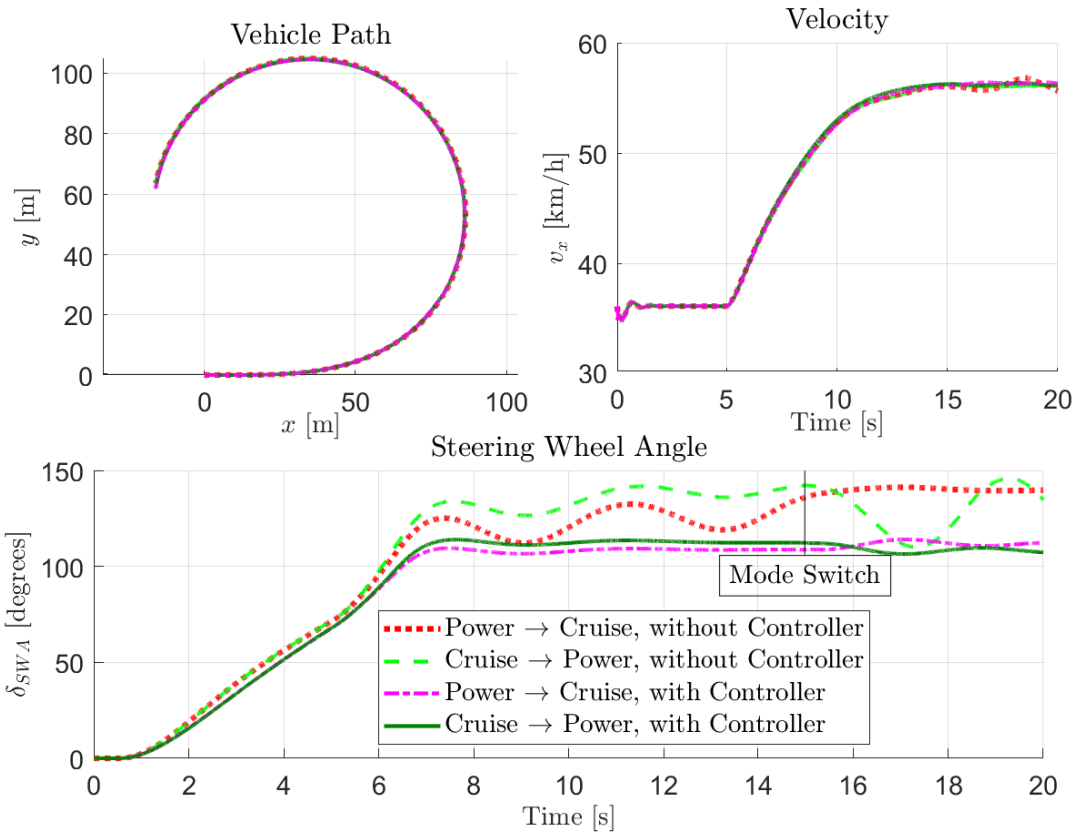

Figure 6.17: Mode switch at the limit of lateral acceleration. The vehicle mode switch happened at t = 15 seconds.

6.9 Rollover Prevention Constraint

The rollover prevention test was done with a tractor only, and the goal was not to completely prevent rollover, but to prove that the MPC was able to keep the lateral acceleration and yaw rate within an acceptable limit (and hence avoid risking rollover), even when a positive acceleration was requested.

The test below started with the vehicle already in a steady state corner. An accel-

eration request was set at t = 10 s.

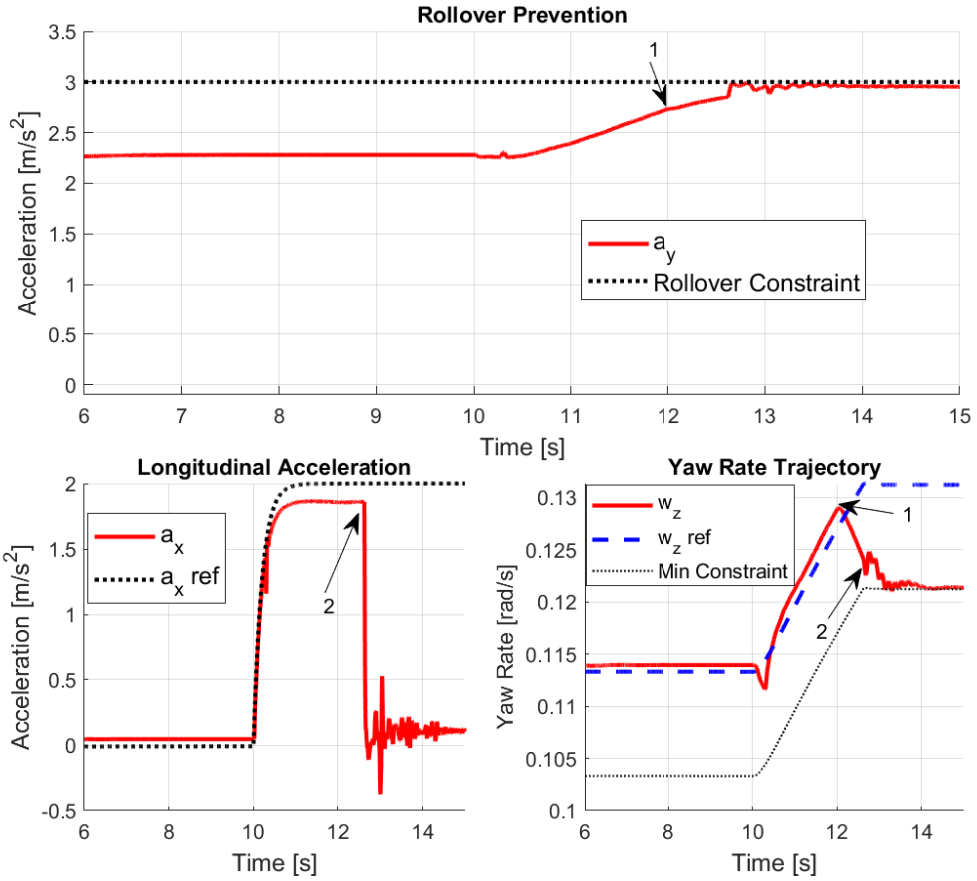

Figure 6.18: Rollover test at 70 km/h. A 2 m/s^2 longitudinal acceleration was requested at 10 seconds. The steering wheel angle was a constant 27 degrees throughout the entire test, and there was no driver.

Two notable timestamps can be extracted:

1. The MPC expected the lateral acceleration to exit the acceptable range within the time horizon. Yaw rate was sacrificed to keep the rollover constraint valid.
2. The MPC expected the yaw rate to exit the minimum acceptable limit within the horizon. Acceleration was sacrificed to ensure that the yaw rate was kept within an acceptable range.

Oscillations occurred when multiple targets were close to a constraint. This was likely due to the fact that vehicle velocity was assumed constant across the horizon. The MPC did not fully understand the dynamics of how vehicle velocity affected yaw rate and lateral acceleration. It was successful for a test without a driver, but may prove unstable when more volatile inputs are given to the motion coordinator. Further development is needed.

6.10 Acceleration in Curve

The performance result is shown in Figure 6.19 and the general trend was that the relaxed request style v_{des} performed worse than the forced request style v_{req}, but only slightly. Looking at the graph with steering wheel angle, it can be seen that the driver clearly had to compensate once the acceleration started at 6 seconds when no lateral motion coordination was present. Both the v_{req} and the v_{des} coordinator styles showed a more muted steering angle. There was still steering compensation required from the driver, but there was a clear improvement. When looking at the total power use of the two styles (as a percentage of the power use by pure power loss minimisation, i.e. no lateral control), it was clear what the relaxed style was intended for. The improvement from the forced request style to the relaxed request style was substantial, where the v_{req} request consumed more power than using no lateral control, finishing at 100.1% of power consumption in comparison to no lateral coordination. The relaxed request style instead reduced power use slightly compared to no lateral coordination, while keeping the benefits of torque vectoring. The v_{des} request style finished the curve at 99.8% of power use.

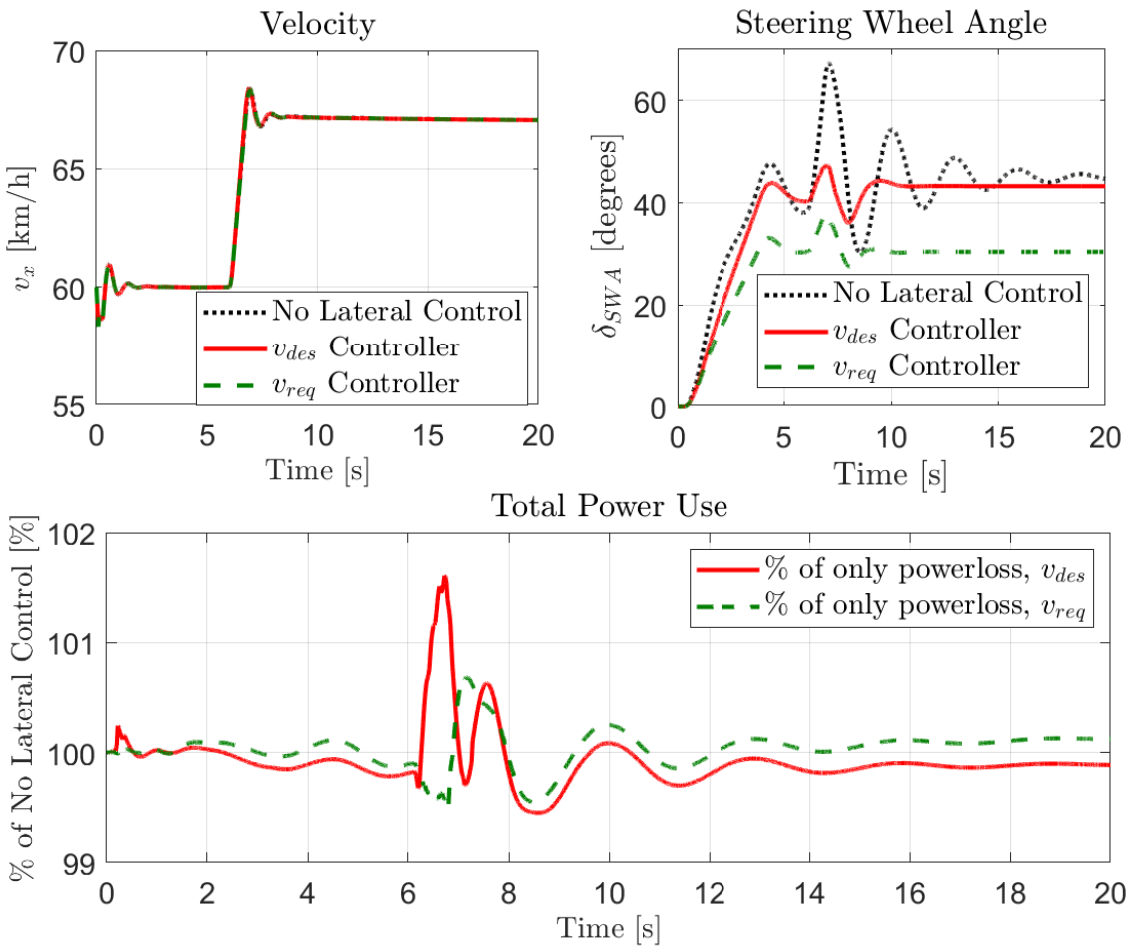

Figure 6.19: Comparison between only using power loss, using a relaxed torque vectoring output and a forced torque vectoring output.

6.11 Short Haul Power Use Simulation

The observed results from the short haul drive scenario can be seen in Figure 6.20. Here, it can be seen that the forced request style (v_{req}) helped the driver in keeping a slightly closer distance to the centre line of the road, compared to relaxed requests. The impact of this however, can be seen in the power usage. Here, it is clear that the high engagement of the forced request style caused it to consume much more energy. When the driver did not expect or want interference by the motion coordinator, the performance of v_{req} was worse than no lateral control at all. v_{des} solved this problem, and had similar performance to no lateral control when not in use. If an emergency situation were to happen, the limits v_{min} and v_{max} within the vector v_{des} would converge, forcing the control allocator to focus on performance, rather than power loss minimisation.

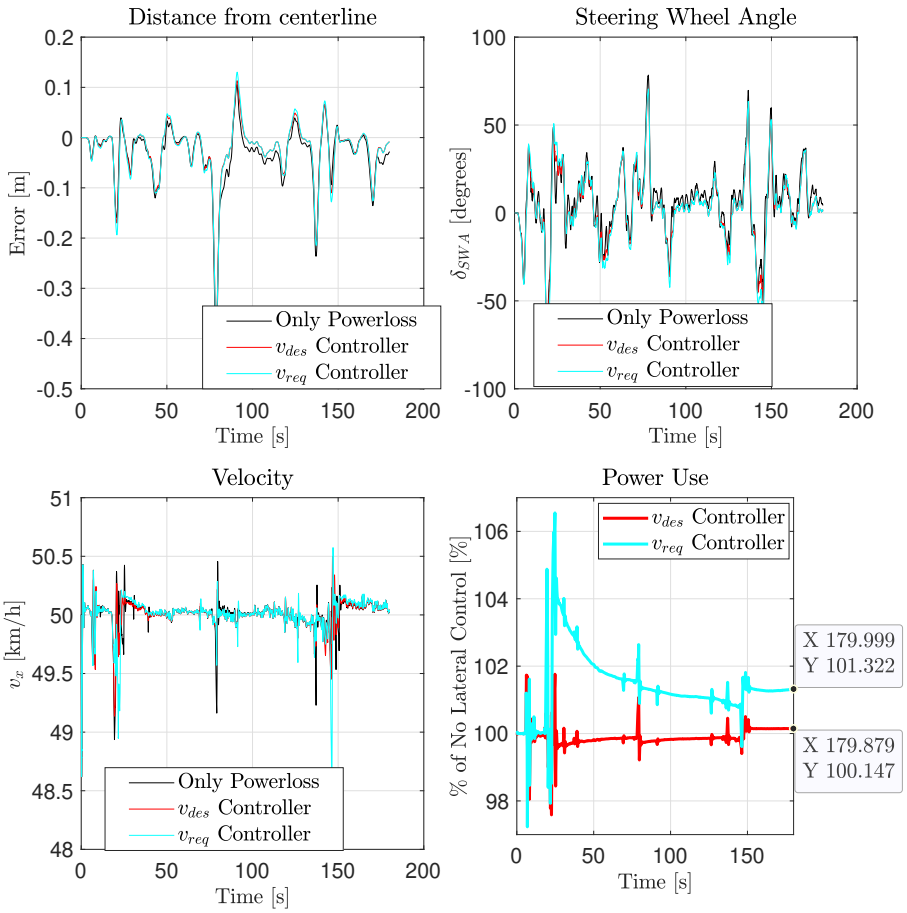

Figure 6.20: Comparison between using power loss without lateral control, with lateral control and with relaxed lateral control on a road between Hällered and Alingsås during normal driving conditions.

To illustrate the effectiveness of a v_{des} style in an emergency case, a hard braking scenario was introduced to the road between Hällered and Alingsås. The goal of the test was to identify how the active yaw rate MPC handled braking in the middle of

a normal driving scenario, and also to look at the impact on its power usage. The graph in Figure 6.21 is an enhanced plot of the times between 45 and 65 seconds for this braking test. The timestamps before this was the same as the previous test.

It can be seen that there was a significant decrease in steering compensation needed from the driver while the MPC was active. Without any lateral control, the steering wheel angle varied with around 55°, compared with 18° for the lateral control. As the driver had trouble keeping the vehicle straight when braking without the lateral motion coordinator, the braking distance was also increased, and the braking time was about 800 milliseconds longer without yaw rate control. Looking at the power consumption in this test showed a clear increase compared to not using any lateral control. This was deemed acceptable as an emergency situation is focused on driver safety and not energy efficiency. The centre line error in the top left graph was less than 5 cm in all control scenarios and could safely be ignored. Figure 6.22 illustrates how often the new v_{des} limits need to intervene with power loss optimisation.

The average value of the constraint violation boolean is 0.13, indicating that the MPC intervened approximately 13% of the time. Power loss still has ability to optimise slightly even when the MPC is active, similar to how the previous request style v_{req} operates, but a non violated constraint means larger freedom is given to the power loss minimisation laterally.

After braking was initialised at 58 seconds, the boolean was generally high, which implies that the MPC was active most of the time. At 59-60 seconds it was constantly active. This was expected and the wanted result, as it implies that the MPC intervenes as intended in an emergency.

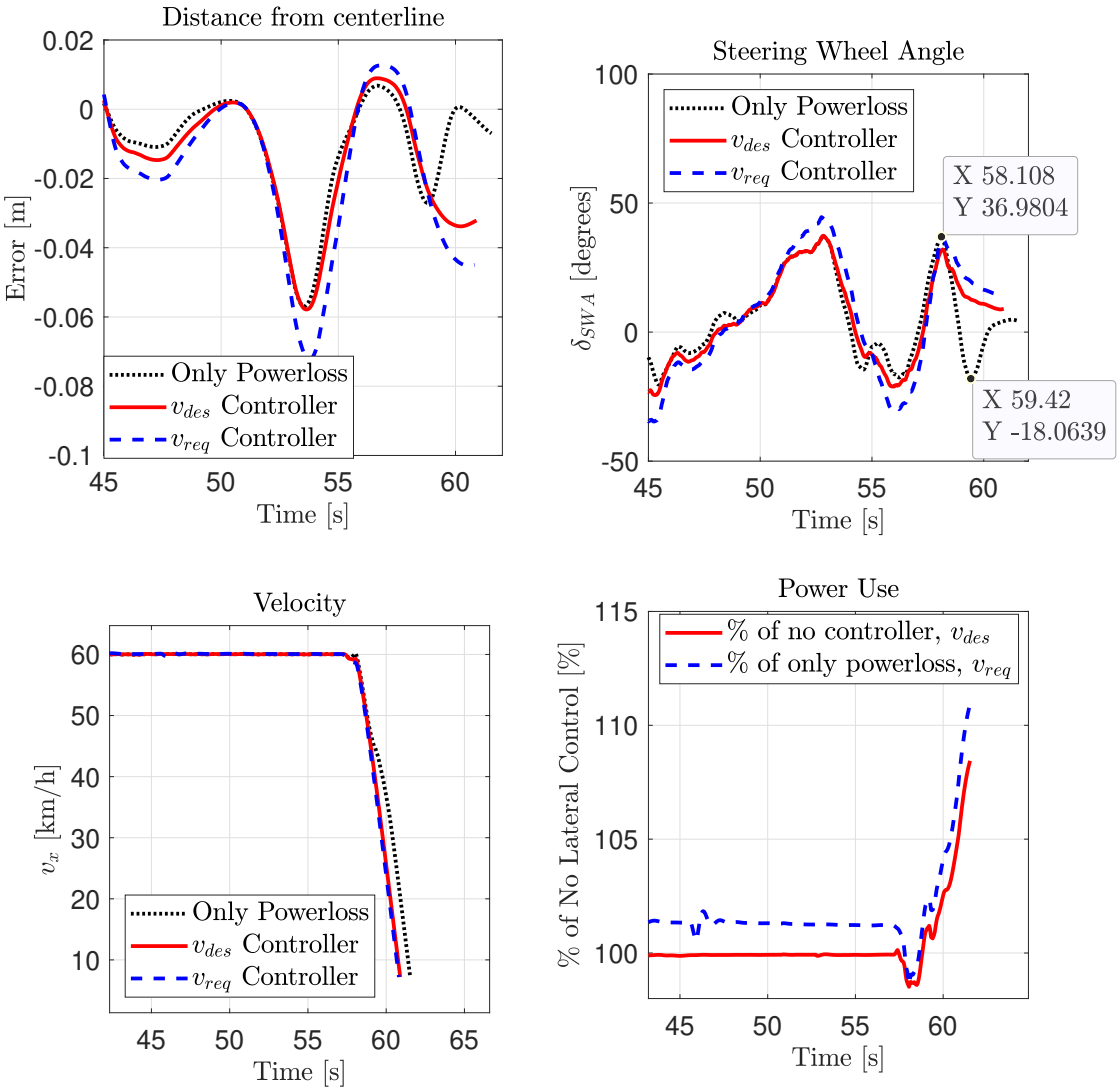

Figure 6.21: Longitudinal control versus lateral control with forced yaw moment versus relaxed controller on Hällered - Alingsås.

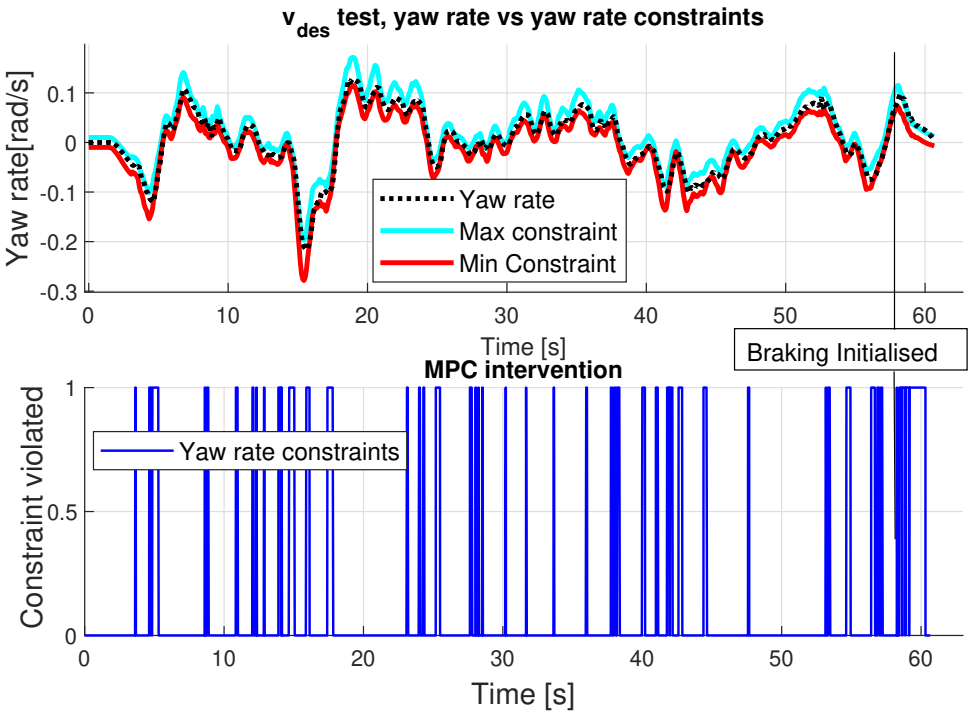

Figure 6.22: Vehicle yaw rate compared to the constraints set by the relaxed request style. If the boolean is zero, the power loss is able to operate freely.

7
Conclusion

Recalling the research questions from the motivation and purpose, the goal of the thesis is to analyse the impact of torque vectoring on lateral performance of a heavy electric vehicle, through the specific questions:

- When can torque vectoring reasonably improve lateral performance of heavy electric vehicles?
- What control strategies are favourable when using torque vectoring for heavy vehicles?
- How can torque vectoring improve the predictability of the vehicle?
- How does a mode switch between axles affect the vehicle behaviour and is torque vectoring able to mitigate the change?
- What is the impact of torque vectoring on power consumption?

A performance analysis has been done on mitigating change over different road surfaces, different propulsion configurations, emergency braking in curves, safe stopping on edge conditions and reducing steering consumption when driving with promising results.

In terms of raw impact, the moment generated from the torque vectoring system was enough to significantly alter the vehicle characteristics, changing the vehicle from understeered to oversteered or vice versa on demand. An analysis of controller performance and benefits was done, with the conclusion that an MPC is the best choice for a motion coordinator, due to the ability to set constraints and adapt before a limit is reached.

Analysing goal states through literature analysis and interviews, the main goals for a torque vectoring system aiming to improve predictability was three things:

- Reduce steering compensation
- Mitigate mode changes, such as start axle startup
- Reduce the difference in vehicle behaviour for different road conditions

As the steering angle is not directly controlled by the torque vectoring system, the steady state yaw rate was chosen as the motion coordinator target. A perfect controller would then result in minimal compensation and behaviour change during mode switching.

In simulation tests, an MPC based controller showed a significant reduction in steering compensation in all scenarios. When emergency braking and braking on ice, the driver slowly reduced the steering wheel angle with the controller active, as opposed to the active prevention needed without lateral control. The MPC also proved very robust to noise variations.

When analysing mode changes, the change in dynamics without a yaw rate controller was not deemed significant outside of extreme scenarios, but the yaw rate controller still improved the handling of the vehicle during the switch from front wheel drive to all wheel drive.

A secondary force request style was made for regular use to reduce the aggressiveness of the motion coordinator outside of extreme scenarios. When analysing power usage, the conclusion was that regular lateral control increased the power consumption by approximately 1.3%, while the relaxed request either did not increase or only increased the power use by 0.1%.

Bibliography

[1] European Commission, "Fit for 55: Eu reaches new milestone to make all new cars and vans zero-emission from 2035," 2023. [online]. Available: https://climate.ec.europa.eu/news-your-voice/news/fit-55-eu-reaches-new-milestone-make-all-new-cars-and-vans-zero-emission-2035-2023-03-28_en (accessed: 2023-03-29).

[2] I. C. Borbujo, P. G. Pereirinha, M. G. Vega, J. A. del Valle, and J. C. Á. Antón, "Heavy duty transport descarbonization: legislation and standards for hydrogen and battery electric buses and heavy-duty trucks," in *2021 IEEE Vehicle Power and Propulsion Conference (VPPC)*, pp. 1–6, IEEE, 2021.

[3] European Commission, "European green deal: Commission proposes 2030 zero-emissions target for new city buses and 90 percent emissions reductions for new trucks by 2040," 2023. [online]. Available: https://ec.europa.eu/commission/presscorner/detail/en/ip_23_762 (accessed: 2023-05-16).

[4] Y. Ushiroda, K. Sawase, N. Takahashi, K. Suzuki, and K. Manabe, "Development of super ayc," *Technical review*, vol. 15, pp. 73–6, 2003.

[5] B. Berk, "The future of off-road is electric.," *Popular Mechanics*, vol. 197, no. 3, pp. 40–44, 2020.

[6] "Polestar 3 performance features." `https://www.polestar.com/uk/polestar-3/performance/`, accessed 2023-01-19.

[7] S. Janardhanan, L. Laine, M. Jonasson, B. Jacobson, and M. Alakü la, "Concept design of electric cruise and startability axles for long haul heavy vehicles to maximise driving range," in *2021 IEEE Vehicle Power and Propulsion Conference (VPPC)*, pp. 1–8, 2021.

[8] B. Jacobson *et al.*, "Vehicle dynamics," *Chalmers University of Technology*, 2016.

[9] G. S. Vorotović, B. B. Rakicević, S. R. Mitić, and D. D. Stamenković, "Determination of cornering stiffness through integration of a mathematical model and real vehicle exploitation parameters," *FME Transactions*, vol. 41, no. 1, pp. 66–71, 2013.

[10] G. De Filippis, B. Lenzo, A. Sorniotti, P. Gruber, and W. De Nijs, "Energy-efficient torque-vectoring control of electric vehicles with multiple drivetrains," *IEEE Transactions on Vehicular Technology*, vol. 67, no. 6, pp. 4702–4715, 2018.

[11] A. Parra, D. Tavernini, P. Gruber, A. Sorniotti, A. Zubizarreta, and J. Pérez, "On nonlinear model predictive control for energy-efficient torque-vectoring," *IEEE Transactions on Vehicular Technology*, vol. 70, no. 1, pp. 173–188, 2020.

[12] W. Liu, A. Khajepour, H. He, H. Wang, and Y. Huang, "Integrated torque vectoring control for a three-axle electric bus based on holistic cornering control method," *IEEE Transactions on Vehicular Technology*, vol. 67, no. 4, pp. 2921–2933, 2017.

[13] B. Zhao, N. Xu, H. Chen, K. Guo, and Y. Huang, "Stability control of electric vehicles with in-wheel motors by considering tire slip energy," *Mechanical Systems and Signal Processing*, vol. 118, pp. 340–359, 2019.

[14] K. Sawase, Y. Ushiroda, and T. Miura, "Left-right torque vectoring technology as the core of super all wheel control (s-awc)," *Mitsubishi Motors Technical Review*, vol. 18, pp. 16–23, 2006.

[15] V. De Pascale, B. Lenzo, F. Farroni, F. Timpone, and X. Zhang, "Torque vectoring control for fully electric sae cars," in *Proceedings of XXIV AIMETA Conference 2019 24*, pp. 1075–1083, Springer, 2020.

[16] J. Kang, H. Heo, *et al.*, "Control allocation based optimal torque vectoring for 4wd electric vehicle," tech. rep., SAE Technical Paper, 2012.

[17] L. Pugi, T. Favilli, L. Berzi, E. Locorotondo, and M. Pierini, "Brake blending and torque vectoring of road electric vehicles: a flexible approach based on smart torque allocation," *International Journal of Electric and Hybrid Vehicles*, vol. 12, no. 2, pp. 87–115, 2020.

[18] D. Kasinathan, A. Kasaiezadeh, A. Wong, A. Khajepour, S.-K. Chen, and B. Litkouhi, "An optimal torque vectoring control for vehicle applications via real-time constraints," *IEEE Transactions on Vehicular Technology*, vol. 65, no. 6, pp. 4368–4378, 2015.

[19] G. Pellegrino, A. Vagati, B. Boazzo, and P. Guglielmi, "Comparison of induction and pm synchronous motor drives for ev application including design examples," *IEEE Transactions on industry applications*, vol. 48, no. 6, pp. 2322–2332, 2012.

[20] A. Koch, O. Teichert, S. Kalt, A. Ongel, and M. Lienkamp, "Powertrain optimization for electric buses under optimal energy-efficient driving," *Energies*, vol. 13, no. 23, p. 6451, 2020.

[21] S. Janardhanan, L. Laine, M. Jonasson, B. Jacobson, and E. Gelso, "Motion control and power coordination of electric propulsion and braking distributed on multiple axles on heavy vehicles," in *2022 IEEE Vehicle Power and Propulsion Conference (VPPC)*, pp. 1–8, IEEE, 2022.

[22] S. Janardhanan, "Powerlossmin-em-and-brakes." `https://github.com/sachinj486/Powerlossmin-EM-and-brakes#power-loss-minimisation-of-electric-machines-and-friction-brakes`, 2023.

[23] L. Laine, *Reconfigurable motion control systems for over-actuated road vehicles.* Chalmers University of Technology Göteborg, Sweden, 2007.

[24] M. Rothhämel, *Characterisation and Utilisation of Steering Feel in Heavy Trucks.* PhD thesis, KTH, Vehicle Dynamics, 2013. QC 20130524.

[25] "Intelligent transport systems – Adaptive cruise control systems – Performance requirements and test procedures," standard, International Organization for Standardization, Geneva, CH, Sept. 2018.

[26] K. N. de Winkel, T. Irmak, R. Happee, and B. Shyrokau, "Standards for passenger comfort in automated vehicles: Acceleration and jerk," *Applied Ergonomics*, vol. 106, p. 103881, 2023.

[27] A. Scamarcio, P. Gruber, S. De Pinto, and A. Sorniotti, "Anti-jerk controllers for automotive applications: A review," *Annual Reviews in Control*, vol. 50, pp. 174–189, 2020.

[28] J. Orus, J. Theunissen, R. Meneses, and J.-M. Rodriguez-Fortun, "Active vibration control for torsional oscillations in powertrains for fully electric vehicles," in *FISITA World Automotive Congress, Maastricht, the Netherlands*, 2014.

[29] M. Mattsson and R. Mehler, "Optimal model predictive acceleration controller for a combustion engine and friction brake actuated vehicle," *IFAC-PapersOnLine*, vol. 49, no. 11, pp. 511–518, 2016.

[30] A. K. Nandi, D. Chakraborty, and W. Vaz, "Design of a comfortable optimal driving strategy for electric vehicles using multi-objective optimization," *Journal of Power Sources*, vol. 283, pp. 1–18, 2015.

[31] C. Hatipoglu, U. Ozguner, and K. Redmill, "Automated lane change controller design," *IEEE Transactions on Intelligent Transportation Systems*, vol. 4, no. 1, pp. 13–22, 2003.

[32] A. Seiler, S. Willebrand, M. Olsson, and H. Wahlman, "Viltolyckskartor: Teknisk beskrivning för datahantering och produktion," 2019.

[33] M. B. Andersen, "Psychosocial factors and changes in peripheral vision, muscle tension, and fine motor skills during stress.," 1988.

[34] L. Kerautret, S. Dabic, and J. Navarro, "Exploration of driver stress when resuming control from highly automated driving in an emergency situation," *Transportation research part F: traffic psychology and behaviour*, vol. 93, pp. 222–234, 2023.

[35] G. Morrison and D. Cebon, "Combined emergency braking and turning of articulated heavy vehicles," *Vehicle system dynamics*, vol. 55, no. 5, pp. 725–749, 2017.

[36] H. Lv and S. Liu, "Closed-loop handling stability of 4ws vehicle with yaw rate control," *Strojniški vestnik-Journal of Mechanical Engineering*, vol. 59, no. 10, pp. 595–603, 2013.

[37] S. D. Fahlgren. E, "Torque vectoring using eaxle configuration for 4wd battery electric truck utilizing control allocation for motion control and steer by propulsion," *Master Thesis, Chalmers University of Technology*, June 2022.

[38] J. Kim and H. Kim, "Electric vehicle yaw rate control using independent in-wheel motor," in *2007 Power Conversion Conference - Nagoya*, pp. 705–710, 2007.

[39] A. Lucchini, S. Formentin, M. Corno, D. Piga, and S. M. Savaresi, "Torque vectoring for high-performance electric vehicles: an efficient mpc calibration," *IEEE Control Systems Letters*, vol. 4, no. 3, pp. 725–730, 2020.

[40] J. P. Switkes, E. J. Rossetter, I. A. Coe, and J. C. Gerdes, "Handwheel force feedback for lanekeeping assistance: Combined dynamics and stability," 2006.

[41] C. B. Winkler, "Simplified analysis of the steady-state turning of complex vehicles," *Vehicle system dynamics*, vol. 29, no. 3, pp. 141–180, 1998.

A

Inequality matrices

In this appendix, the inequality constraints will be explained.

The lengths used are N as the length of the horizon, n as the amount of states in the model, and m as the amount of inputs. The matrix A_{in} is split into three matrices, referred to as F, G and Barrier. These affect the states, input and slack variable respectively.

$$A_{in}\mathbf{z} \leq b_{in} \tag{A.1}$$

$$\begin{bmatrix} F & | & G & | & Barrier \end{bmatrix} \begin{bmatrix} \mathbf{e} \\ \hline \mathbf{u} \\ \hline \mathbf{s} \end{bmatrix} \leq b_{in} \tag{A.2}$$

To begin constructing the matrices A_{in} and b_{in}, $b_{in_{friction}}$ is the maximum longitudinal force allowed on each tyre in each time instance. The first half is the maximum longitudinal force and the second half is the minimum(maximum negative) longitudinal force. When constructing the matrices, it is important to negate the minimum values, as it allows the inequality constraint logic to work properly:

$$u \geq u_{min} \implies -u \leq -u_{min} \tag{A.3}$$

$$b_{in_{friction}} = \begin{bmatrix} F_{Friction_{max}}[FR][0] \\ \vdots \\ F_{Friction_{max}}[RR][0] \\ \vdots \\ F_{Friction_{max}}[FR][N] \\ \vdots \\ F_{Friction_{max}}[RR][N] \\ -F_{Friction_{min}}[FR][0] \\ \vdots \\ -F_{Friction_{min}}[RR][0] \\ \vdots \\ -F_{Friction_{min}}[FR][N] \\ \vdots \\ -F_{Friction_{min}}[RR][N] \end{bmatrix} \tag{A.4}$$

$b_{in_{actuator}}$ is the maximum longitudinal actuator torque(hard motor limits). The first half only includes the motors, while the second half(maximum negative torque) also includes the brakes.

$$b_{in_{actuator}} = \begin{bmatrix} F_{motor_{max}}[FR][0] \\ \vdots \\ F_{motor_{max}}[RR][0] \\ \vdots \\ F_{motor_{max}}[FR][N] \\ \vdots \\ F_{motor_{max}}[RR][N] \\ -(F_{motor_{min}}[FR][0] + F_{brake_{min}}[FR][0]) \\ \vdots \\ -(F_{motor_{min}}[RR][0] + F_{brake_{min}}[RR][0]) \\ \vdots \\ -(F_{motor_{min}}[FR][N] + F_{brake_{min}}[FR][N]) \\ \vdots \\ -(F_{motor_{min}}[RR][N] + F_{brake_{min}}[RR][N]) \end{bmatrix} \tag{A.5}$$

As both $b_{in_{actuator}}$ and $b_{in_{friction}}$ set a maximum positive and negative force on the wheels, they can be combined into u_{min} and u_{max}.

Algorithm 2 Calculate actuator limits

$u_{min} = \max(b_{in_{actuator}}[1{:}\text{length}/2], b_{in_{friction}}[1{:}\text{length}/2])$
$u_{max} = \min(b_{in_{actuator}}[\text{length}/2{+}1{:}\text{end}], b_{in_{friction}}[\text{length}/2{+}1{:}\text{end}])$

The A_{in} part of u_{max} and u_{min} will thus be $2m \cdot N$ long, and $N(n+m+1)$ wide. Only the control inputs matter, and only one at a time, so the rest are set to zero matrices of appropriate size.

$$F_{u_{max}} = \begin{bmatrix} 0 & \cdots & 0 \\ \vdots & \ddots & \vdots \\ 0 & \cdots & 0 \end{bmatrix}, \; G_{u_{max}} = \begin{bmatrix} 1 & \cdots & 0 \\ \vdots & \ddots & \vdots \\ 0 & \cdots & 1 \end{bmatrix}, \; Barrier_{u_{max}} = \begin{bmatrix} 0 & \cdots & 0 \\ \vdots & \ddots & \vdots \\ 0 & \cdots & 0 \end{bmatrix} \tag{A.6}$$

$$A_{u_{max}} = \begin{bmatrix} F_{u_{max}} & G_{u_{max}} & Barrier_{u_{max}} \end{bmatrix} \tag{A.7}$$

Similarly, for the minimum, only that the negative value of the control has to be taken to allow the inequality logic to function:

$$F_{u_{min}} = \begin{bmatrix} 0 & \cdots & 0 \\ \vdots & \ddots & \vdots \\ 0 & \cdots & 0 \end{bmatrix}, \; G_{u_{min}} = \begin{bmatrix} -1 & \cdots & 0 \\ \vdots & \ddots & \vdots \\ 0 & \cdots & -1 \end{bmatrix}, \; Barrier_{u_{min}} = \begin{bmatrix} 0 & \cdots & 0 \\ \vdots & \ddots & \vdots \\ 0 & \cdots & 0 \end{bmatrix} \tag{A.8}$$

$$A_{u_{min}} = \begin{bmatrix} F_{u_{min}} & G_{u_{min}} & Barrier_{u_{min}} \end{bmatrix} \tag{A.9}$$

e_{max} is the maximum allowed error for the states. Note that for the v_{des} controllers, the reference points will be different, and the actual values for these constraints will be different. This is what allows the two controllers to cross eachother, as seen in figure 6.9. The minimum value is the maximum negative error, not the smallest error. In the thesis, the main constraint that was active was the yaw rate, where the two controllers would not allow the error to be larger than the difference between the two reference yaw rates, essentially forcing the yaw rate to stay within the band created.

$$x_{max} = \begin{bmatrix} e_{max} \begin{bmatrix} \dot{v_x} \\ v_x \\ \omega \\ \beta \end{bmatrix} [0] \\ \vdots \\ e_{max} \begin{bmatrix} \dot{v_x} \\ v_x \\ \omega \\ \beta \end{bmatrix} [N] \end{bmatrix} \tag{A.10}$$

$$x_{min} = - \begin{bmatrix} e_{min} \begin{bmatrix} \dot{v_x} \\ v_x \\ \omega \\ \beta \end{bmatrix} [0] \\ \vdots \\ e_{min} \begin{bmatrix} \dot{v_x} \\ v_x \\ \omega \\ \beta \end{bmatrix} [N] \end{bmatrix} \tag{A.11}$$

The $A_{x_{max}}$ and $A_{x_{min}}$ are constructed the same way as before, except the states are now nonzero and the inputs are set to zero. The main difference is the inclusion of the slack variable. As a single equation:

$$x[k] - s[k] \leq x_{max} \tag{A.12}$$

Depending on how many states need a slack variable for robustness a different amount of slack variables have to be added. In this thesis, only the yaw rate had a

slack constraint, which meant that only $1 \cdot N$ was needed.

$$F_{x_{max}} = \begin{bmatrix} 1 & \cdots & 0 \\ \vdots & \ddots & \vdots \\ 0 & \cdots & 1 \end{bmatrix},\ G_{x_{max}} = \begin{bmatrix} 0 & \cdots & 0 \\ \vdots & \ddots & \vdots \\ 0 & \cdots & 0 \end{bmatrix},\ Barrier_{x_{max}} = \begin{bmatrix} \begin{bmatrix} 0 \\ 0 \\ -1 \\ 0 \end{bmatrix} & \cdots & 0 \\ \vdots & \ddots & \vdots \\ 0 & \cdots & \begin{bmatrix} 0 \\ 0 \\ -1 \\ 0 \end{bmatrix} \end{bmatrix} \tag{A.13}$$

$$A_{x_{max}} = \begin{bmatrix} F_{x_{max}} & G_{x_{max}} & Barrier_{x_{max}} \end{bmatrix} \tag{A.14}$$

And similarly:

$$F_{x_{min}} = \begin{bmatrix} -1 & \cdots & 0 \\ \vdots & \ddots & \vdots \\ 0 & \cdots & -1 \end{bmatrix},\ G_{x_{min}} = \begin{bmatrix} 0 & \cdots & 0 \\ \vdots & \ddots & \vdots \\ 0 & \cdots & 0 \end{bmatrix},\ Barrier_{x_{min}} = \begin{bmatrix} \begin{bmatrix} 0 \\ 0 \\ 1 \\ 0 \end{bmatrix} & \cdots & 0 \\ \vdots & \ddots & \vdots \\ 0 & \cdots & \begin{bmatrix} 0 \\ 0 \\ 1 \\ 0 \end{bmatrix} \end{bmatrix} \tag{A.15}$$

$$A_{x_{min}} = \begin{bmatrix} F_{x_{min}} & G_{x_{min}} & Barrier_{x_{min}} \end{bmatrix} \tag{A.16}$$

For the lateral acceleration rollover constraint, it is assumed that the vehicle has a low body slip, so that the lateral velocity is low.

$$a_y \approx v_x \omega_z \tag{A.17}$$

The lateral acceleration can then be modelled as an inequality constraint, using equation 2.33.

$$\underbrace{e_{\omega_z} v_{x0}}_{A_{in,roll}} \leq \underbrace{g\frac{t_f + t_r}{4h} - w_{z,ref} v_{x0}}_{b_{in,roll}} \tag{A.18}$$

The left side of the equation fits into a diagonal F matrix with size $N \times n \cdot N$, and the G and Barrier matrices would be zero of $N \times m \cdot N$ and $N \times N$ size.
The actuator rate of change constraints are slightly more complicated as they depend on the previous state and take up more processing power. As the motor dynamics are very fast in a BEV, they have mostly been left off in the tests to allow faster

calculations. The minimum is once again the maximum negative change. For one step, the rate of change can be formulated as an inequality constraint as:

$$u[k+1] - u[k] \leq Ts_{MPC_{step}} \Delta T_{max_{wheel}} \tag{A.19}$$

The right side equation is used in the b matrix.

$$\Delta u_{max} = \begin{bmatrix} Ts_{MPC_{step}} \begin{bmatrix} \Delta T_{max_{FR}} \\ \vdots \\ \Delta T_{max_{RR}} \end{bmatrix} [0] \\ \vdots \\ Ts_{MPC_{step}} \begin{bmatrix} \Delta T_{max_{FR}} \\ \vdots \\ \Delta T_{max_{RR}} \end{bmatrix} [N] \end{bmatrix} \tag{A.20}$$

$$\Delta u_{min} = - \begin{bmatrix} Ts_{MPC_{step}} \begin{bmatrix} \Delta T_{min_{FR}} \\ \vdots \\ \Delta T_{min_{RR}} \end{bmatrix} [0] \\ \vdots \\ Ts_{MPC_{step}} \begin{bmatrix} \Delta T_{min_{FR}} \\ \vdots \\ \Delta T_{min_{RR}} \end{bmatrix} [N] \end{bmatrix} \tag{A.21}$$

Using equation A.19, the F and Barrier matrices are clearly zero again, but careful construction of the $G_{\Delta_{umax}}$ is needed.

$$F_{\Delta u_{max}} = \begin{bmatrix} 0 & \cdots & 0 \\ \vdots & \ddots & \vdots \\ 0 & \cdots & 0 \end{bmatrix}, \; G_{\Delta u_{max}} = \begin{bmatrix} -1 & 1 & 0 & \cdots & 0 \\ 0 & -1 & 1 & \ddots & 0 \\ \vdots & \ddots & \ddots & \ddots & \vdots \\ \vdots & \cdots & 0 & -1 & 1 \\ 0 & \cdots & \cdots & 0 & -1(0) \end{bmatrix}, \; Barrier_{\Delta u_{max}} = \begin{bmatrix} 0 & \cdots & 0 \\ \vdots & \ddots & \vdots \\ 0 & \cdots & 0 \end{bmatrix} \tag{A.22}$$

The last entry of $G_{\Delta u_{max}}$ is set to zero as there is no next state to compare to. However, it is far forward in time, so it is deemed negligible. $F_{\Delta u_{min}}$, $G_{\Delta u_{min}}$ and $Barrier_{\Delta_{umin}}$ are once again the maximum matrices multiplied by -1.

$$A_{\Delta u_{max}} = \begin{bmatrix} F_{\Delta u_{max}} & G_{\Delta u_{max}} & Barrier_{\Delta u_{max}} \end{bmatrix} \tag{A.23}$$

$$A_{\Delta u_{min}} = \begin{bmatrix} F_{\Delta u_{min}} & G_{\Delta u_{min}} & Barrier_{\Delta u_{min}} \end{bmatrix} \tag{A.24}$$

Finally, the matrices are combined to make the inequality constraint matrices b_{in}

and A_{in}.

$$b_{in} = \begin{bmatrix} x_{max} \\ x_{min} \\ u_{max} \\ u_{min} \\ a_{y,max} \\ a_{y,min} \\ \Delta u_{max} \\ \Delta u_{min} \end{bmatrix} \tag{A.25}$$

The size of the full b_{in} matrix is then

$$b_{in} = \begin{bmatrix} x_{max} \\ x_{min} \\ u_{max} \\ u_{min} \\ a_{y,max} \\ a_{y,min} \\ \Delta u_{max} \\ \Delta u_{min} \end{bmatrix} \implies \begin{bmatrix} N \cdot n \\ N \cdot n \\ N \cdot m \\ N \cdot m \\ N \cdot 1 \\ N \cdot 1 \\ N \cdot m \\ N \cdot m \end{bmatrix} = N(2n + 4m + 2) \tag{A.26}$$

With one column. Using this information, the sizes for the A_{in} matrix are locked. The width of the A_{in} matrix is $\mathbf{z}$, and the length of the A_{in} matrix is $N(2n+4m+2)$. It can be constructed in the same way as b_{in} using the A_{in} matrices.

$$A_{in} = \begin{bmatrix} A_{x_{max}} \\ A_{x_{min}} \\ A_{u_{max}} \\ A_{u_{min}} \\ A_{a_{y,max}} \\ A_{a_{y,min}} \\ A_{\Delta u_{max}} \\ A_{\Delta u_{min}} \end{bmatrix} \tag{A.27}$$

B

6x4 Tractor

To investigate the versatility of the controller, a secondary powertrain configuration was investigated, on a 6 wheel tractor. In this case, the cruise axle is on the first rear axle starting from the front, and the startability axle is on the second rear axle.

Adding an axle in the rear will affect the cornering stiffness. Most notably, the bicycle model now has to account for a third cornering stiffness, and the equations for yaw rate and body slip changes accordingly. The subscript $r1$ represents the distance to the first rear axle and $r2$ represents the distance to the very rear axle.

$$\dot{\omega_z} = -\frac{L_f C_{f\alpha} - L_{r1} C_{r1\alpha} - L_{r2} C_{r2\alpha}}{I_{zz}}\beta - \frac{L_f^2 C_{f\alpha} - L_{r1}^2 C_{r1\alpha} - L_{r2}^2 C_{r2\alpha}}{I_{zz} v_x}\omega_z - \frac{L_f C_{f\alpha}}{I_{zz}}\delta_f \tag{B.1}$$

$$\dot{\beta} = -\frac{C_{f\alpha} + C_{r1\alpha} + C_{r2\alpha}}{m \cdot v_x}\beta + \left(\frac{-L_f \cdot C_{f\alpha} + L_{r1} \cdot C_{r1\alpha} + L_{r2} \cdot C_{r2\alpha}}{m \cdot v_x^2} - 1\right)\omega_z + \frac{C_{f\alpha}}{m \cdot v_x}\delta_f \tag{B.2}$$

To simplify, L_{1r} and L_{2r} is reformulated as $L_r + \Delta$ and $L_r - \Delta$, where L_r is the middle point between the two rear axles. The two cornering stiffnesses on the rear axles are assumed to be equivalent, i.e: $C_{r1\alpha} = C_{r2\alpha} = \frac{C_r}{2}$. The method of combining axles provided by C.Wrinkler is then used[41]. Assuming steady state, where $\omega_z = \frac{v_x}{R}$, where R is the radius of the turn and $\dot{\omega_z} = 0$, then a correlation between the understeer coefficient and the steering angle can be found for a vehicle with multiple rear axles:

$$\delta_f - \frac{\hat{L}}{R} = \frac{\Delta^2}{\hat{L}R}\left(1 + \frac{C_{r\alpha}}{C_{f\alpha}}\right) + \left(\frac{C_{r\alpha}L_r - C_{f\alpha}L_f}{\hat{L}C_{f\alpha}C_{r\alpha}}\right)\frac{v_x^2}{R}m \tag{B.3}$$

Where $\hat{L} = L_r + L_f$. Recall the original equation for the understeer coefficient in steady state:

$$\delta_f - \frac{L}{R} = \left(\frac{C_{r\alpha}L_r - C_{f\alpha}L_f}{LC_{f\alpha}C_{r\alpha}}\right)\frac{v_x^2}{R}m = K_u a_y \tag{B.4}$$

It can then be noted that there is an additional term for vehicles with multiple axles:

$$\frac{\Delta^2}{\hat{L}R}\left(1 + \frac{C_{r\alpha}}{C_{f\alpha}}\right) \tag{B.5}$$

This is moved to the other side of the equation and a new equivalent wheelbase is found to represent the multiple axis vehicle as a two-axis vehicle.

$$\delta_f - \frac{1}{R}\underbrace{\left(\hat{L} + \frac{\Delta^2}{\hat{L}}\left(1 + \frac{C_{r\alpha}}{C_{f\alpha}}\right)\right)}_{L_e} = K_u a_y \tag{B.6}$$

Which converts the multi-axis vehicle to a two axis vehicle.

$$\delta_f - \frac{L_e}{R} = K_u a_y \tag{B.7}$$

Where the front is extended by

$$\frac{\Delta^2}{\hat{L}} \cdot \frac{C_{r\alpha}}{C_{f\alpha}} \tag{B.8}$$

and the rear is extended by

$$\frac{\Delta^2}{\hat{L}} \tag{B.9}$$

This is then updated in the state space model every calculation loop.

Additionally, the placement of the brakes and motors are now split. A 6x4 tractor will have brakes in the front, even if the only the rear axles have motors. The input matrices B and the inequality matrices needs to be expanded to account for this. The MPC will, for calculation purposes, keep using a four tyre model with the additions mentioned above. The only notable change needed is that the cruise motor needs to be moved to the rear axle.

The control allocator need to consider the vehicle as a 6 tyre vehicle. Most notably, assuming that all of the rear weight is put on one wheel will result in loss of grip on low friction surfaces, as the CA will prefer to use the cruise axle, likely breaking the friction circle constraint on one of the rear axles assuming that the full rear weight can be utilised. A simplified model of the rear friction circle is used, assuming that the rear weight can be split into two for the rear axles.

$$F_{x_{max},R1} = F_{x_{max},R2} = \frac{F_{x_{max},R}}{2} \tag{B.10}$$

The output from the control allocator is expanded, since there are 6 brake actuators instead of 4. The new input matrix is:

$$B = \begin{bmatrix} \frac{1}{r_w} & \frac{1}{r_w} & \frac{1}{r_w} & \frac{1}{r_w} & \frac{1}{r_w} & \frac{1}{r_w} & \frac{\mathrm{gr_{crs}}}{r_w} & \frac{\mathrm{gr_{crs}}}{r_w} & \frac{\mathrm{gr_{stb}}}{r_w} & \frac{\mathrm{gr_{stb}}}{r_w} \\ -\frac{\mathrm{T_f}}{2\,r_w} & \frac{\mathrm{T_f}}{2\,r_w} & -\frac{\mathrm{T_r}}{2\,r_w} & \frac{\mathrm{T_r}}{2\,r_w} & -\frac{\mathrm{T_r}}{2\,r_w} & \frac{\mathrm{T_r}}{2\,r_w} & -\frac{\mathrm{gr_{crs}\,T_r}}{2\,r_w} & \frac{\mathrm{gr_{crs}\,T_r}}{2\,r_w} & -\frac{\mathrm{gr_{stb}\,T_r}}{2\,r_w} & \frac{\mathrm{gr_{stb}\,T_r}}{2\,r_w} \end{bmatrix} \tag{B.11}$$

The H matrix and g matrix is expanded the same way. The limit matrix is on a tyre level.

$$T_{max} = \begin{bmatrix} F_{x,max,fl} & F_{x,max,fr} & \frac{F_{x,max,rr}}{2} & \frac{F_{x,max,rr}}{2} & \frac{F_{x,max,rr}}{2} & \frac{F_{x,max,rr}}{2} \end{bmatrix} \tag{B.12}$$

Algorithm 3 Distribute max forces on actuators

for i = 1:6 **do**
  if $EM_{lim,low}(i) \leq T_{min}(i)$ **then**
    {The motors can brake more than the friction allows}
    $EM_{lim,low}(i) = T_{min}(i)$;
    $Brake_{lim}(i) = 0$;
  else if $EM_{lim,low}(i) + Brake_{lim}(i) \leq T_{min}(i)$ **then**
    {The motors can't utilize the full F min when braking so the brakes can also be used}
    $Brake_{lim}(i) = T_{min}(i) - EM_{lim,low}(i)$;
  else
    {both brakes and motors don't fully utilize F min}
    $Brake_{lim}(i) = Brake_{lim}(i)$;
  end if
end for

Where $EM_{lim,low} = [0, 0, crs_{min}, crs_{min}, stb_{min}, stb_{min}$ and T_{min} is the friction circle limit on each wheel. A similar algorithm is used to find the maximum allowed force. Results when testing were similar to the 4x4 tractor.

DEPARTMENT OF MECHANICS AND MARITIME SCIENCES
CHALMERS UNIVERSITY OF TECHNOLOGY
Gothenburg, Sweden
www.chalmers.se

CHALMERS
UNIVERSITY OF TECHNOLOGY